Parson, L., Hawkins, J., Allan, J., et al., 1992
Proceedings of the Ocean Drilling Program, Initial Reports, Vol. 135

7. SITE 837[1]

Shipboard Scientific Party[2]

HOLE 837A

Date occupied: 8 January 1991

Date departed: 9 January 1991

Time on hole: 1 day, 2 hr, 20 min

Position: 20°13.307'S, 176°49.360'W

Bottom felt (rig floor; m, drill-pipe measurement): 2763.5

Distance between rig floor and sea level (m): 11.00

Water depth (drill-pipe measurement from sea level, m): 2752.5

Total depth (rig floor; m): 2847.50

Penetration (m): 84.00

Number of cores (including cores with no recovery): 9

Total length of cored section (m): 84.00

Total core recovered (m): 83.90

Core recovery (%): 99.9

Oldest sediment cored:
Depth (mbsf): 94.00
Nature: nannofossil chalk
Earliest age: late Pliocene
Measured velocity (km/s): 1.6

HOLE 837B

Date occupied: 9 January 1991

Date departed: 11 January 1991

Time on hole: 1 day, 2 hr, 25 min

Position: 20°13.319'S, 176°49.362'W

Bottom felt (rig floor; m, drill-pipe measurement): 2764.0

Distance between rig floor and sea level (m): 11.00

Water depth (drill-pipe measurement from sea level, m): 2753.0

Total depth (rig floor; m): 2863.60

Penetration (m): 99.60

Number of cores (including cores with no recovery): 6

Total length of cored section (m): 34.60

Total core recovered (m): 9.07

Core recovery (%): 26.3

Oldest sediment cored:
Depth (mbsf): 70.70
Nature: nannofossil chalk
Earliest age: late Pliocene
Measured velocity (km/s): 1.6

Hard rock:
Depth (mbsf): 70.72
Nature: basalt
Measured velocity (km/s): 3.9

Basement:
Depth sub-bottom (m): 70.72
Nature: basalt
Measured velocity (km/s): 3.90

Principal results: Site 837 is located in the central Lau Basin about 160 km east of the Lau Ridge remnant arc and approximately 69 km west of the axial rift zone of the Eastern Lau Spreading Center (ELSC). The ELSC is the present site of seafloor spreading and generation of new backarc basin crust at the latitude of the drill site. Site 837 is located in a region of north-striking ridges and deeps interpreted as horsts and grabens or half-grabens. The bathymetric relief in the area is about 400 m with ridges shoaling to about 2300 m, rising above basins that can exceed 2700 m depth. In this discussion we will use the term "Basin 837" for the irregular, diamond-shaped, narrow, linear, sedimented trough in which the site is located. Basin 837 is about 10 km long on its major axis, about 2.5 km wide in the north and narrows toward the south-southwest to about 1 km wide at 20°15'S. The seismic character of the sedimentary section is one dominated by planar parallel reflectors, which overlie an irregular hummocky surface comprising a complex series of discontinuous low-frequency reflectors that are interpreted as acoustic basement. The upper seismic unit reaches a maximum thickness of 0.15-s two-way traveltime (TWT) and is here correlated to the seismic Unit A discussed in the site chapter for Site 834 and the other site chapters for Leg 135. As at other sites, the unit continues outside the basin and forms a shallow drape sequence over the emergent basement topography. There is no seismic Unit B at Site 837.

The site was selected to investigate a part of the Lau Basin crust that had been estimated to be intermediate in age between the oldest backarc crust (e.g., Site 834) and young crust formed at the axial rift of the ELSC.

The scientific results are illustrated in Figure 1. The sedimentary sequence recovered at Site 837 is 84 m thick and ranges in age from the latest Pliocene to the middle Pleistocene. The sequence is divided into two lithologic units. Unit I comprises the sediments from the seafloor down to 13.5 mbsf and consists of clayey nannofossil oozes with thin calcareous and volcaniclastic turbidites. Unit II extends from 13.5 to 84.0 mbsf and is divided into five subunits on the basis of grain size, sedimentary structures, and composition. Each subunit defines a sedimentary cycle, starting at the base with thick volcaniclastic turbidites. An upward thinning and fining of individual turbidites occurs as the sediment gradually changes into clayey nannofossil oozes. The thickest turbidite (17.1 m) occurs in Subunit IIC. The volcaniclastics at Site 837 consist of clear, angular, and platy glass shards of rhyodacitic composition, but a minor component of basaltic andesite composition is also present. Below 22 mbsf the sedimentation rate is 39 mm/k.y., which decreases to 38 mm/k.y. for the nannofossil oozes in the upper part of the section.

The sediments from Site 837 range in age from the middle Pleistocene (CN14b, *Globorotalia (Truncorotalia) crassaformis hessi* Subzone of N22) to the upper Pliocene (CN12d, *Globigerinoides quadrilobatus fistulosus* Subzone of N22). The Pleistocene/Pliocene boundary (based on the top of Subzone CN13b) is placed within Core 135-837-7H. Diversity and preservation decrease within the ash and pumiceous beds.

Magnetic polarity reversal results show the base of the Brunhes Normal Polarity Chron (0.73 Ma) at 13.6 mbsf, and the Jaramillo

[1] Parson, L., Hawkins, J., Allan, J., et al., 1992. *Proc. ODP, Init. Repts.*, 135: Ocean Drilling Program (College Station, TX).

[2] Shipboard Scientific Party is as given in the list of participants preceding the contents.

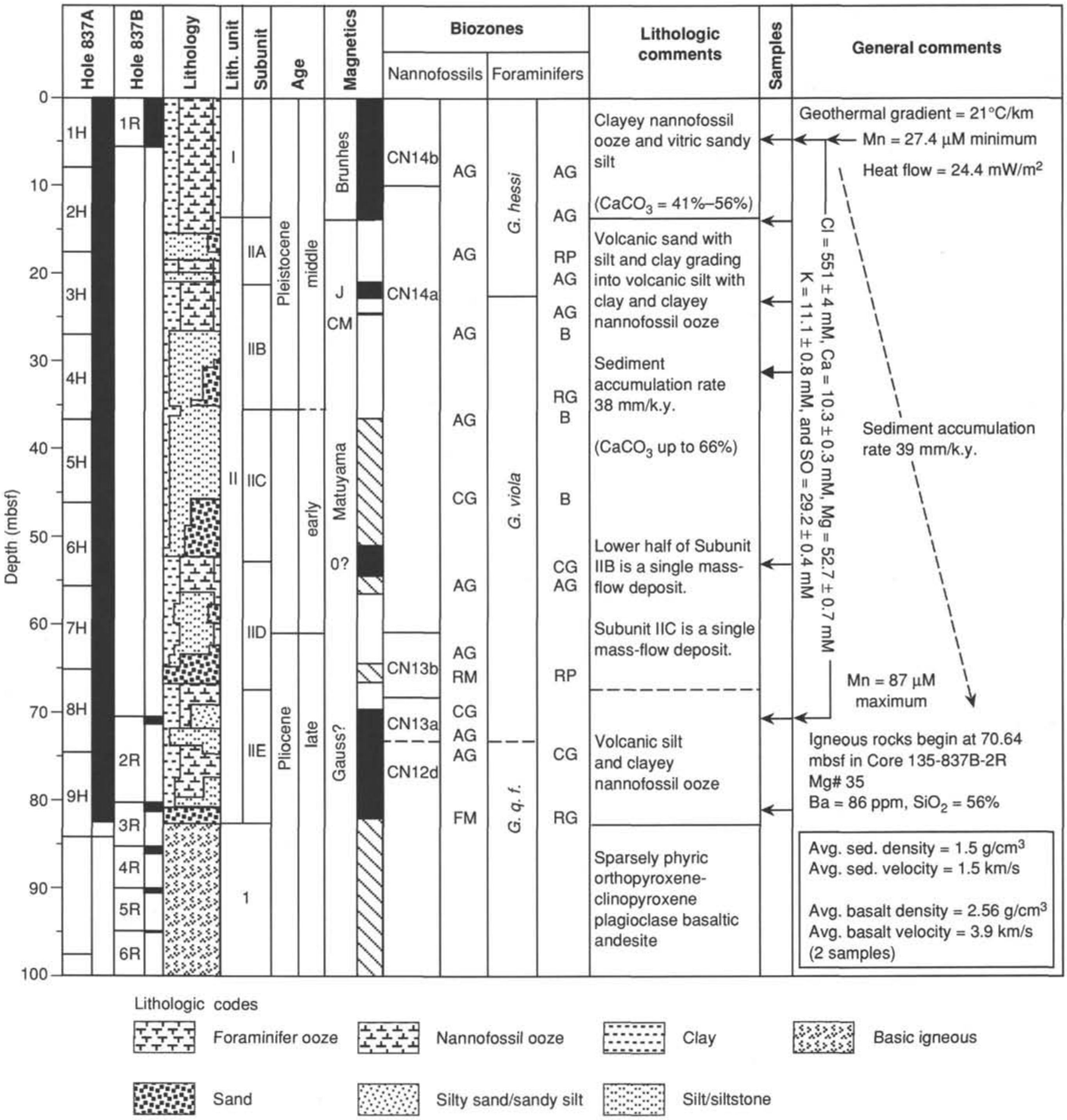

Figure 1. Site summary, Site 837. Abbreviations for abundance are as follows: A = abundant, C = common, F = few, and R = rare, and B = barren. Those for preservation are as follows: G = good, M = moderate, and P = poor. Planktonic foraminifer zones are abbreviated as follows: *G. hessi* = *Globorotalia crassaformis hessi*, *G. viola* = *Globorotalia crassaformis viola*, and *G. q. f.* = *Globigerinoides quadrilobatus fistulosus*.

(0.91–0.98 Ma) and Cobb Mountain (1.11–1.13 Ma) Polarity Subchrons at 21.4–22.7 and 24.3–24.7 mbsf, respectively. For the deeper parts of Hole 837A, two polarity models are suggested. Model A interprets a normal polarity sequence at 69.6–79.0 mbsf as between the top of the Gauss Polarity Chron (2.48 Ma) and the top of the reversed Kaena Polarity Subchron (1.88 Ma), whereas Model B interprets these depths as the Olduvai Subchron (1.66–1.88 Ma). The sedimentation rate calculated from the magnetic polarity reversal data is quite similar to that calculated from the paleontologic data within 5 mm/k.y. Furthermore, the short length of the Brunhes interval recovered in Hole 837A may indicate that up to 55% of this polarity chron is missing. In the sediment section, cyclic variations in the modified Q-ratio (ratio between remanent magnetization intensity and the susceptibility) at periods of 37 k.y. can probably be correlated to Milankovitch cycles.

Results of the shipboard organic geochemical analyses indicated only background levels of methane in the cores at Site 837. These low methane levels indicated that methanogenesis was not occurring in the sediments either because sulfate levels were too high or because there was insufficient organic carbon to maintain microbial activity. Trace levels of organic carbon (0.01%–0.27%) were found. A sample of volcanic sand (13.31 mbsf) was analyzed for total carbon but none was detected. Carbonate values range from 1.9% to 66.1%; the lowest values are from the intervals that contain volcanic sand and silt.

A single igneous lithologic unit was recognized in Hole 837B. It consists of approximately 4 m of very fresh, vesicular, sparsely phyric orthopyroxene-clinopyroxene-plagioclase basaltic andesite underlying upper Pliocene sediments. The rocks possess a seriate porphyritic texture with phenocrysts of plagioclase, clinopyroxene, partially resorbed olivine, and rare orthopyroxene. Some of the plagioclase phenocrysts have resorbed cores and irregular scalloped edges. Many have sodic rims. Some of the euhedral orthopyroxene phenocrysts have rims of clinopyroxene. Two samples, analyzed by shipboard X-ray fluorescence (XRF), are low-K basaltic andesites and have 3.5% MgO, very low Ni and Cr, and low Ti, Zr, and Y. Some of the incompatible trace element characteristics are intermediate between MORB values and rocks from the Tonga and Kermadec volcanic arcs. The Site 837 basaltic andesites are also very similar to Units 1 and 2 from Site 838.

The physical properties data, particularly the GRAPE density and *P*-wave-logger compressional-wave velocity, correlate well with the lithologic units identified in the core. The density of the nannofossil ooze in Unit I is relatively constant at around 1.49 g/cm^3. An increase in the proportion of volcanic sands and silts (30–35 mbsf) and an increase in consolidation of the sediment (7–80 mbsf) are reflected in increased density values. Compressional wave velocity reflects the changes in sediment grain size downhole. The velocity of the nannofossil ooze is about 1490 m/s throughout, and values higher than this reflect increases in grain size as seen in the 30–37 m interval. In the interval between 37 and 53 mbsf, the grain size of the sediments increases from clay to silt with fine vitric ash. Because the density remains constant throughout this interval, the increased velocity is related to the increase in grain size. The heat flow measured at Site 837 is 24.4 mW/m^2, which is low if compared with theoretical heat-flow values of 175 to 200 mW/m^2 predicted for young ocean crust. Although Site 837 is undoubtedly not located within the same heat and fluid circulation cell as Sites 834 and 835, similar conclusions as for those sites can be drawn: (1) the sediments are not thick or diagenetically altered enough to act as an impermeable cap to impede fluid exchange between the sediments and seawater, and (2) the basins are zones of recharge for fluid circulation that serves to dissipate large amounts of heat.

Structural data for the cores at Site 837 are limited, and no logging data are available to support the interpretations made from them. The turbidite flows in the upper part of the section (0–20 mbsf) show a general dip of up to 18° to the north, east, or south. Slightly steeper easterly dips in the lower part of the section (50–80 mbsf) may indicate tilting of the sediments a few degrees to the east during sedimentation. The intermediate stratigraphic levels, in which no bedding planes were measurable, are dominated by a remarkable volcaniclastic turbidite deposit 17 m thick. Although its upper part is fine grained, its thickness indicates very rapid deposition, and close proximity to its source may be inferred. It may be an indication of local tectonic activity. Part of the wide dispersion of the dip data may be a result of depositional as well as tectonic processes. At 16 mbsf, gently dipping hyaloclastite turbidites are cut by a number of planar features lying at a steep angle to the bedding. They are infilled by poorly lithified fossil ooze and definitely cut, but do not offset, banding in the turbidite. Although the volcaniclastic layer is unconsolidated, it appears that it was nevertheless competent enough to fracture before injection of the ooze. The strike of the features is to the north-northeast, parallel to the elongation of the basin, and they may represent fractures caused by extension. Steeply dipping joint planes cut the igneous rocks, but their orientation could not be determined.

BACKGROUND AND OBJECTIVES

Background

Location and Bathymetry

Site 837 is located in the central Lau Basin about 180 km east of the Lau Ridge (remnant arc) and approximately 69 km west of the axial rift zone of the Eastern Lau Spreading Center (ELSC; Fig. 2). The ELSC is the presently active site of generation of new backarc basin crust at the latitude of the drill site.

Bathymetric relief in the area is about 400 m, with ridges shoaling to about 2300 m; they rise above basins that locally exceed 2700 m depth. In this discussion we use the term "Basin 837" for the irregularly shaped, narrow, linear, sedimented trough in which the site is located (Fig. 3). Basin 837 is about 10 km long on its major axis, defined by the 2750-m isobath, and about 2.5 km wide in the north; it narrows south-southwestward to about 1 km at 20°15′S. The deepest part of the basin, as identified with our data, is 2760 m. Basin 837 extends north-northeast and south-southwest between steeply shoaling ridges and discrete highs to the west (rising to <2350 m water depth). The more gently sloping seafloor shoals to at least 2550 m in the east. The steepness of scarps identified on the west flank of the basin, coupled with the subparallel, semicontinuous lineaments traced from the GLORIA sonograph data in the area, delineate a fault-controlled western margin to Basin 837. Subordinate, perhaps antithetic, faulting interrupts the eastern floor and foot of the slope. In the extreme south, around 20°15′S, 176°50′W, the basin floor is significantly shallower, inclined gently to the east, and less planar than the main basin, suggesting some recent faulting and uplift of the floor.

The site was selected to give data for a part of the Lau Basin crust that had been estimated to be intermediate in age between the oldest backarc crust (e.g., Site 834) and young crust formed at the axis of the ELSC. As discussed above (in the "Principal results" section), the magnetic anomaly data in the region of Site 837 are equivocal, and the integration of the ages of the central Lau Basin sites will serve to constrain spreading rates and ages of basin formation.

Geologic Setting

As discussed for Site 836, the regional tectonic and bathymetric fabric trends between north-northeast and north. The basin is one of many bounded by ridges and deeps, interpreted as horsts and grabens or half-grabens, that follow a general northerly trend. Figure 3 illustrates a sketch map of an interpretation of the morphologic and tectonic features near Basin 837. A dredge collection from a ridge adjacent to the drill site on the west (ANT 223, discussed in the "Background and Objectives" section for Site 836) retrieved tholeiitic basalt with geochemical characteristics that indicate a basalt type transitional between N-MORB and arc-like rocks. A nearby heat-flow station, also discussed in the "Background and Objectives" section for Site 836, gave a value of 1.04 μcal/cm^2. Additional data on the geological setting are discussed in the "Background and Objectives" section for Site 836.

Seismic Stratigraphy

The locations of seismic reflection profiles used to select Site 837 are given in Figure 4, and the tracks of the seismic reflection profiles collected by the *JOIDES Resolution* are also illustrated. An example of the data and its interpretation is shown in Figure 5. The seismic character of the sedimentary section is dominated by planar parallel reflectors. These overlie an irregular hummocky surface comprising a complex series of discontinuous low-frequency reflectors that are referred to as acoustic basement. The upper seismic unit at the site reaches a maximum thickness of 0.15 s TWT and is here correlated to seismic Unit A discussed in the "Background and Objectives" section of Site 834. As at the other sites, Unit A continues outside the basin and forms a shallow drape sequence over the surrounding emergent basement topography. A seismic velocity of 1,600 m/s was used to convert traveltime in the sediments to depth; it indicated a depth to

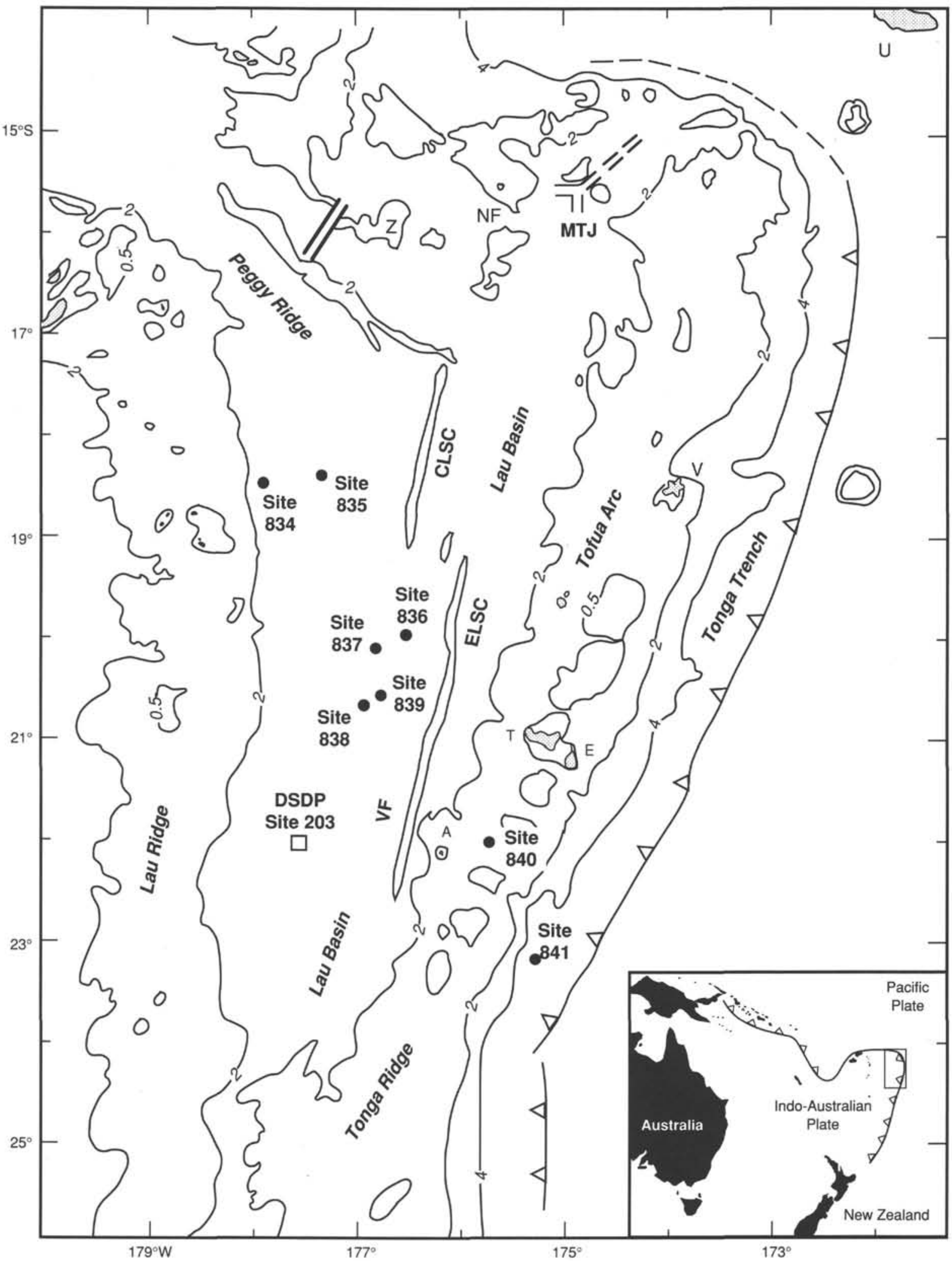

Figure 2. Regional bathymetry of the Lau Basin and the location of Site 837. The figure also illustrates the regional setting for the locations of other drill sites in the Lau Basin and the major geologic features of the Tonga Trench and Lau Basin system. Z = Zephyr Shoal; islands include T = Tongatapu, E = 'Eua, V = Vavau, NF = Niua Fo'ou, and A = Ata. Locations of the Central Lau (CLSC) and Eastern Lau (ELSC) spreading centers, Valu Fa (VF) Ridge, and Mangatolu Triple Junction (MTJ) are from von Stackelberg (1990), Parson et al. (1990), Hawkins et al. (1989), and Nilsson et al. (1989). The location of DSDP Site 203 is shown as an open box. Contour intervals in thousands of meters.

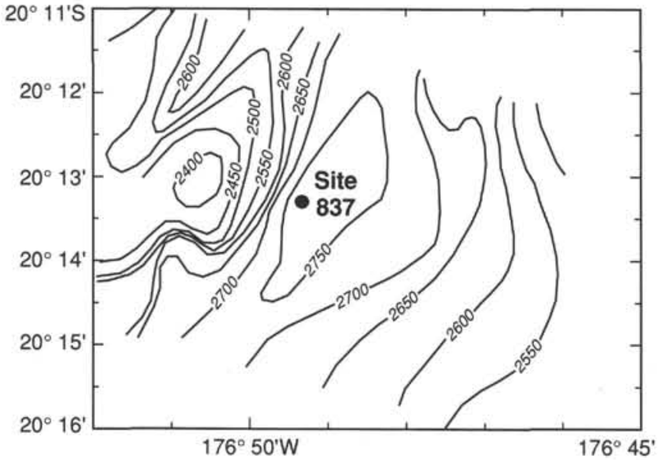

Figure 3. Bathymetry of the area around Site 837, based on conventional wide beam echo-sounder records collected by *Charles Darwin* (Parson et al., 1989) and *JOIDES Resolution*. Contour intervals in meters.

basement of around 120 m. No seismic Unit B is present at Site 837.

Scientific Objectives

The scientific objectives for Site 837 were the same as for Sites 836, 838, and 839, and are discussed in the "Background and Objectives" section for Site 836.

OPERATIONS

Introduction

After completing Site 836, the *JOIDES Resolution* began a 13-nmi transit to the vicinity of Site 837 at 1454 hr UTC on 8 January 1991. The transit took 1.2 hr at an average speed of 10.8 kt. A survey covering 29 nmi, requiring 5.4 hr, was run at 5.4 kt (Fig. 4). The survey was on a set of lines designed to complement the single-channel seismic data acquired earlier (Fig. 4). The drill site is in a narrow (about 1.5 km wide) sedimented basin that is elongated in a north-northeast direction. A summary of the coring operation appears in Table 1.

Site Approach and Site Survey

Site 837 is located in the central Lau Basin on crust of uncertain age. It was considered likely that the crustal age might be similar to that drilled at Site 835 and thus about 4 Ma or the time of magnetic anomaly 3. The crust at this site was expected to be older than that at Site 836 and possibly much older than Site 836 crust if both had formed at the same spreading center. It has been proposed (Parson et al., 1990) that a ridge jump had juxtaposed younger (Site 836) crust against older (Site 837) crust. The drill site would help to test this hypothesis. The area had been surveyed earlier by the *Charles Darwin* on Cruise CD33, which acquired single-channel seismic data and GLORIA imagery of the area (Parson et al., 1989). It was estimated that there would be about 100 m of sediment at the site.

The ship was slowed to 6 kt and two 80-in.^{3} water guns, a 60-element single-channel Teledyne hydrophone, and a magnetometer were deployed. The survey began at 1526 UTC on 8 January 1991 at 20°12.5′S, 176°45.5′W. A Benthos model 210 beacon, broadcasting at 15.0 kHz, was dropped at 2050 UTC on 8 January 1991. The towed gear was retrieved and the ship made a Williamson turn to return to the beacon and come on station.

Drilling and Logging Summary

Our original plan was to drill two adjacent holes at Site 837, with the principal objective being to core the estimated 100-m sediment section and to core 50 m into basement. Hole 837A was to be drilled with the advanced hydraulic piston corer (APC), with the goal of obtaining a relatively undisturbed and complete section. The extended core barrel (XCB) would be used if hard

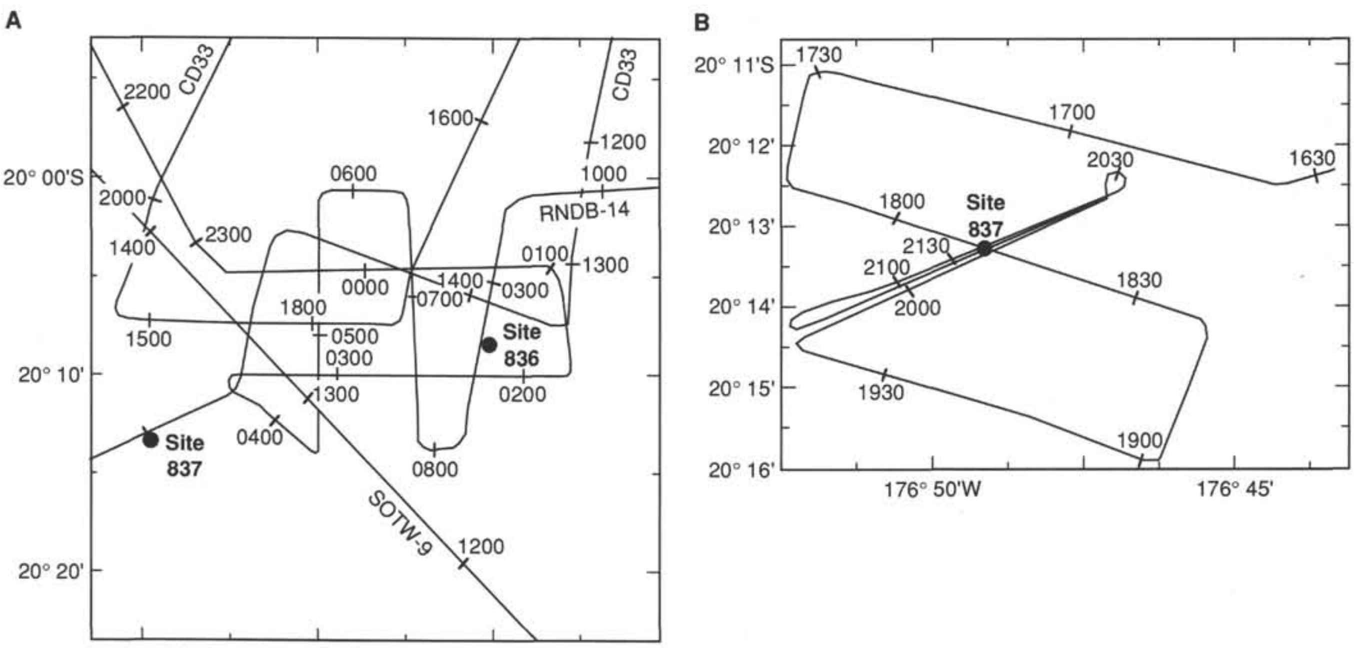

Figure 4. **A.** Track chart of seismic reflection profiles available before Leg 135, collected on *Thomas Washington* (RNDB-14; Hawkins, 1989; SOTW-9, Hawkins, 1976), and the *Charles Darwin* (CD33, Parson et al., 1989). **B.** Track chart of the site approach and survey lines of *JOIDES Resolution* at Site 837.

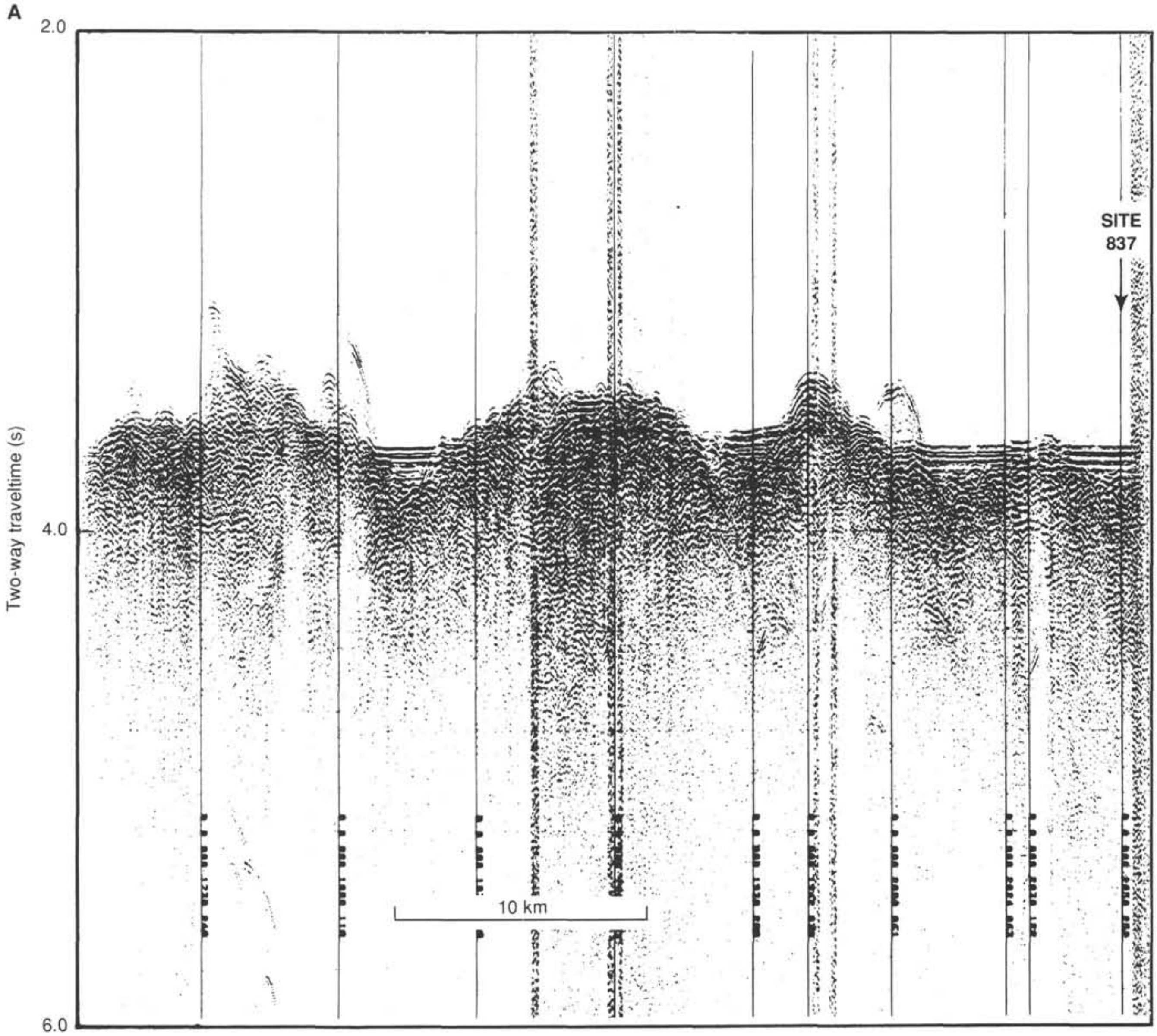

Figure 5. Seismic data for Site 837. **A.** Single-channel seismic reflection profile across Site 837, acquired by the *JOIDES Resolution* during the site survey. **B.** Line interpretation of the profile in Figure 5A. Light stipple areas denote acoustic basement. Upper section is interpreted as Unit A. **C.** Interpretation of seismostratigraphy at Site 837. SB = seismic bottom reflector and TD = total depth.

sediments or basalt sills were encountered, as had been our experience at Site 834. *In situ* temperature measurements were planned, using the WSTP tool at five points 20 m apart, beginning at 30 mbsf. Hole 837B would be cored with the rotary core barrel (RCB) after washing down to the level of APC refusal. Logging would follow conditioning of the hole.

Hole 837A

Hole 837A was sited at 20°13.307′S, 176°49.360′W and spudded in at 0305 UTC on 9 January 1991. Core 135-837A-1H recovered 7.96 m, establishing the mud line at 2763.5 mbrf. The APC was used to take Cores 135-837A-1H to -9H from 0.0 to 84.0 mbsf. The total depth cored was 84.0 m, with 83.57 m recovered (99.49% recovery). A nonmagnetic Monel drill collar was used, and cores were oriented after Core 135-837A-3H using the multishot tool. Temperature measurements were taken at 36.5, 54.5, and 74.5 mbsf with the WSTP tool. APC core refusal was at 84.0 mbsf (Core 135-837A-9H). The core barrel was stuck after a partial stroke. Difficulties in retrieving the core barrel resulted in the decision to pull the drill string and terminate the hole at 1645 UTC on 10 January 1991. The sediments recovered are mainly brown clayey nannofossil ooze interbedded with vitric silt and sand.

Hole 837B

After clearing Hole 837A, the ship moved 20 m south to position 20°13.319′S, 176°49.362′W. Hole 837B was spudded at 0552 UTC on 10 January 1991. Punch Core 135-837B-1R established the seafloor at 2764.0 mbrf, recovering 5.34 m out of a 5.5-m advance. The hole was then washed from 5.5 to 70.5 mbsf. Cores 135-837B-2R to -7R were taken from 70.5 to 104.6 mbsf, with 34.1 m cored and 3.73 m recovered (10.94% recovery).

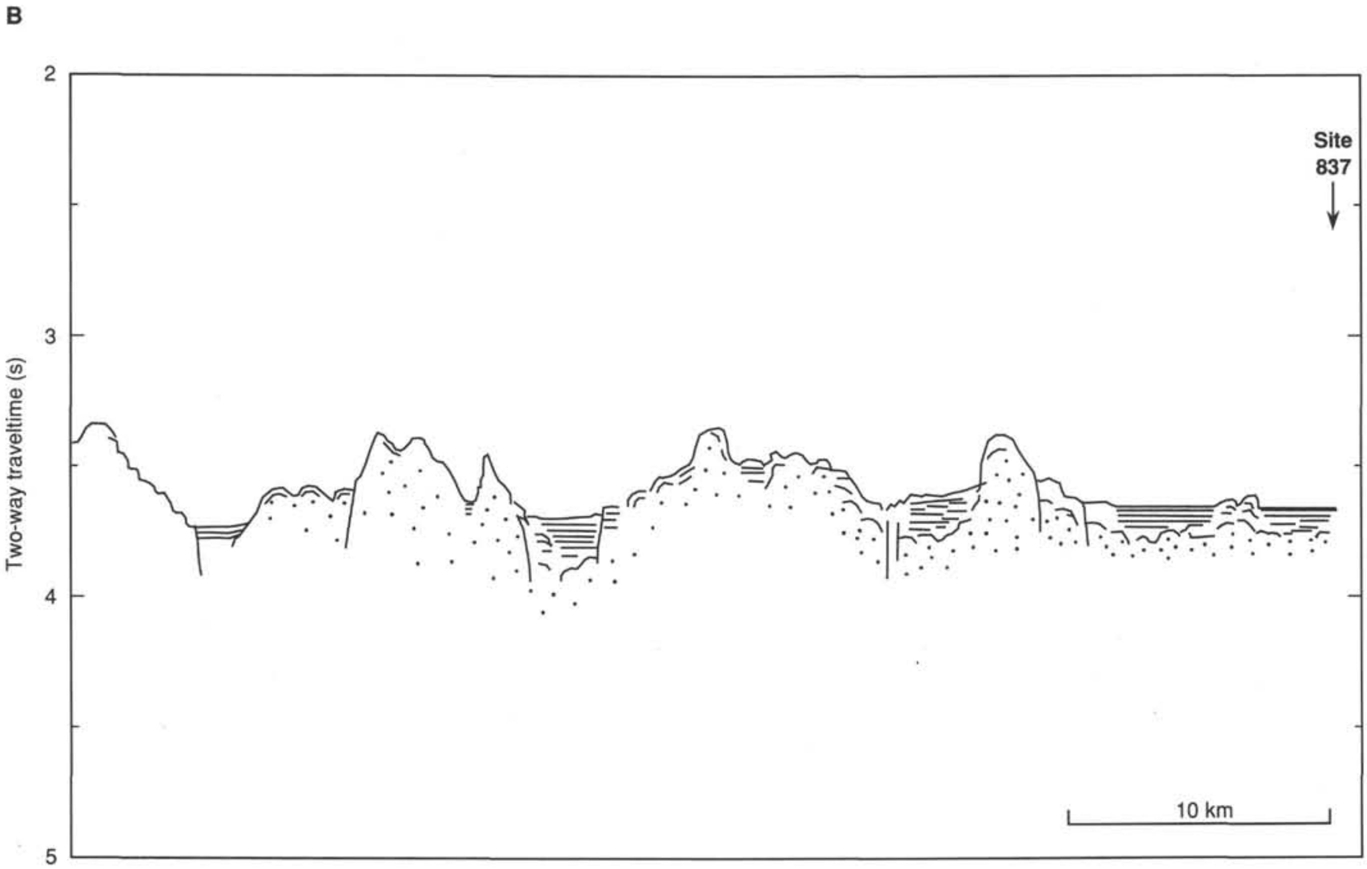

Figure 5 (continued).

Basalt was encountered at 70.64 mbsf. Unstable sloughing basalt and sand was encountered below 84 mbsf, causing the drill string to stick and the electric top drive motor to stall. The drill string was gradually pulled free, with the loss of the mechanical bit release in the bottom-hole assembly (BHA), the drill bit, the flapper valve, and Core 135-837B-8R. By 0155 hr UTC on 11 January 1991, the drill string was retrieved, and the ship was underway to Site 838 shortly thereafter.

LITHOSTRATIGRAPHY

Introduction

The sedimentary sequence cored at Site 837 consists of 82.1 m of clayey nannofossil ooze and vitric volcaniclastics ranging in age from Holocene to late Pliocene (see "Biostratigraphy" section, this chapter). Turbidites, up to 17.1 m thick, make up approximately 60% of the sedimentary sequence. Sediment cores were described and sampled for smear slide descriptions, carbonate analyses, refractive index of glasses, and X-ray diffraction (XRD) studies. The lithostratigraphic summary (Fig. 6) is a synthesis of both holes. The sedimentary sequence at Site 837 was divided into two lithologic units, based on differences in sedimentary textures, structures, and composition and in particular on the abundance of volcaniclastic deposits. Unit I is dominated by clayey nannofossil oozes, whereas Unit II comprises a sequence of thick, graded, volcaniclastic sands and silts that are interpreted as sediment gravity flow deposits. Unit II is further divided into subunits that define individual depositional cycles that fine upward (Fig. 6).

Unit I

Intervals: Sections 135-837A-1H-1 through -2H-4 and 135-837B-1R-1 through -2R-1
Depth: 0–13.54 mbsf

Unit I is 13.54 m thick and composed of brown to dark yellowish brown, iron-oxyhydroxide-stained, clayey nannofossil ooze that contains rare beds of graded foraminifer oozes and thin, vitric silts. The age of Unit I, based on paleomagnetic and biostratigraphic data, ranges from Holocene to middle Pleistocene (0.5–0.6 Ma), with an average sedimentation rate of 25 mm/k.y. (see "Sediment Accumulation Rates" section, this chapter).

Clayey Nannofossil Ooze

The clayey nannofossil ooze is composed mainly of calcareous nannofossils (about 60 vol%), clay (30–40 vol%), and planktonic foraminifers (up to 10 vol%). The proportions of clay- (clay and calcareous nannofossils) and silt-sized (mainly foraminifers) grains remain fairly constant throughout the clayey nannofossil ooze of Unit I (Fig. 7). The ooze is generally fairly homogeneous, although mottled intervals, caused mainly by bioturbation, occur throughout the unit. Pumice and mud clasts, up to 4 cm in diameter, are common and are scattered throughout the ooze. Some of the pumice fragments are heavily altered and rusty brown in color.

The clayey nannofossil ooze contains 41%–56% $CaCO_3$ (Table 2); $CaCO_3$ increases downward through the unit. The ooze is stained brown to dark yellowish brown (Munsell Color values: 10YR 3/4, 4/3, 4/4) and only slight color variations are discernible throughout the unit. The sediment color is slightly darker in the

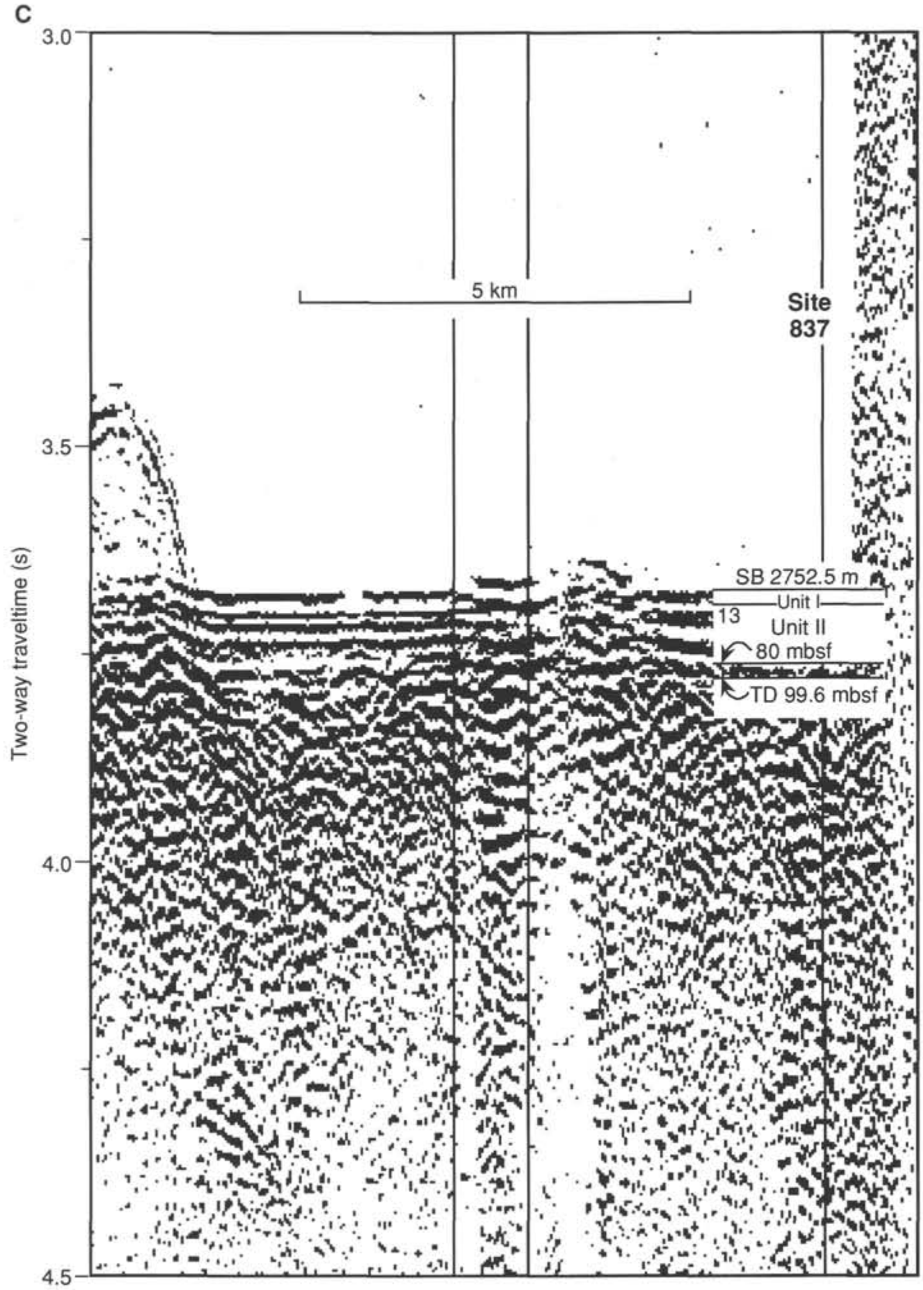

Figure 5 (continued).

upper 1.5 m of the sedimentary section, and the Munsell chart chroma value increases slightly between 5.8 and 8 mbsf. Smear slide analyses show that the color of the clayey nannofossil ooze is a result of the presence of iron oxyhydroxides, occurring as small aggregates within the sediment and as surface coatings around the sedimentary grains. The iron oxyhydroxides are thought to have a hydrothermal origin and are widely distributed throughout the sediments of the Lau Basin (Cronan et al., 1986; Hodkinson et al., 1986; Reich et al., 1990).

Graded Foraminifer Sands and Oozes

Thin, normally graded, clayey foraminiferal ooze interbeds (up to 4 cm thick) containing up to 10% glass occur throughout Unit I. These typically show sharp basal contacts, although the upper parts are often bioturbated and gradational with the overlying clayey nannofossil oozes. Four such interbeds, interpreted as calcareous turbidites, are identified within Unit I (at 1.2, 3.4, 5.7, and 8.3 mbsf).

Volcaniclastic Deposits

Volcaniclastic deposits are generally very rare in Unit I, although a 17-cm-thick, normally graded vitric volcanic silt occurs at 6.8 mbsf (Table 3), comprising about 80% volcanic glass, 10% foraminifers, 5% accessory minerals, and 5% clay. The presence of foraminifers suggests that this is a redeposited layer. A layer interpreted as transitional between clayey foraminifer ooze and

Table 1. Coring summary, Holes 837A and 837B.

Core no.	Date (Jan. 1991)	Time (local)	Depth (mbsf)	Cored (m)	Recovered (m)	Recovery (%)	Age
135-837A-							
1H	9	0325	0.0–8.0	8.0	7.96	99.5	middle Pleistocene
2H	9	0400	8.0–17.5	9.5	9.66	101.0	lower Pleistocene
3H	9	0440	17.5–27.0	9.5	9.84	103.0	lower Pleistocene
4H	9	0530	27.0–36.5	9.5	9.53	100.0	lower Pleistocene
5H	9	0725	36.5–46.0	9.5	9.79	103.0	lower Pleistocene
6H	9	0800	46.0–55.5	9.5	10.00	105.2	lower Pleistocene
7H	9	1000	55.5–65.0	9.5	9.70	102.0	upper Pliocene
8H	9	1045	65.0–74.5	9.5	9.78	103.0	upper Pliocene
9H	9	2330	74.5–84.0	9.5	7.64	80.4	upper Pliocene
Coring totals				84.0	83.90	99.9	
135-837B-							
1R	10	0650	0.0–5.5	5.5	5.34	97.1	middle Pleistocene
2R	10	0945	70.5–80.2	9.7	0.95	9.8	upper Pliocene
3R	10	1120	80.2–85.2	5.0	1.11	22.2	
4R	10	1250	85.2–89.9	4.7	0.81	17.2	
5R	10	1530	89.9–94.9	5.0	0.72	14.4	
6R	10	1755	94.9–99.6	4.7	0.14	3.0	
Coring totals				34.6	9.07	26.2	

vitric silt occurs at 13.5 mbsf. Glass shards are present in some of the calcareous turbidites discussed above (up to 10 vol%). These shards are presumed to have been present in the source area from which the calcareous turbidites were derived.

Unit II

Interval: Sections 135-837A-2H-4 through -9H-CC
Depth: 13.54–82.1 mbsf

Unit II is distinguished from Unit I by the occurrence of very thick beds (up to 17.1 m thick) of upward fining vitric sands and silts. These beds are interpreted as sediment gravity flow deposits on the basis of their grain-size characteristics and sedimentary structures. Some of these deposits appear to have been deposited in rapid succession, as there is often very little pelagic sediment between the clastic beds. Unit II is subdivided into five subunits which each define upward fining depositional cycles. The entire Unit II also shows an overall upward-fining trend; that is, beds toward the base of Unit II (60–82 mbsf) have coarser bases than those in the middle of the sequence (21–52 mbsf), which again have coarser bases than beds in the upper part of Unit II (13.5–21 mbsf, Fig. 7). The volcaniclastic deposits of this unit generally have $CaCO_3$ contents of only 2%–7%; whereas the nannofossil oozes contain up to 66% $CaCO_3$ (Table 2). The age of Unit II ranges from middle Pleistocene to late Pliocene (approximately 0.5–2.0 Ma), with an average sedimentation rate of about 38 mm/k.y. (see "Biostratigraphy" section, this chapter).

Subunit IIA

Intervals: Sections 135-837A-2H-4 through -3H-3
Depth: 13.54–21.0 mbsf

Subunit IIA is 7.46 m thick and consists of normally graded, vitric ashes and vitric silts (3–6 cm thick), interbedded in brown structureless clayey nannofossil ooze (13.54–15.65 mbsf). This overlies an interval (15.65–17.5 mbsf) of normally graded vitric silt and sand beds (each up to 40 cm thick). These overlie each other directly with no interbedded clayey nannofossil oozes. Below this there is a normally graded vitric silt (17.5–18.5 mbsf). The sediment is soft and appears fairly homogeneous, although traces of bedding are suggested by darker gray banding. This interval directly overlies dark brown, homogeneous, clayey nannofossil ooze. A color change from brownish yellow (10YR 6/6) to dark brown (10YR 4/3) in Section 135-837A-3H-1, at 115 cm, 14 cm beneath the base of the overlying volcaniclastic unit, is interpreted as a zone of chemical alteration. The clayey nannofossil ooze is underlain by a normally graded, coarse to medium-grained, vitric silt (19.6–20.0 mbsf), which itself overlies a coarse-grained, normally graded, vitric silt (20–21.0 mbsf). Both units comprise 85–90 vol% volcanic glass shards. The glass is mainly colorless and optically appears fresh. The remainder of the sediments are made up of angular, anhedral to subhedral, feldspar grains (up to 2 vol%), foraminifer tests and test fragments (up to 2 vol%), and calcareous nannofossils and clay-size material (9–11 vol%).

Subunit IIA can be interpreted as a series of volcaniclastic turbidites of variable thickness (4–104 cm thick). Two episodes of turbidite deposition can be recognized, separated by a period of pelagic deposition. The younger turbidites occur between 13.45 and 18.5 mbsf; the older sequence occurs between 19.6 and 21.0 mbsf. The vitric ashes at 13.54–15.26 mbsf (Table 3) are interpreted as primary pyroclastic deposits.

Subunit IIB

Intervals: Section 135-837A-3H-3 through -4H-6
Depth: 21–35.2 mbsf

Subunit IIB is 14.2 m thick and consists of 5.9 m of dark brown clayey nannofossil ooze (21–26.9 mbsf), which overlies 8.3 m of pale brown to gray vitric silt, which grades down into a coarse vitric sand with a sharp base at 35.2 mbsf. The dark brown clayey nannofossil oozes consist of about 30% clay and up to 60% calcareous nannofossils. Foraminifers (about 8 vol%) and volcanic glass (up to 2 vol%) occur in much smaller quantities. Trace amounts of accessory minerals such as opaques and mafics are also present. The clayey nannofossil ooze is stained dark brown (Munsell color codes: 10YR 5/4, 4/3, 5/3) by iron and manganese oxyhydroxides, which occur as small aggregates or grain coatings within the sediments. The sediment, which is firm and slightly mottled throughout, contains rare weathered pumice lapilli and mud clasts up to 1 cm in diameter. Mud clasts are particularly common in the upper part of the unit between 21.0 and 22.0 mbsf.

At 26.9 mbsf a 28-cm thick, brownish yellow, homogeneous vitric silt with clay overlies 7.96 m of dark yellowish brown, firm vitric silt that grades down into a coarse vitric sand. Apart from a

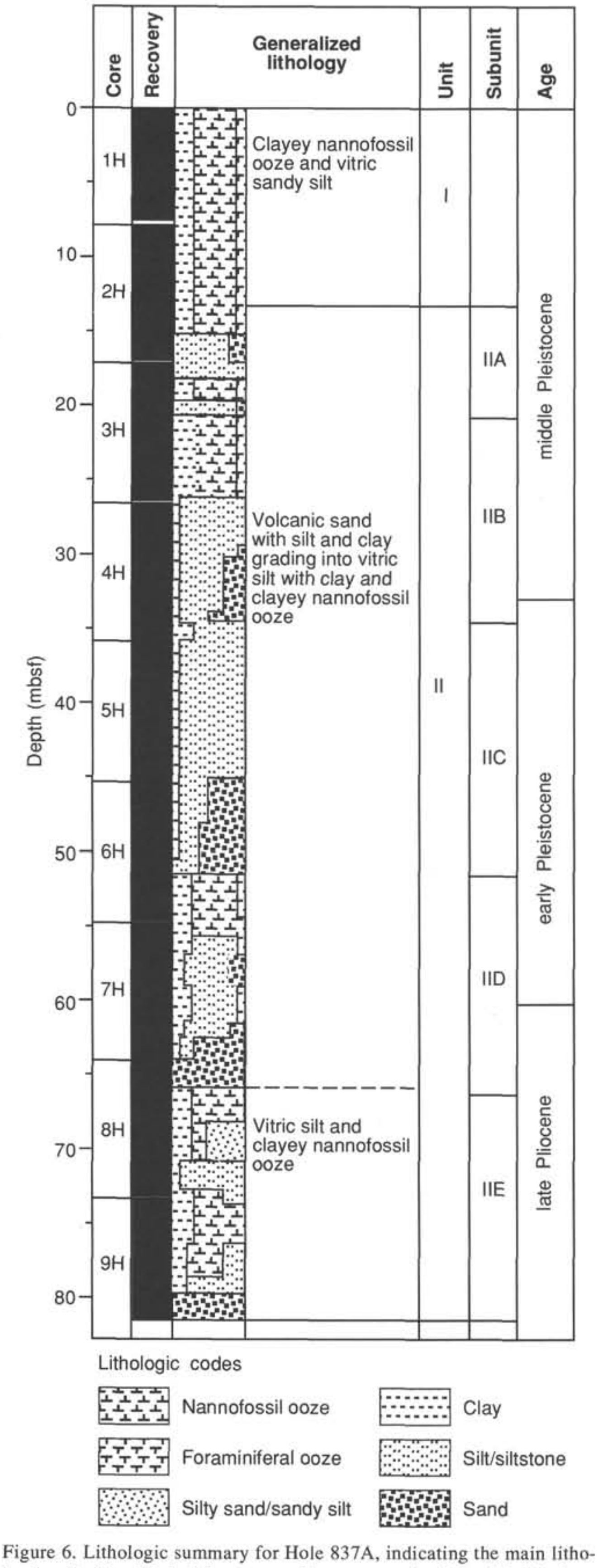

Figure 6. Lithologic summary for Hole 837A, indicating the main lithologic units identified with age as well as a generalized graphic lithology for Site 837.

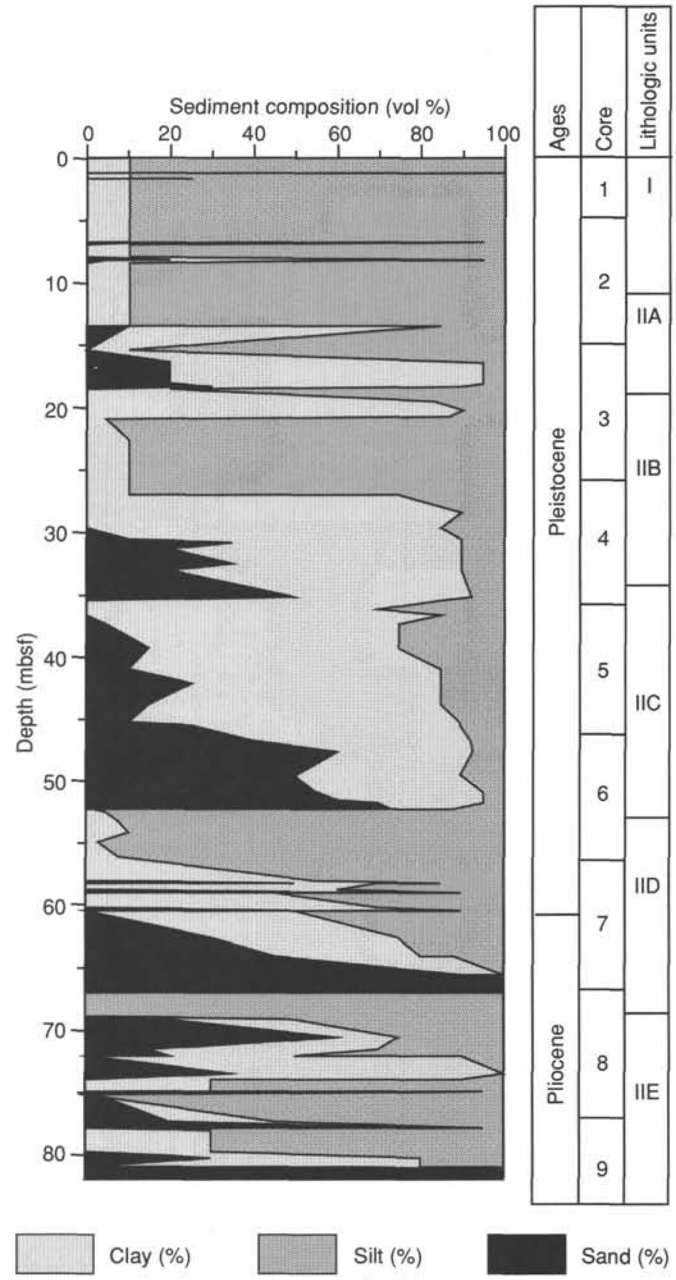

Figure 7. Grain-size variations with depth within the sedimentary sequence in Hole 837A. Note that the subdivision of Unit II corresponds with fining-upward cycles.

clear upward-fining sequence, no internal structures are present in this homogeneous sediment. The vitric silt comprises about 90% of colorless and optically clear volcanic glass, minor amounts of foraminifers (1 vol%), calcareous nannofossils (3 vol%), clay (6 vol%), and trace amounts of feldspar and accessory minerals. These proportions remain remarkably constant throughout the unit, except immediately above the base where the amount of feldspar and accessory minerals increases to 3–4 vol%. Grain-size profiles throughout this unit clearly show an upward-fining trend (Fig. 7).

The lower, volcaniclastic part of this subunit is interpreted as a sediment gravity flow deposit on the basis of its grain-size structure. The homogeneity of the deposit suggests that it may

Table 2. $CaCO_3$ content of sediments in Hole 837A.

Core, section, interval (cm)	Depth (mbsf)	$CaCO_3$ (%)	Unit	Description
135-837A-				
1H-2, 80	2.30	45.50	I	Clayey nannofossil ooze
1H-4, 78	5.28	41.40	I	Clayey nannofossil ooze
1H-6, 7	7.57	54.60	I	Clayey nannofossil ooze
1H-CC, 9	7.86	50.80	I	Clayey nannofossil ooze
2H-2, 74	10.20	56.20	I	Clayey nannofossil ooze
2H-4, 81	13.30	52.80	I	Clayey nannofossil ooze
2H-6, 99	16.50	4.70	IIA	Vitric sandy silt
3H-6, 69	25.70	66.10	IIB	Clayey nannofossil ooze
4H-2, 65	29.20	4.30	IIB	Vitric silt
4H-4, 68	32.20	1.90	IIB	Vitric silt
7H-2, 71	57.70	64.10	IID	Clayey nannofossil ooze
7H-3, 70	59.20	29.50	IID	Clayey vitric silt with nannofossils
7H-4, 71	60.70	21.60	IID	Clayey vitric silt with nannofossils
7H-6, 101	64.00	7.40	IID	Clayey silty vitric sand
8H-2, 25	66.80	4.50	IID	Vitric sand
8H-2, 86	67.40	52.10	IIE	Clayey nannofossil ooze
8H-4, 66	70.20	41.00	IIE	Clayey vitric mixed sediment
8H-6, 81	73.30	5.80	IIE	Vitric silt
9H-1, 27	74.80	5.80	IIE	Vitric sandy silt
9H-1, 76	75.30	60.10	IIE	Clayey nannofossil ooze
9H-1, 130	75.80	57.10	IIE	Clayey nannofossil ooze
9H-2, 76	76.80	59.00	IIE	Clayey nannofossil ooze
9H-4, 63	79.60	45.20	IIE	Clayey vitric nannofossil ooze

represent a single depositional event. Water escape may have destroyed the original sedimentary structures. After deposition of this sequence, there was a relatively long period of continuous pelagic sedimentation, represented by the overlying clayey nannofossil ooze.

Subunit IIC

Intervals: Sections 135-837A-4H-6 through -6H-5
Depth: 35.20–52.30 mbsf

Subunit IIC comprises a single upward-fining sequence 17.10 m thick (Figs. 7 and 8). From the base upward, the lithology grades from (1) vitric sand with silt and clay to (2) silty vitric sand with clay and then to (3) clayey vitric silt in the uppermost part. The color changes upward from gray (5Y 3/1) with layers of black (5Y 2.5/1) and very dark gray (5Y 3/1) in (1) to light greenish gray (10Y 6/1) in (2) to light greenish gray (10Y 6/2) in (3).

The sequence in Subunit IIC rests on an eroded basal surface overlain by 1–2 cm of granule-sized (2–5 mm in diameter) grains. The sequence is remarkably homogeneous throughout except within the lowermost 80 cm, where well-developed planar lamination/bedding is present. The laminae/beds within this interval vary in thickness from 0.5–3 cm, are enriched in heavy and accessory minerals, and internally often show normal and reverse grading. In the lower part of the stratified interval, the maximum grain size is approximately 5 mm, and the lithology is thus a very coarse-grained granular sandstone. A layer of very coarse-grained granular sandstone also occurs in Section 135-837A-6H-4, 100–102 cm, 76 cm above the base of the subunit.

Above the stratified interval, the sequence is structurally very homogeneous. Except for upward-fining shown by increasing content of clay-sized material and a decrease in the volume of sand, no structures were observed except for a faint lamination in the uppermost part of the sequence, in Section 135-837A-4H-6, 70–100 cm. This interval is also slightly mottled.

The sediments of this unit appear to be moderately to well sorted. Clasts much larger than the mean maximum (average of 10 largest clasts) were not observed, but granule-sized grains up to 5 mm in diameter occur at the base. Clast composition is fairly constant throughout. Vitric material constitutes 85%–90% by volume of deposit, whereas clay and nannofossils make up approximately 5 vol% each.

The thick, graded sand-silt making up Subunit IIC was deposited during a single mass-flow event. The lack of sedimentary structures, the relatively good sorting, and the general upward fining throughout the unit suggest that this bed may have been deposited from a high-density turbulent flow (Lowe, 1982). A sediment gravity flow deposit as thick as the one comprising Subunit IIC is unlikely to have a distal source.

Subunit IID

Intervals: Sections 135-837A-6H-5 through -8H-2
Depth: 52.30–67.00 mbsf

Subunit IID is 14.70 m thick and, from the base upward, is composed of light gray (10YR 7/1) vitric sand, pale olive (5Y 6/3) to yellowish brown (10YR 5/4) vitric sand with silt and clay, brown (10YR 5/3) clayey vitric silt with nannofossils, yellowish brown (10YR 5/4) vitric silt with clay and sand, dark yellowish brown (10YR 4/4) clayey nannofossil ooze, and brown (10YR 4/3) clayey nannofossil ooze with foraminifers.

The base of Subunit IID in Section 135-837A-8H-2, 55 cm, is an erosional surface (Fig. 9). Overlying this boundary is a sequence of poorly sorted, granular, very coarse-grained sands and gravels extending to the top of Core 135-837A-8H. The maximum grain size of the granules is approximately 12 mm (Fig. 9), and the mean maximum (average of ten largest clasts) is around 5 mm. Most pumice clasts are well rounded. The lowermost 50 cm of the sequence are clearly reversely graded, and the lowermost 25 cm are also planar stratified, with dark, mafic, mineral-rich layers at the base grading up into lighter colored layers of foraminifer-bearing sand. The remaining part of the sequence, to the top of Section 135-837A-8H-1, consists of thin- to medium-bedded and occasionally stratified, very coarse-grained sandstones and gravels. The beds are usually ungraded or normally graded, but some exhibit inverse grading. This sediment consists almost exclusively of volcanic glass, which makes up 85%–90% by volume, with nannofossils and clay together comprising approximately 10%.

An interval of thin-bedded vitric silty sand (Sections 135-837A-7H-CC, 5 cm, to -7H-6, 117 cm) with interbedded thickly laminated vitric silty sand (Section 135-837A-7H-7, 27–59 cm) overlies this deposit. Both the thin beds and the laminae show normal grading. This interval is overlain by an upward-fining sequence grading from clayey and silty vitric sand into clayey and sandy vitric silt, which in turn grades into clayey vitric silt with nannofossils (Sections 135-837A-7H-6, 117 cm, to -7H-4, 52 cm. The sequence commonly shows normally graded layers and planar lamination.

From Sections 135-837A-7H-4, 52 cm, through -7H-1, 150 cm, there are six other upward-fining sequences, grading from vitric sand or vitric silt up into clayey vitric silt or vitric silt with nannofossils. These sequences are 7–142 cm thick, and often show planar lamination in their lower parts. The basal surfaces are usually eroded.

The remaining part of Subunit IID, 57.0–52.3 mbsf, consists of clayey nannofossil ooze and clayey nannofossil ooze with foraminifers. Rusty-colored pumice fragments up to 2 cm in diameter are common in the lower part of the sequence. The upper part of the sequence, from 55.5 to 52.3 mbsf, has been strongly affected by soft sediment deformation. In the upper part of the oozes there occurs a color change (interpreted as a chemical

Table 3. Discrete ash layers and volcaniclastic turbidites in Hole 837A.

Core, section, depth to smear-slide sample	Depth (mbsf)	Smear slide	Interval thickness (cm)	Type	Glass (vol%)	Maximum grain size (mm)	Shard morphologies			Igneous minerals present (>1%)
							Tubular	Bubble wall	Angular	
1H-1, 125	1.22–1.26		4	E,G	10	ND				
1H-5, 84	6.69–6.86	1	17	E,G	80	600	X	X	X	plag, augite
2H-1, 16	8.00–8.18	1	18	E,G	85	300	X	X	X	plag
2H-1, 31	8.18–8.31	1	13	E,G	50	450	X		X	plag, augite, olivine
2H-4, 103	13.47–13.54	1	7	P,G	75	400	X	X		plag, augite
2H-5	14.88–14.91		3	P,G	ND	Silt				
2H-5	15.20–15.26		6	P,G	ND	Silt				
2H-6	15.26–15.54		28	E,G	ND	Silt				
2H-6	15.54–15.74		20	E,G	ND	Sand				
2H-6	15.74–15.81		7	E,G	ND	Sand				
2H-6	15.81–15.88		7	E,G	ND	Sand				
2H-6	15.88–16.01		13	E,G	ND	Sand				
2H-6	16.01–16.18		17	E,G	ND	Sand				
2H-6	16.18–16.22		4	E,G	ND	Sand				
2H-6	16.22–16.32		10	E,G	ND	Sand				
2H-6	16.32–16.37		5	E,G	ND	Sand				
2H-6, 102	16.37–16.58	1	21	E,G	95	180	X	X	X	
2H-6	16.58–16.72		14	E,G	ND	Sand				
2H-6	16.72–16.87		15	E,G	ND	Sand				
2H-6 to 2H-7	16.87–17.33		46	E,G	ND	Sand				
2H-7	17.33–17.44		11	E,G	ND	Sand				
2H-7	17.44–17.47		3	E,G	ND	Sand				
2H-7	17.47–17.50		11	E,G	ND	Sand				
3H-1, 50 and 95	17.50–18.52	2	102	E,G	89	300/500	X	X	X	plag
3H-2, 60	19.00–20.01	1	101	E,G	80	200			X	plag
3H-2	20.01–20.11		10	E,G	ND	Silt				
3H-2, 118	20.11–20.25		14	E,G	90	Silt				
3H-2	20.25–20.42		17	E,G	ND	Silt				
3H-3	20.42–20.55		13	E,G	ND	Silt				
3H-3	20.55–20.58		3	E,G	ND	Silt				
3H-3	20.58–20.61		3	E,G	ND	Silt				
3H-3	20.61–20.65		4	E,G	ND	Silt				
3H-3	20.65–20.69		4	E,G	ND	Silt				
3H-3, 22	20.69–20.76	1	7	E,G	85	Silt				
3H-3	20.76–20.81		5	E,G	ND	Silt				
3H-3	20.81–21.05		24	E,G	ND	Silt				
3H-CC, 10	27.05–27.32	1	27	E,H	85	100		X	X	
4H-1 to 4H-6	27.10–35.20	9	810	E,G	85/90	800	X	X	X	plag, augite
4H-5 to 6H-6	35.20–52.28	16	1708	E,G	85/90	800	X	X	X	plag, augite, hypersthene, olivine
7H-2, 120 and 141	56.50–57.92	2	50	E,H	55/85	ND	X	X	X	plag, augite
7H-3, 25 and 56	58.42–59.08	2	66	E,G	82/60	170/650	X	X	X	plag, hypersthene
7H-3, 59	59.08–59.34	1	26	E,G	45	Sand				
7H-3	59.34–59.61		27	E,G	ND	Silt				
7H-3	59.61–59.70		9	E,G	ND	Silt				
7H-4, 21 and 47	59.70–60.52	2	82	E,H	73/88	250/500	X	X	X	plag
7H-4, 62	60.52–62.40	1	188	E,G	60	140	X		X	
7H-5	62.40–62.48		8	E,G	ND	ND				
7H-6 to 7H-5	62.48–64.17	3	169	E,H	80/65	200/420	X	X	X	plag
7H-6, 79	64.17–65.00	1	83	E,H	79	300				
8H-1, 55	65.00–67.05	1	205	E,G	60	1100	X	X	X	plag, augite
8H-3	69.23–69.36		13	E,G	ND	Silt				
8H-3	69.36–69.39		3	E,G	ND	Silt				
8H-3	69.39–69.43		4	E,G	ND	Silt				
8H-3	69.43–69.47		4	E,G	ND	Silt				
8H-3 to 8H-4	69.47–69.61		14	E,G	ND	Silt				
8H-4	69.61–69.85		24	E,G	ND	ND				
8H-4, 110	69.85–70.66	1	81	E,G	20	ND				
8H-5, 60	70.66–72.40	1	174	E,H	70	120			X	
8H-6, 100	72.40–74.31		191	E,G	95	Silt				
9H-1, 50	74.31–75.07	1	76	E,G	85	300	X	X	X	plag
9H-2	77.30–77.35		5	E,H	ND	ND				
9H-3, 34	77.76–77.87		11	E,G	90	700	X	X	X	augite
9H-3	77.87–77.97		10	E,G	ND	Sand				
9H-3	77.97–78.07		10	E,G	ND	Sand				
9H-3	78.07–78.12		5	E,G	ND	Sand				
9H-3	78.37–78.49		12	E,G	ND	Sand				
9H-4	79.21–79.23		2	E,G	ND	Sand				
9H-4	79.23–79.26		3	E,G	ND	Sand				
9H-4	79.26–79.31		5	E,G	ND	Sand				
9H-4	79.31–79.38		7	E,G	ND	Sand				
9H-4 to 9H-CC	80.10–84.00	2	390	E,H	80/95	300–250	X	X	X	plag, augite

Notes: Note that glass content will normally indicate maximum modal abundance as estimated from smear slides. Glass content may be highly variable in individual units, especially in the graded sequences. P = pyroclastic, E = epiclastic, H = homogeneous, G = graded, and ND = not determined. Plag = plagioclase.

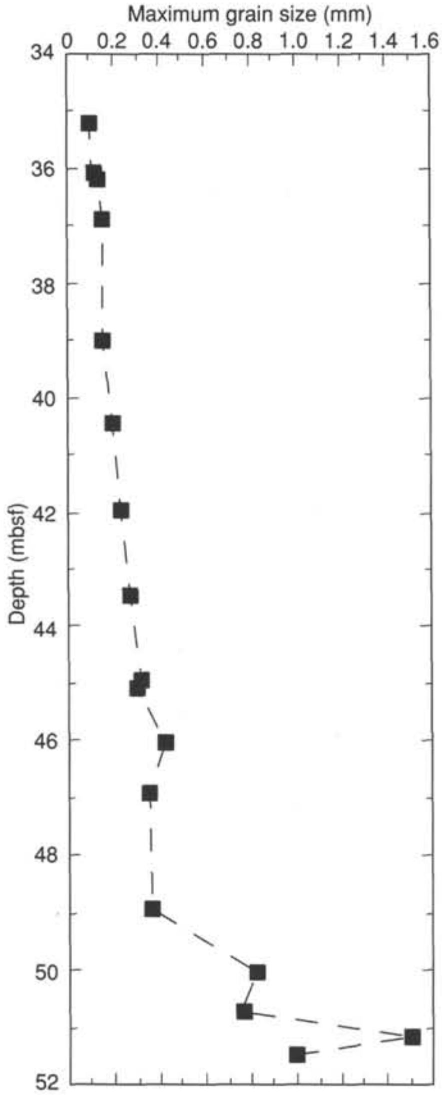

Figure 8. Variation in maximum grain size (measured from smear slides) with depth within Subunit IIC. Filled squares represent individual sampling points.

alteration front) from white (5Y 8/2), immediately beneath the overlying subunit, to olive (5Y 5/4), to yellowish brown (2.5Y 6/4), to brown (10YR 4/3).

The sediments in the lower part of Subunit IID (up to Section 135-837A-7H-1, 150 cm; depth, 57 mbsf) are interpreted as a series of mass-flow deposits, predominantly high-density turbidites (Lowe, 1982), with some showing facies transitional to debris flows. Many of the sequences are relatively well sorted and show an upward-fining trend indicative of settling from a turbulent suspension. Planar lamination indicates alternate deposition of bedload and suspended load (Walker, 1975), although the influence of grain collisions and dispersive pressure is reflected in reverse grading immediately above the bases of some flows (Bagnold, 1956). Such sequences, starting at the base with a reversely graded layer and overlain by an ungraded or stratified layer, have been termed traction carpets (Hiscott and Middleton, 1979; see also Pickering et al., 1989). The occurrence of well-rounded, lapilli-sized pumice pebbles may show that these were reworked before redeposition, although pumice clasts also may become rounded during eruptions. The clayey nannofossil ooze in the upper part of Subunit IID was deposited during a interval of pelagic sedimentation. Soft sediment deformation in the upper part of this interval most likely occurred subsequent to deposition of the extraordinarily thick turbidite in Subunit IIC (see above).

Subunit IIE

Intervals: Sections 135-837A-8H-2 through -9H-CC
Depth: 67.0–82.1 mbsf

Subunit IIE is 15.1 m thick and is composed of a series of thin- to very thick-bedded, fining-upward sequences. Vitric sands mainly occur in Core 135-837A-9H and are black (2.2Y 2/0) in color. Vitric silts are generally dark gray (5Y 4/1), greenish gray (5Y 5/3), and light olive gray (5Y 6/2), whereas clayey nannofossil oozes are brown to dark brown (10YR 3/3 and 10YR 4/3). There is often a color change in the clayey nannofossil oozes, a short distance beneath volcaniclastic beds. These are interpreted as chemical alteration fronts (see also Subunit IID). Both yellowish brown (10YR 5/4), light yellowish brown (10YR 6/4), and very pale brown (10YR 7/4) colors are common.

Subunit IIE starts at the base with a vitric sand and grades upward through a vitric silt into clayey nannofossil ooze (82.1–79.4 mbsf). The interval is very homogeneous throughout. Above this, from 79.4 to approximately 77.3 mbsf, there is a sequence of normally graded and upward-fining beds that vary in thickness from 2 to 70 cm. These units all have planar eroded bases. In their lower parts the beds are composed of structureless black sands that pass upward into mottled, clayey nannofossil oozes. Clayey nannofossil ooze between 77.3 and 75.1 mbsf is occasionally mottled and contains scattered pumice clasts up to 2 cm in diameter.

The nannofossil ooze is overlain by a 76-cm-thick sequence of vitric sand and silt that fines upward and passes into clayey nannofossil oozes. In its lower part, this sequence is graded and shows planar lamination. Between 74.3 and 72.4 mbsf, a homogeneous vitric volcanic silt is overlain by a sequence of vitric silts and sands that grades upward into mottled clayey nannofossil oozes (72.4–69.2 mbsf). These sequences usually have eroded bases, are graded, and may show planar lamination in their lower parts. They vary in thickness from 2 to 80 cm, with the thinner beds occurring in the upper part of the interval (Fig. 10). Ripple cross-lamination occurs directly above the base of one of these beds, in Section 135-837A-8H-4, 112–116 cm. This was only observed after cutting the core with a knife for strike and dip measurements, and it is possible that cross-lamination also occurs in the lower part of other intervals but was not resolved on cut core faces. A sequence of clayey nannofossil ooze, which is occasionally mottled and contains scattered pumice fragments, is present from 69.2 mbsf to the top of the subunit.

We interpret the sediments of Subunit IIE as a series of volcaniclastic turbidites interbedded in clayey nannofossil oozes. The oozes represent periods of more stable hemipelagic deposition. Two longer periods of hemipelagic deposition occur. These are represented by the sequences of nannofossil ooze at 77.3–75.1 and 69.2–67 mbsf.

Chemical Composition of Glasses

Volcaniclastic sediments are much more abundant at Site 837 than at Sites 834, 835, and 836. In Hole 837B no volcaniclastic material was recovered. Seventy-three individual layers rich in volcaniclastic material were identified in cores from Hole 837A and examined in 54 smear slides (Table 3). Refractive indexes were determined in eight representative samples to estimate the SiO_2 concentrations of optically clear vitric shards. The methods used are described in detail in the site chapters for Sites 834 and 835 (see "Lithostratigraphy" section, Sites 834 and 835 chapters).

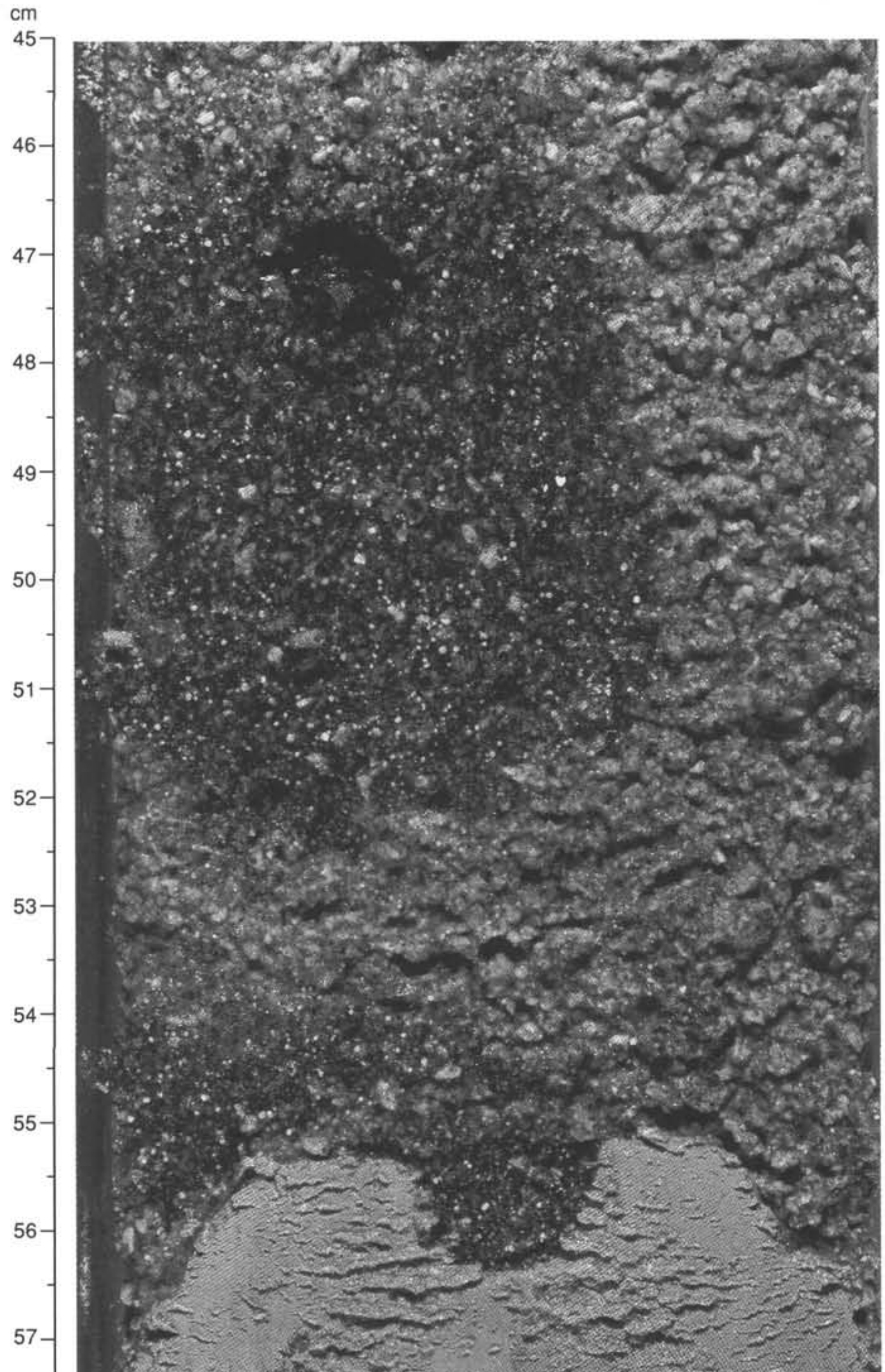

Figure 9. Lowermost part of Subunit IID, illustrating the eroded base and reverse grading. Note the mafic clast (12 mm in diameter) and surrounding staining (Section 135-837A-8H-2, 45–58 cm).

Volcaniclastic deposits in Hole 837A are generally dominated by clear, angular, and platy volcanic glass shards. The proportion of pumiceous clasts with tubular vesicles and fibrous varieties increases with average grain size. Pale brown to pale green glass and igneous-derived minerals such as plagioclase, augite, olivine, and hypersthene normally occur only in trace amounts but occasionally make up substantial amounts in the basal parts of thicker turbidites.

The volcaniclastics in Hole 837A are dominated by clear, colorless shards of dacitic to rhyodacitic composition showing surprisingly small compositional variations. Most samples have 70 to 71 wt% SiO_2 (Fig. 11 and Table 4). However, XRF analysis

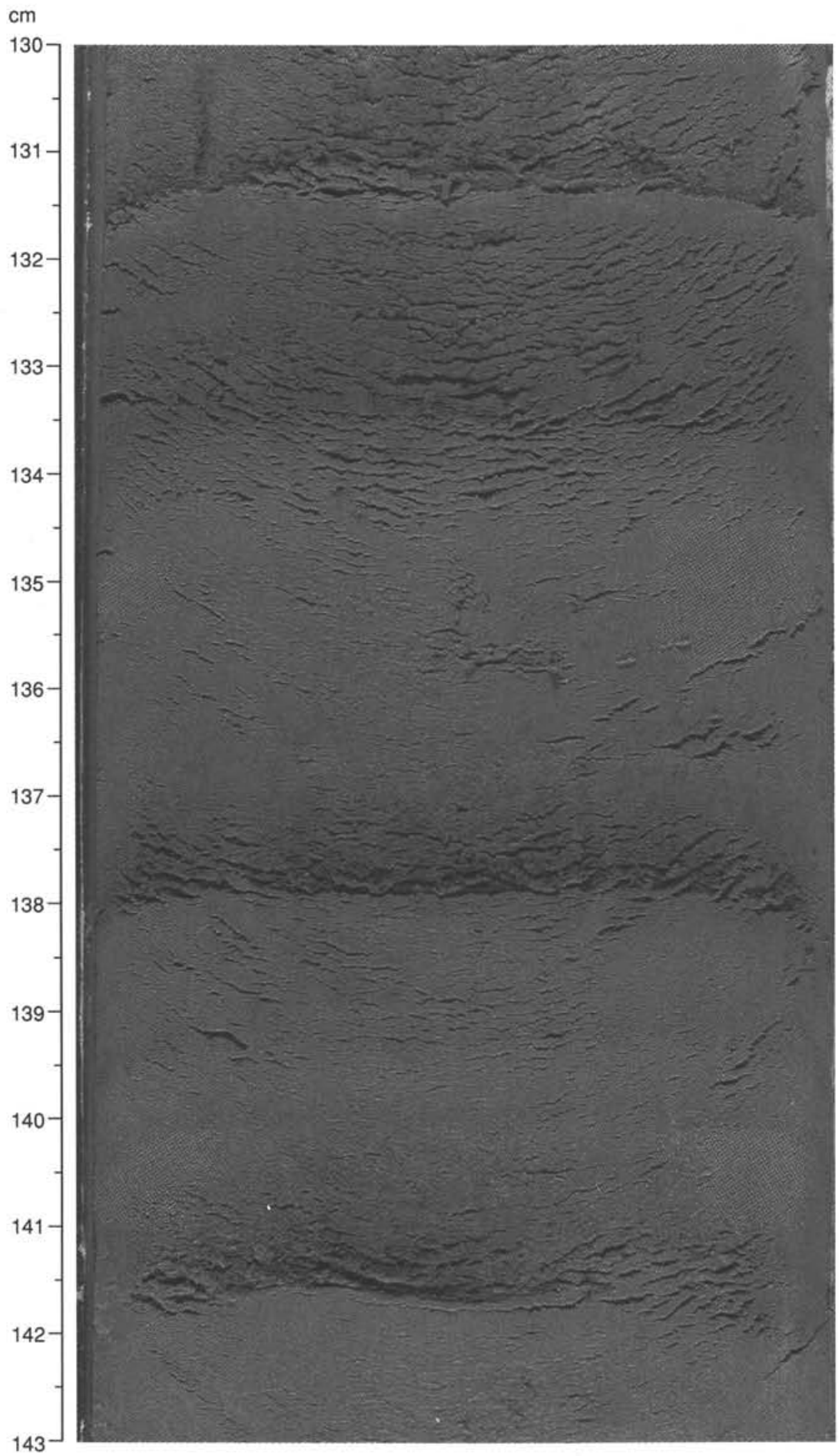

Figure 10. Sequence of thin-bedded turbidites stacked directly on top of one another, without interbedded hemipelagic deposits; note the planar, noneroded bases (Subunit IIE, Section 135-837A-8H-3, 130–143 cm).

of a pumice clast from Subunit IID (Section 135-837A-8H-1, 108–116 cm, at 66.1 mbsf) shows 77.15 wt% SiO_2. A second population of pale brown shards is normally present only in trace amounts, but it becomes the dominant shard type in a few beds, most of them <10 cm thick, in Unit I. The pale brown glasses are basaltic andesites. These also show little compositional variation (54–55 wt% SiO_2).

The alteration of glasses in Hole 837A is low, in agreement with the homogeneity of the refractive index data. However, low first-order birefringence, indicative of the hydration of glass

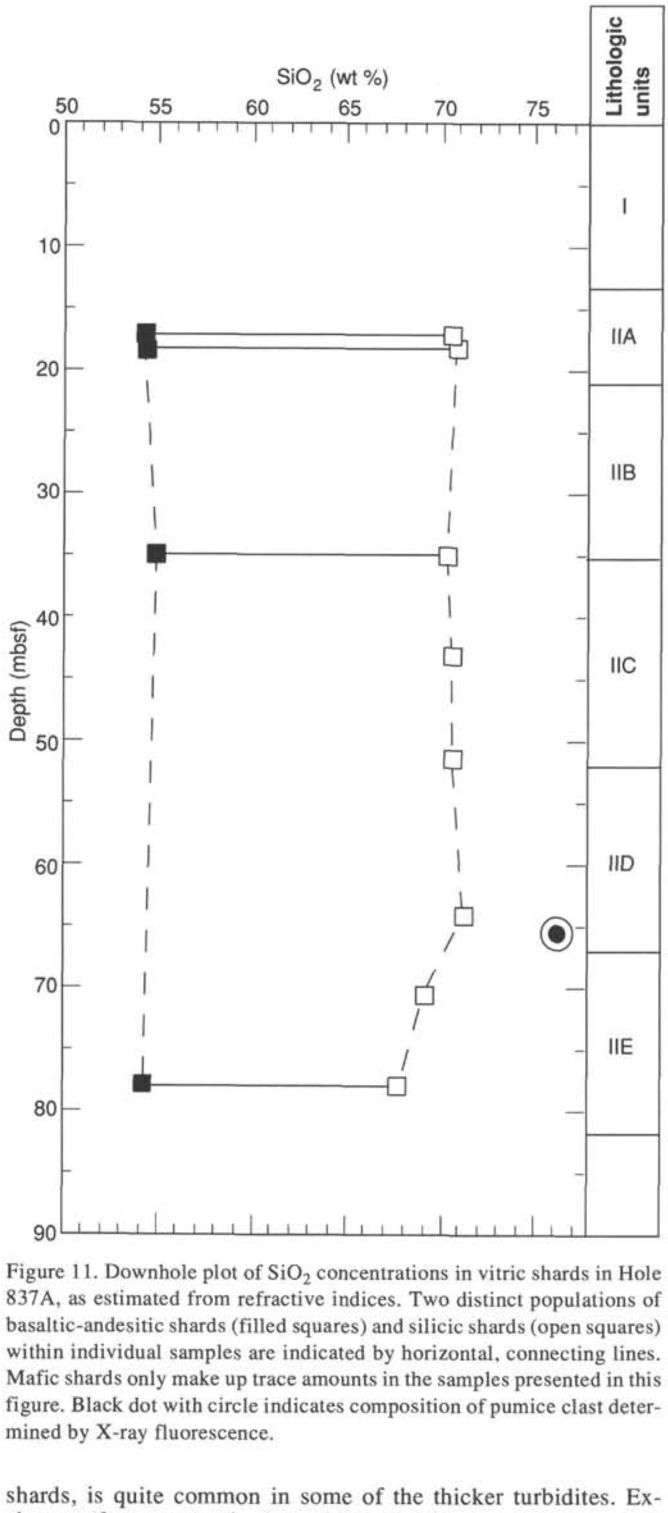

Figure 11. Downhole plot of SiO_2 concentrations in vitric shards in Hole 837A, as estimated from refractive indices. Two distinct populations of basaltic-andesitic shards (filled squares) and silicic shards (open squares) within individual samples are indicated by horizontal, connecting lines. Mafic shards only make up trace amounts in the samples presented in this figure. Black dot with circle indicates composition of pumice clast determined by X-ray fluorescence.

shards, is quite common in some of the thicker turbidites. Exchange of pore water in these thick, highly permeable beds was probably much more effective than in most of the deposits at Sites 834 and 835.

Volcaniclastic Sediments

Pyroclastic sediments

Rare, well-preserved tephra layers are restricted to the uppermost parts of Hole 837A. Three layers of thin, primary airfall deposits are found within Cores 135-837A-2H-4 and -2H-5 (Table 3). These are graded, with sharp, non-eroded bases. Two of the layers contain large fragments of highly vesicular pumice lying at the basal contact. Individual grains are typically angular and often show bubble wall and junction morphologies. Fibrous pumiceous shards containing tubular vesicles also occur.

Table 4. Refractive indices (n) and SiO_2 concentrations (estimated after Church and Johnson [1980] and Schmincke [1981]) of glass shards (63–36 μm size fraction) from turbidites in Hole 837A.

Core, section, interval (cm)	Depth (mbsf)	Comment	n	SiO_2 (wt%)
135-837A-				
2H-7, 30	17.3	Clear	1.508	70.5
2H-7, 30	17.3	Brown/green	1.574	54.2
3H-1, 87	18.37	Clear	1.507	70.8
3H-1, 87	18.37	Brown/green	1.574	54.2
4H-6, 52	35.02	Clear	1.509	70.3
4H-6, 52	35.02	Brown/green	1.571	54.8
5H-5, 58	43.08	Clear	1.508	70.5
6H-4, 77	51.27	Clear	1.508	70.5
7H-7, 6	64.06	Clear	1.506	71.1
8H-4, 103	70.53	Clear	1.513	69.1
9H-3, 55	78.05	Clear	1.518	67.7
9H-3, 55	78.05	Brown/green	1.574	54.2

Epiclastic Sediments

Unit I bears only small amounts of volcaniclastic sediments, whereas Unit II is dominated by thick volcaniclastic turbidites that often grade upward into nannofossil oozes. The subunits of Unit II represent different cycles of volcaniclastic sedimentation. Turbidites, averaging around 70 cm in thickness, are common in Unit II of Hole 837A, forming depositional sequences up to 17.1 m thick. The thickest sequences are found in the middle of Unit II, within Subunits IIB and IIC, at 27.1 to 52.3 mbsf. The variation of turbidite thicknesses with depth and time defines several discrete cycles that are especially well developed in Subunits IIA, IID, and IIE. Within these cycles the thickness of individual beds commonly decreases up-section.

Origin of the Volcaniclastics

The abundance of clear glass of rhyolitic composition (SiO_2 content up to 70%–71%) within turbidites of Hole 837A (Fig. 11) suggests derivation from a silicic magma source. At the present time, no such source is known to have existed close to the location of Site 837A. If the Lau Basin is reconstructed by removing 2 m.y. of crustal extension or formation on either side of the ELSC (assuming a 5–6 cm/yr of extension or formation), then a postulated proto-Tofua Arc would be situated immediately adjacent to Site 837; this arc could have been a source for the rhyolitic glasses. If the arc volcanism migrated across the basin during its 5–2 m.y. history, then arc constructs are likely to have developed from which silicic material could be derived.

Except for a few thin pyroclastic layers, the whole sequence at Site 837 is made up of volcaniclastic mass-flow deposits. It appears that the morphology of the Lau Basin, with numerous north-trending small basins and ridges, was a more important control on the distribution of volcaniclastics than was the distance to the source area. Although deep basins directly within the pathways of major turbidity currents have gained large volumes of coarse-grained volcanic detritus, others, which are sheltered behind submarine barriers, are starved in clastic sediments. The majority of the volcaniclastic sediments deposited at Site 837 may have been derived locally from horsts within the Lau Basin.

Depositional History

Sedimentation at Site 837 is dated as beginning in the late Pliocene, at about 2.0 Ma (see "Biostratigraphy" section, this chapter). The sediments were deposited directly onto basaltic lava at paleowater depths probably not greater than the present depth of 2500 m (see "Igneous Petrology" section, this chapter). Sediments at this site are dominated by epiclastic deposits, predominantly volcaniclastic sediment gravity flow deposits with interbedded clayey nannofossil oozes. Pyroclastic sediments comprise only a small proportion of the volcaniclastics, although proximity to an active arc system since the start of sedimentation is inferred.

Epiclastic turbidite sedimentation was almost unbroken throughout deposition of Unit II, after the end of eruption of mafic lavas. Apparent breaks in the trend occur with two thick turbidites in Subunit IIC and the lower part of Subunit IIB. Deposition of Unit II (approximately 2.0–0.5 Ma) occurred in pulses, with each event or sequence of events separated from its successor by a period of slow deposition, nondeposition, or even erosion. Longer lasting periods of slow deposition, resulting in intervals of clayey nannofossil oozes, occur in the middle part of Subunit IIE in the upper parts of Subunits IIE, IID, and IIB and in Unit I. The waning of volcaniclastic sedimentation at Site 837 probably relates to a cessation of active volcanism and, therefore, to reduced input of pyroclastic material to the source area for the turbidites. Sediments deposited from 0.5 Ma to the present are dominated by clayey nannofossil oozes representing hemipelagic sedimentation.

Pumice fragments occur scattered throughout the nannofossil oozes. Some of these may be derived from distal sources (Fisher and Schmincke, 1984). The thickness of (up to 17.1 m) and predominance of epiclastic turbidites may indicate that Site 837 lay within the pathway of a major sediment distributory system. The coarseness of turbidites also indicates, despite good sorting, that these are proximal deposits. It is evident from the sediments recovered at Sites 834–839 that, over short distances within the Lau Basin, large variations occur in the distribution pattern, composition, and sedimentary facies of the deposits. This can probably be ascribed to north-trending ridges acting as major barriers to sediment transport, with sediments being deposited in small, local basins between the ridges.

STRUCTURAL GEOLOGY

Sediments

Hole 837A penetrated sediment to a depth of 84 mbsf before encountering igneous rocks that may represent basement. Two lithologic units were recognized within the sedimentary section and are described in detail in the "Lithostratigraphy" section (this chapter). Unit I (0–13.5 mbsf) is dominated by clay/nannofossil ooze, and Unit II (13.5–83 mbsf) by volcaniclastic turbidites. The latter unit contains a large number of ash layers and vitric sands, including one exceptional sand-silt-graded turbiditic horizon 17 m in thickness. Dip measurements were made on these turbiditic horizons within Unit II, and these are presented in Figure 12. Orientation of the dip measurements to geographical coordinates was made using the methods described in the "Structural Geology" section of the "Explanatory Notes" chapter (this volume). The reoriented dips from Hole 837A are generally shallow and toward the east, with a wide dispersion of dip directions between north and south. Dip values plotted vs. depth for these data are shown in Figure 13.

With relatively few data, and in the absence of logging information, hypotheses to explain the disposition of the bedding are speculative. It is possible that the turbidite flows had a component of depositional dip, as proposed for the dipping strata measured at Site 835 (see "Structural Geology" section, Site 835 chapter). The localized clustering of dip directions at different depths (Fig. 13) might be attributed to deposition of turbidity flows with distinct paleocurrent directions at different times throughout the stratigraphic record.

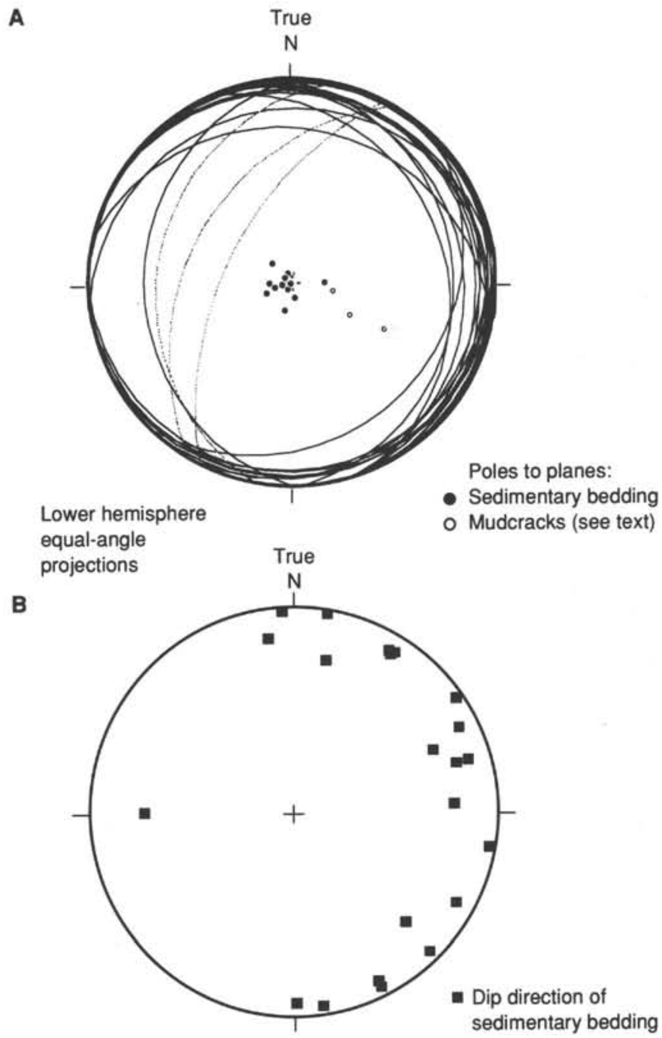

Figure 12. Lower hemisphere equal-angle stereographic projection of structural data from the sedimentary portion of Hole 837A. **A.** Great circles and poles to bedding of turbidite layers are illustrated by means of solid lines and circles, respectively. Nannofossil-ooze-filled extension fractures ("mudcracks") at 16 mbsf are marked by dotted lines and open circles (see text for discussion of their origin). N = 27. **B.** Plot of the dip direction of sedimentary bedding derived from the same data (filled squares); the mudcracks are not shown. N = 24.

Alternatively, the slight increase of average dip from the upper (0–20 mbsf) to the lower (50–80 mbsf) parts of the sedimentary succession could also be indicative of slight tilting of the sequence by a few degrees toward the east during deposition.

The stratigraphic levels intermediate between the more steeply dipping lower and gently dipping upper portions are dominated by the 17-m-thick turbidite flow mentioned above (see "Lithostratigraphy" section, this chapter), and no bedding planes were

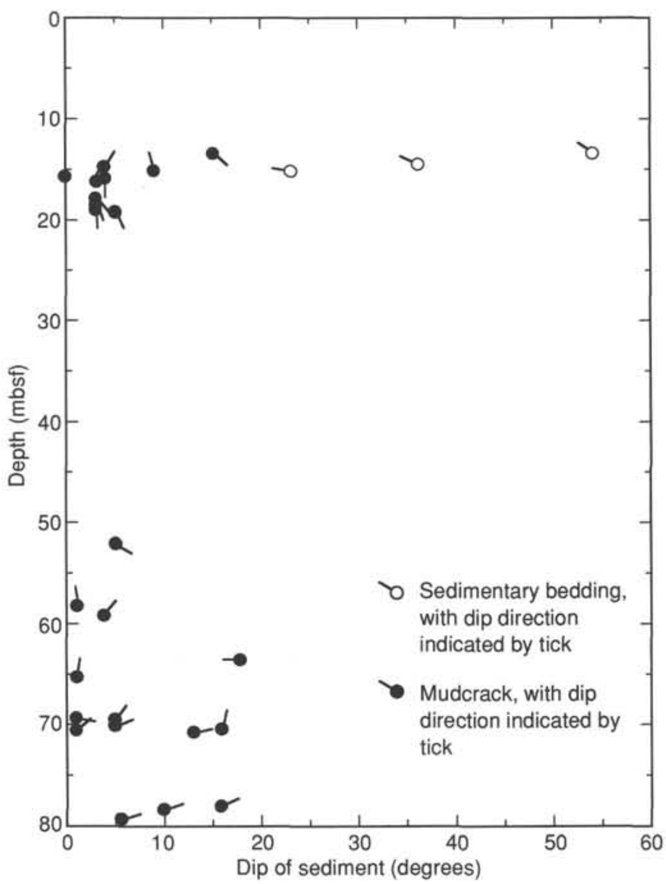

Figure 13. Dip of sedimentary bedding vs. depth, Hole 837A. The dip of individual measurements is given by their position relative to the *x*-axis of the diagram; dip directions are indicated by the direction of the ticks on each symbol. Ooze-filled mudcracks (see text) are indicated by open circles.

measurable. Although relatively fine grained, the turbidite is evidence for unusually rapid deposition (see "Sediment Accumulation Rates" section, this chapter) and is possibly also an indication of local tectonic activity.

At 16 mbsf in Hole 837A (135-837A-2H-6, 30–50 cm), gently dipping vitric turbidites are cut by a number of planar features inclined at a steep angle (ca. 40°–70°) to the bedding. The features are filled by poorly lithified soupy nannofossil ooze and intersect but do not offset bedding in the turbidite. Three of these ooze-filled cracks, 2–4 mm wide and spaced a few centimeters apart, increase in their dip upsection. Although the volcaniclastic layer is unconsolidated, it appears that it was nevertheless competent enough to fracture before injection of the ooze. The features are interpreted as extension fractures. They are coplanar and strike north-northeast, dipping toward the west. This trend is parallel to the direction of elongation of the basin within which Site 837 is situated and is also parallel to the possible axis of tilting of the sediments inferred above.

Igneous Rocks

Igneous rocks, which may represent basement, are present from 83 mbsf to the bottom of Hole 837B at 104.6 mbsf. The igneous rocks are traversed by a small number of steeply dipping joint planes for which no orientation data are available, as no demagnetization of igneous material from this site was undertaken during the routine shipboard paleomagnetic measurements.

BIOSTRATIGRAPHY

The biostratigraphic results for Sites 837A and 837B are summarized in Figures 14 and 15.

Calcareous Nannofossils

Pleistocene

Samples 135-837A-1H-CC and -2H-1, 97–102 cm, and Sample 135-837B-1R-CC contain floras including *Gephyrocapsa oceanica* but not *Emiliania ovata*. On that basis they are assigned to Subzone CN14b.

Samples 135-837A-2H-2, 11–12 cm, through 135-837A-6H-CC yield floras including *Emiliania ovata, Pseudoemiliania lacunosa,* and *Gephyrocapsa oceanica*. They are assigned to Subzone CN14a. The Pliocene flora *Discoaster brouweri* in Samples 135-837A-3H-CC and -4H-CC and *Calcidiscus macintyrei* in Sample 135-837A-4H-CC are thought to be reworked.

Pliocene

Samples 135-837A-7H-3, 60 cm, and -7H-6, 90 cm, contain floras including *Pseudoemiliania lacunosa, Emiliania ovata, Helicosphaera sellii, Calcidiscus macintyrei,* and *Gephyrocapsa caribbeanica* but not *Gephyrocapsa oceanica*. These samples are assigned to Subzone CN13b. Rare *Discoaster brouweri, D. pentaradiatus,* and *D. variabilis* identified in Sample 135-837A-7H-3, 60 cm, are reworked.

Sample 135-837A-7H-CC contains a sparse, moderately preserved flora including *Calcidiscus macintyrei, Pseudoemiliania lacunosa, Emiliania ovata,* and common small gephyrocapsids. This flora is sufficient to assign the sample to Zone CN13, but it is not possible to assign it to a subzone.

Floras including *Emiliania ovata, Pseudoemiliania lacunosa, Calcidiscus macintyrei,* and *Helicosphaera sellii* but not *Gephyrocapsa caribbeanica* are present in Samples 135-837A-8H-4, 110 cm, and 135-837A-8H-4, 120 cm. They are assigned to Subzone CN13a. Poorly preserved discoasters found in both samples and a single specimen of *Sphenolithus neoabies* in Sample 135-837A-8H-4, 120 cm, are considered to be reworked.

Sample 135-837A-8H-CC yielded an abundant, moderately preserved flora including *Emiliania ovata, Pseudoemiliania lacunosa, Calcidiscus macintyrei,* and *Helicosphaera sellii*. The flora also includes rare, poorly preserved specimens of *Discoaster triradiatus* and one poorly preserved specimen of *D. asymmetricus*. The *D. asymmetricus* is probably reworked, but it is possible that *D. triradiatus* is in place. On this basis, this sample is given a possible age assignment of Subzone CN12d. A sample from a thin sediment layer at the top of Section 135-837B-2R-1 presents a similar biostratigraphic problem as it contains a flora including *E. ovata, P. lacunosa, C. macintyrei,* and *H. sellii*. This flora also includes one poorly preserved specimen of *D. asymmetricus* and very rare *D. brouweri*. It is possible, in this stratigraphic position, that *D. brouweri* is in place. This sample is, therefore, given a possible age assignment of Subzone CN12d.

Samples 135-837A-9H-1, 125 cm, through -9H-CC contain floras including *Calcidiscus macintyrei, Helicosphaera sellii, Emiliania ovata, Pseudoemiliania lacunosa, Discoaster brouweri,* and in most cases, *D. triradiatus*. These samples are assigned to Subzone CN12d.

Planktonic Foraminifers

The planktonic foraminifer assemblages at Sites 837A and 837B are typically abundant and well preserved in most of the samples from the Pleistocene and late Pliocene. These assemblages, however, become less diverse in ash-rich sediments, and

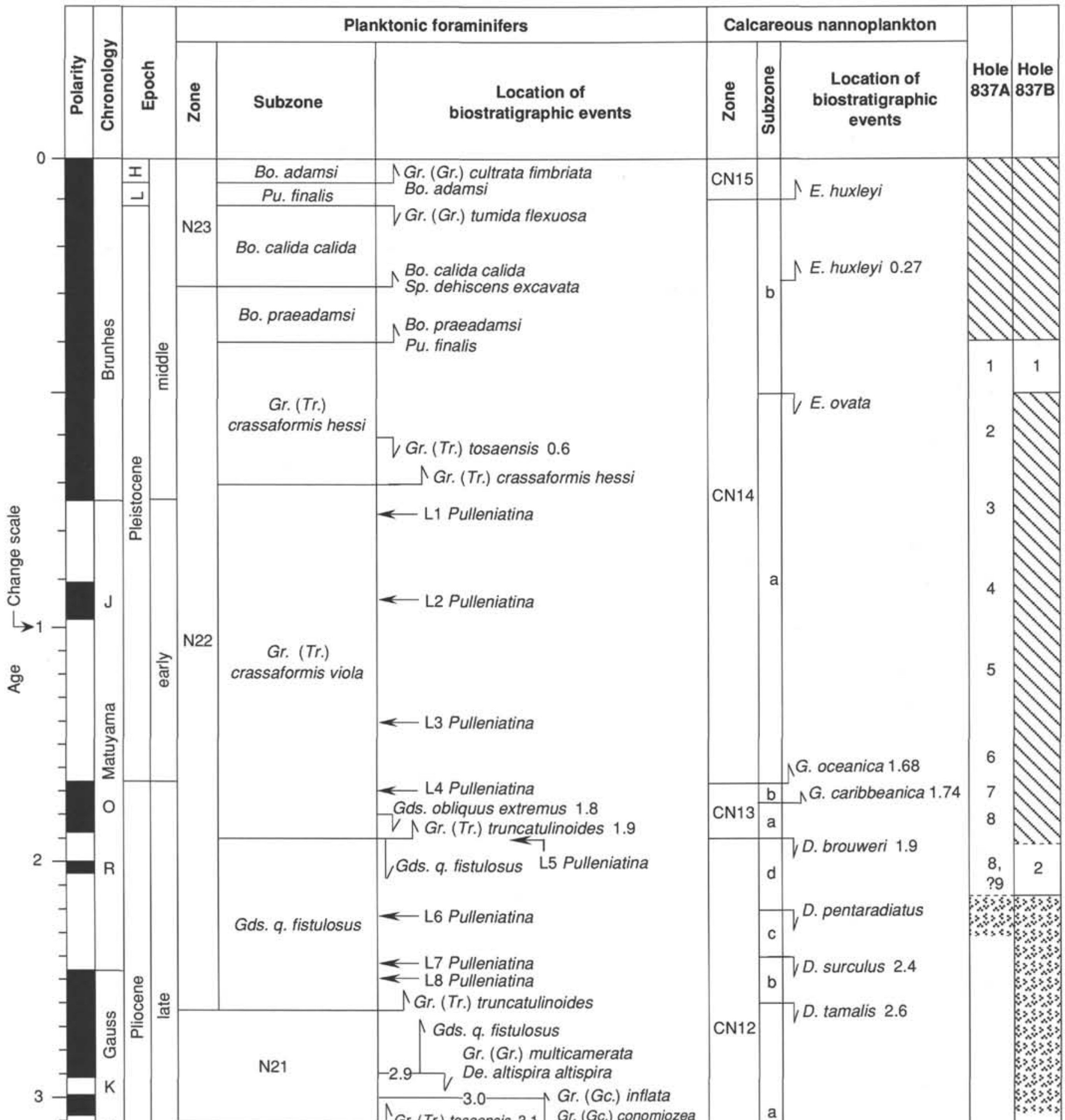

Figure 14. Biostratigraphic results, Site 837.

are absent from many of the ash horizons within the interval from 26 to 46 mbsf.

Pleistocene

Samples 135-837A-1H-CC through 135-837A-3H-1, 93–99 cm, and Sample 135-837B-1R-CC contain *Globorotalia (Truncorotalia) truncatulinoides* and *Gr. (Tr.) crassaformis hessi* without *Gr. (Tr.) tosaensis,* indicating the *Gr. (Tr.) crassaformis hessi* Subzone of Zone N22 (Chaproniere, in press).

The last appearance datum (LAD) of *Gr. (Tr.) tosaensis* occurs in Sample 135-837A-3H-5, 54–59 cm, marking the top of the *Gr. (Tr.) crassaformis viola* Subzone (Chaproniere, in press). This subzone ranges downhole to Sample 135-837A-8H-CC. Populations of *Pulleniatina obliquiloculata* are dextrally coiled through-

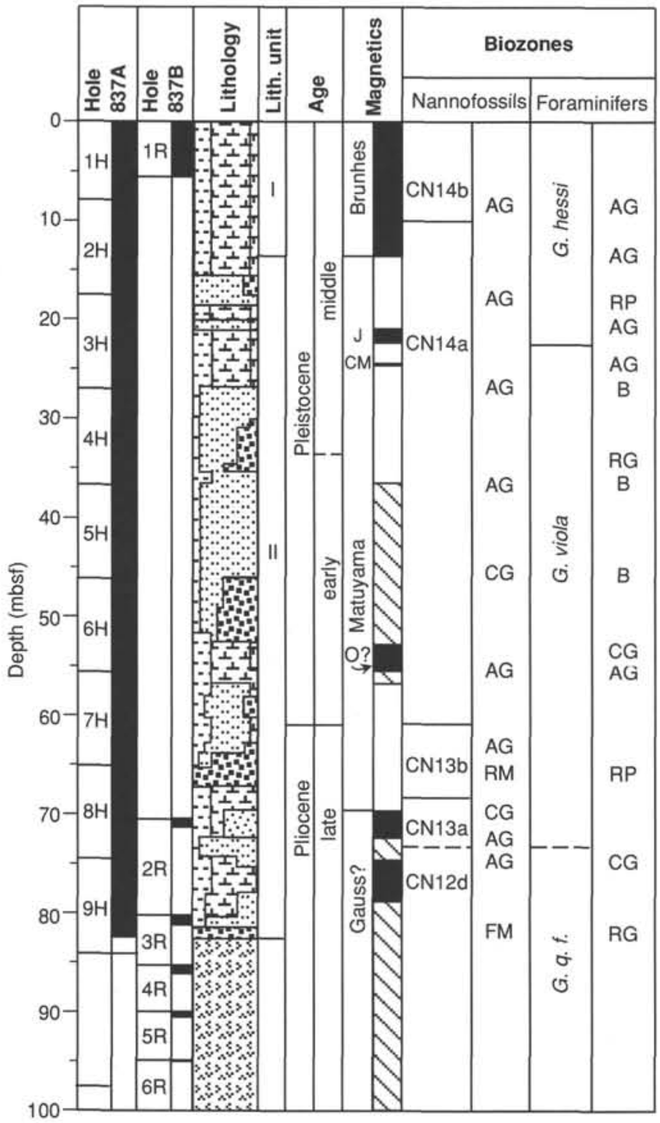

Figure 15. Paleontology summary chart, Site 837. See Figure 1 caption for an explanation of the symbols and abbreviations used.

out most of this interval, except for lowest Sample 135-837A-8H-CC, in which the population of this species is sinistrally coiled.

Pliocene

The LAD of *Globigerinoides quadrilobatus fistulosus* occurs in Sample 135-837A-8H-CC; this taxon is found only in one other sample, 135-837B-2R-CC. The presence of *Gr.* (*Tr.*) *truncatulinoides* and *Gr.* (*Tr.*) *tosaensis* with *Globigerinoides quadrilobatus fistulosus* in these samples indicates the *Globigerinoides quadrilobatus fistulosus* Subzone of Zone N22 (Chaproniere, in press). Populations of *Pulleniatina obliquiloculata* are sinistrally coiled in these samples, indicating the uppermost part of this subzone.

SEDIMENT ACCUMULATION RATES

Biostratigraphic and paleomagnetic data both indicate that the age of the sediments at Site 837 ranges from the middle Pleistocene to the latest Pliocene (Brunhes and Matuyama chrons). The sediment sequence consists largely of tuffaceous sands, with some interbedded calcareous ooze horizons. The amount of volcaniclastic material increases greatly downcore, being concentrated from the base of Core 135-837A-3H to within Core 135-837A-6H, an interval with little paleontologic control. Overall, the preservation and diversity of the planktonic assemblages are good, but moderate and poor faunal assemblages occur in the lower part of the sedimentary section.

Figure 16 is a graphical presentation of depth and biostratigraphic data from Site 837. Two sets of biostratigraphic data have been used; one based on the extinction level (LAD) of *Gr.* (*Tr.*) *tosaensis* at 0.6 Ma (Berggren et al., 1985a, 1985b), and the other with this event being placed at 0.9 Ma (based on the relationship between this event and the paleomagnetic data at both this site and Site 834). In addition, paleomagnetic data have been plotted with the biostratigraphic data. Both sets of data overlap for the top of the core, but they diverge from each other in the middle part and then are parallel to each other for the remainder of the hole.

The reliable paleomagnetic data show a sediment accumulation rate of about 19–42 mm/k.y. in the upper part of the hole, and the curve based on paleontologic data in Table 5 shows a similar average rate of about 38 mm/k.y. However, this fails to differentiate between the lower part of the sequence containing the thick tuffaceous beds below about 25 mbsf and the upper part that lacks these thick beds. Little difference is achieved by using the modified dating of the LAD of *Gr.* (*Tr.*) *tosaensis* event. The curve can be divided into two parts (A and B). If the 0.6-Ma LAD is used, the sediment accumulation rate is about 38 mm/k.y. for the upper part (B) and about 39 mm/k.y. for the lower part (A). Using the modified LAD of 0.9 Ma, the sediment accumulation rate is 25 mm/k.y. for B and 50 mm/k.y. for A. The plot using the modified LAD of 0.9 Ma fits the lithologic data more closely than the other curves.

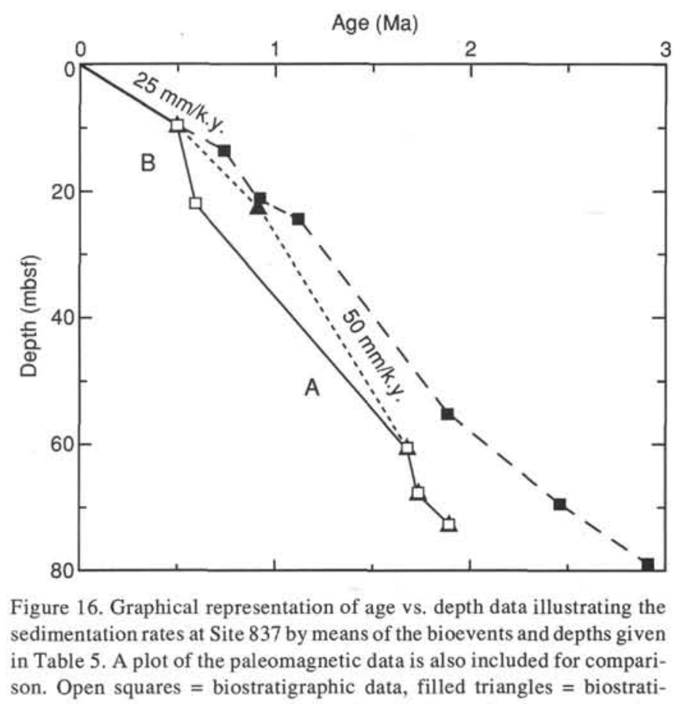

Figure 16. Graphical representation of age vs. depth data illustrating the sedimentation rates at Site 837 by means of the bioevents and depths given in Table 5. A plot of the paleomagnetic data is also included for comparison. Open squares = biostratigraphic data, filled triangles = biostratigraphic data with modified ages for *Globorotalia* (*Truncorotalia*) *tosaensis*, and filled squares = paleomagnetic data.

Table 5. Depths and ages of bioevents used to plot accumulation rates, Site 837.

Depth (mbsf)	Age (Ma)	Events
10.0	0.50	LAD *E. ovata*
22.5	0.60	LAD *Gr. (Tr.) tosaensis*
61.0	1.68	LAD *G. oceanica*
68.0	1.74	FAD *G. caribbeanica*
73.0	1.90	LAD *D. brouweri*

PALEOMAGNETISM

Remanent Magnetism

Most remanent magnetization measurements were made with the pass-through cryogenic magnetometer on archive halves of cores at a spacing of 5 cm. After measuring the natural remanent magnetization (NRM), sediment cores were subjected to alternating-field (AF) magnetic cleaning at 15 mT only, to speed the core flow through the laboratory. For basalt cores, a more detailed AF demagnetization sequence, with steps of 2, 5, 10, and 15 mT, was used. A few discrete sediment samples were further analyzed using the Molspin Minispin spinner magnetometer, the Schonstedt GSD-1 AF demagnetizer, and the Molspin pulse magnetizer to investigate their magnetic properties in greater detail.

Sediments in Cores 135-837A-1H through -9H were measured to determine magnetic polarity stratigraphy and remanent magnetization intensity. Because of the poor recovery and lack of suitably large basalt pieces, no segments or individual specimens of RCB basalt cores from Hole 837B were measured.

Magnetic Properties

Sediments at Site 837 are similar to those of Sites 834 and 835, with ash layers and volcaniclastics being abundant. The equivalent of Unit I in Hole 834A extends down to 25.8 mbsf, whereas Unit II of Hole 834A is equivalent to the lower part of Hole 837A (see "Lithostratigraphy" section, this chapter).

The sediment color is often dark reddish brown as a result of abundant iron, mainly contained in ferric oxyhydroxides (see "Lithostratigraphy" section, this chapter). Isothermal remanent magnetization (IRM) acquisition curves for three nannoplankton ooze samples (Fig. 17) show a rapid saturation with increasing field strength; 95% saturation is acquired at about 0.15 T in all cases, indicating that the magnetic grains within these sediments behave like magnetite.

The intensity of the sediments is relatively constant downhole, typically averaging 100 mA/m with a range between 10 and 300 mA/m. These strong magnetizations undoubtedly result from volcanic material in the sediments as well as from the propensity of the sediment to acquire a large drill-string-induced IRM. The pervasive upward overprint, which gives the sediments NRM inclinations near –90°, completely masks their intrinsic polarities. Notable peaks in NRM intensity between 700 and 3000 mA/m are found at the base of the ash layers.

The sediments acquired a strong drill-string IRM because many of their magnetic grains have low coercivities, as shown by the low mean destructive field (MDF) values, typically 2–4 mT, although some sediment samples have higher MDFs between 10 and 25 mT (Figs. 18 and 19). However, as it typically resides in low coercivity grains, this overprint is easily removed with AF demagnetization (Figs. 18 and 19), isolating more stable, characteristic remanences that hold geologic information.

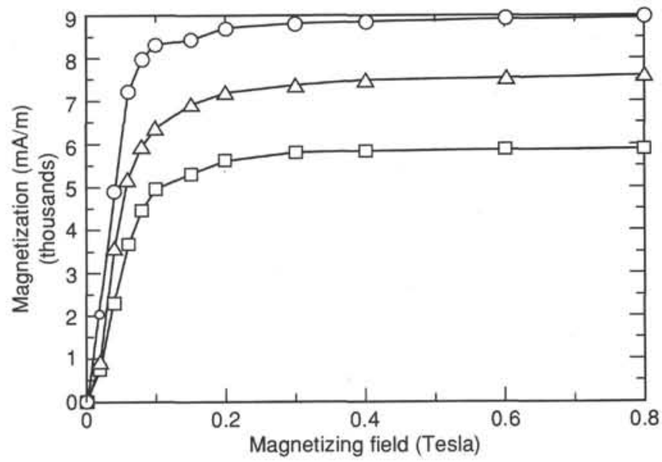

Figure 17. Isothermal remanent magnetization (IRM) curves for three sediment samples, Hole 837A. All three display saturation in low applied fields, indicating magnetite-type behavior. Open squares = Sample 135-837A-4H-1, 40–42 cm; open triangles = 135-837A-7H-2, 100–102 cm; and open circles = Sample 135-837A-9H-4, 72–74 cm.

Both samples shown in Figure 18 are from two major ash layers but show very different MDFs (2 and 15 mT). In both cases, the inclination changes sign from negative to positive (i.e., the polarity changes from normal to reversed). However, in the low-coercivity sample from Subunit IIB at 33.2 mbsf (see "Lithostratigraphy" section, this chapter; also Fig. 20), this shift requires a 20-mT AF demagnetization, whereas in the sample of higher coercivity from Subunit IIC at 41.20 mbsf (Fig. 20) this shift occurs at 4-mT AF demagnetization. Both ash layers show pronounced graded bedding (see "Lithostratigraphy" section, this chapter). The low-coercivity ash sample is from a relatively coarse-grained level about 2 m above the base of an 8-m-thick ash layer, and the higher-coercivity ash sample is from a level about 12 m above the base of the 18-m-thick ash layer. The graded bedding yielded highly scattered directional results in the pass-through magnetometer, perhaps caused partly by drilling disturbances but also by differences in the grain and domain size of the dominant ferromagnetic grains in the ash sediments and the 15-mT AF demagnetization limit.

As with sediments in Holes 834A and 835A, AF demagnetization above 30–40 mT removes the drill-string overprint to reveal a stable characteristic remanent magnetization. Again we must stress, however, that because AF demagnetization of the archive core halves during Leg 135 was limited to 15 mT, characteristic magnetizations may not always have been isolated and so the measurements made with the pass-through magnetometer must be regarded as reconnaissance results only.

Magnetic Polarity Stratigraphy

The sediments of Hole 837A showed a strong drill-string IRM masking the true NRM polarities, as did the sediments in previous Leg 135 holes. Nevertheless, 15-mT AF demagnetization usually revealed an interpretable polarity record. That the 15-mT level is not the optimum choice for these sediments is shown in Figure 20 by changes from positive to steep negative inclinations without coincident changes in declination, implying that the AF cleaning has been insufficient. Furthermore, there is a cleaning deficiency in the ash-dominated parts that may be dependent on sediment grain size.

At 14–21 mbsf the declination is well behaved, even though the inclination is highly scattered (14–21 mbsf) or changes gradu-

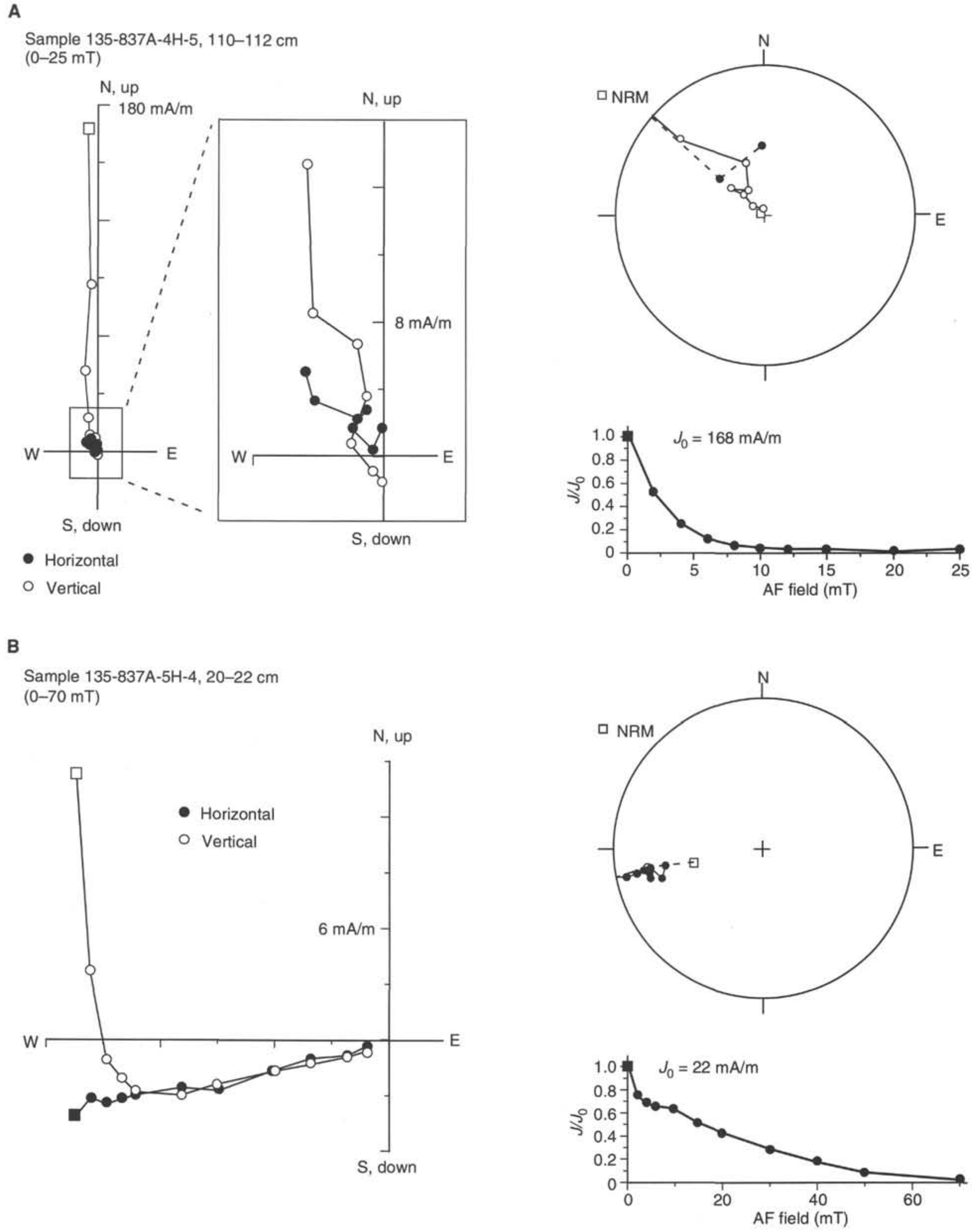

Figure 18. Behavior of two samples (**A–B**) of volcanic ash, Hole 837A, during alternating field (AF) demagnetization. In each set of plots, orthogonal vector plots, illustrated on the left-hand side, detail the directional behavior of the samples during AF demagnetization; on the upper right are stereographic projections of directions during AF demagnetization; and on the bottom right is a plot of normalized intensity decay. Much of the natural remanent magnetization (NRM) is thought to be an IRM induced by the drill string. J_0 is the NRM intensity for each sample. In Figures 18A and 18B, both samples show a polarity change, but at different AF fields: one high (20 mT) and one low (6 mT).

ally (27–35 mbsf). At 45–52 mbsf, within a large ash layer, coherent oscillatory swings are seen in both inclination and declination; at 36–44 and 56–65 mbsf, the inclination appears abnormally shallow for the site latitude. Indeed, the two major ash layers dominating the sediments between 28 and 54 mbsf may be responsible for much of this magnetically irregular behavior, caused by a gradual change of magnetic coercivities in the graded beds (e.g., 27–35 mbsf) as well as poor magnetic alignment resulting from coarse grain sizes (e.g., 45–52 mbsf).

In Figure 20 the observed polarity from Hole 837A is shown along with an interpretation into polarity chrons and subchrons. Because of the aforementioned effects, the polarity interpretation of Hole 837A was not as straightforward as that of Hole 834A, although apparently without the complicating repetitions of allochthonous units as occurred in Hole 835A. Reversed polarity is sometimes noted by a change from steep inclinations to values near zero. Declination switches usually show reversals, although in a few small sections there are changes in inclination without changes in declination. Such cases are assumed not to be reversals; they may be parts of the core for which the drill-string-induced IRM was not removed as completely. Apart from the ash layers, sediments analyzed from Hole 837A are generally less disturbed than are those from Hole 835A.

The top 14 m of Hole 837A is of normal polarity and undoubtedly belongs to the Brunhes Chron. Between 13.9 and 21.4 mbsf, the polarity is reversed, belonging to the top part of the Matuyama Chron. Two short normal polarity intervals at 21.4–22.7 and 24.3–24.7 mbsf, respectively, are interpretated as the Jaramillo Subchron and the Cobb Mountain Event (Mankinen et al., 1978; Clement and Robinson, 1987). Between 24.7 and 26.8 mbsf, the polarity is reversed, continuing the Matuyama.

Between 26.8 and 53.5 mbsf, the polarity is indeterminate because of the unclear patterns in declination and inclination; this is ascribed to the poor magnetic recording properties of the two major ash layers as discussed previously. Between 53 and 55.7 mbsf, the inclination is negative and the declination near 180°. This interval may be of normal polarity, possibly the Olduvai Subchron, or it may be an artifact. This interpretation is critical, for if we take this zone as the Olduvai, then the reversed zone beneath is the lower Matuyama. If not, the reversed zone must be the middle Matuyama. Moreover, this also determines whether the next normal polarity zone below is interpreted as the Olduvai Subchron or Gauss Chron. Between 55.7 and 69.6 mbsf, the polarity is reversed and may be interpreted as more of the Matuyama. Between 69.6 and 79 mbsf the polarity is normal, equivalent to either the top of the Gauss Chron or the Olduvai Subchron. Below 79 mbsf the polarity appears scattered, but Sample 135-837A-9H-4, 72–74 cm (Fig. 19), shows a stable reversed polarity above 6 mT and may correspond to either the top of the Kaena Subchron or the base of the Olduvai Subchron.

As described above, there are two potential interpretations of the observed polarities. Using the magnetic stratigraphy and the geomagnetic polarity reversal time scale of Berggren et al. (1985a, 1985b), an age vs. depth curve was constructed for the upper 82 mbsf of Hole 837A (Fig. 21 and Table 6). In Model A, we interpret an age of 2.92 Ma (top of the Kaena Subchron) at 79 mbsf, whereas in Model B we suggest an age of 1.88 Ma for 79 mbsf (base of the Olduvai Subchron).

Sedimentation rates deduced for different intervals of Hole 837A (Fig. 21) differ considerably according to which model is chosen. In both cases the rate of deposition in the Brunhes is 19 mm/k.y. and in the upper Matuyama, 42 mm/k.y. In Model A, the rates of deposition between the Cobb Mountain and Olduvai subchrons is 33 mm/k.y. and between the Olduvai and the top of the Kaena is 22 mm/k.y. However, the rates in Model B between the Cobb Mountain Subchron and the top of the Olduvai is 102 mm/k.y., and within the Olduvai it is 43 mm/k.y. Sedimentation accumulation rates derived on the basis of biostratigraphic data suggest sedimentation rates of 21 mm/k.y. for the top 18 m of Hole 837A (see "Sedimentation Accumulation Rates" section, this chapter).

If the two major ash layers between 27 and 53 mbsf are removed in the calculation of the rates of deposition, we end up with a mean rate in Model A between the Cobb Mountain and the top of the Kaena of 16 mm/k.y., as compared with a rate of 38 mm/k.y. between the Cobb Mountain and the Olduvai in Model B. The close equivalence between the Brunhes rate of 19 mm/k.y. and the ash-corrected rate of 16 mm/k.y. in Model A favors the latter as the more convincing.

Table 6. Measured magnetic polarity vs. depth, Hole 837A.

Depth (mbsf)	Polarity (N, I, R)	Age (Ma)	Chron/subchron		
0.0		0.0	BRUNHES		
	N				
7.8					
	I				
8.0					
	N		BRUNHES		
13.9		0.73			
	R		MATUYAMA		
21.4		0.91			
	N		Jaramillo		
22.7		0.98			
	R				
24.3		1.12			
	N		Cobb Mountain		
24.7		1.12			
	R				
28.5					
	R?				
35.3					
	R				
36.1					
	I				
46.0					
	R?				
47.3					
	I				
51.0					
	R?				
54.3					
	I				
55.7					
	R		Model A:	Model B:	
			MATUYAMA		
69.6		2.48		1.66	
	N		GAUSS		Olduvai (top)
72.9					
	I				
74.5					
	N				Olduvai (base)
79.0		2.92		1.88	
	R?		Kaena (top)		
80.0					
	R				
81.2					
	R?				
82.0					
			GAUSS (69.6 to >82.0 m)		

Notes: Interpretation of age and polarity chrons derived by comparison with the geomagnetic polarity reversal time scales (Berggren et al., 1985a, 1985b; supplemented with selected subchron ages from Harland et al., 1982, and Clement and Robinson, 1987). Models A and B are two possible interpretations for the deeper parts of the hole.

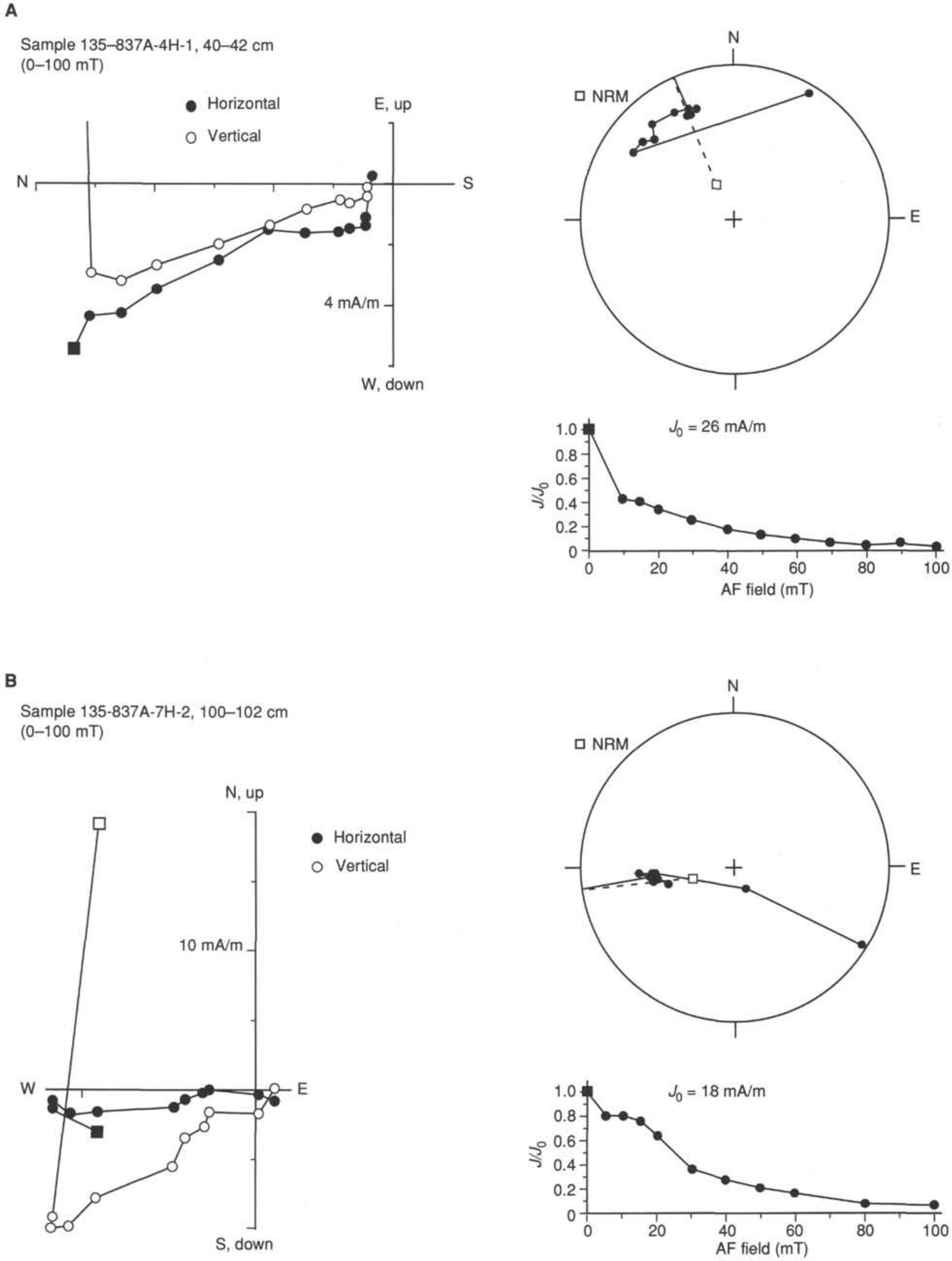

Figure 19. Behavior of three brown nannofossil ooze sediment samples, Holes 837A and 837B, during alternating field (AF) demagnetization (**A–C**). Figure conventions as in Figure 18. Much of the natural remanent magnetization (NRM) is thought to be an IRM induced by the drill string. All three samples change polarity but at different AF demagnetization levels. Furthermore, MDF are rather different: 10, 25, and 40 mT.

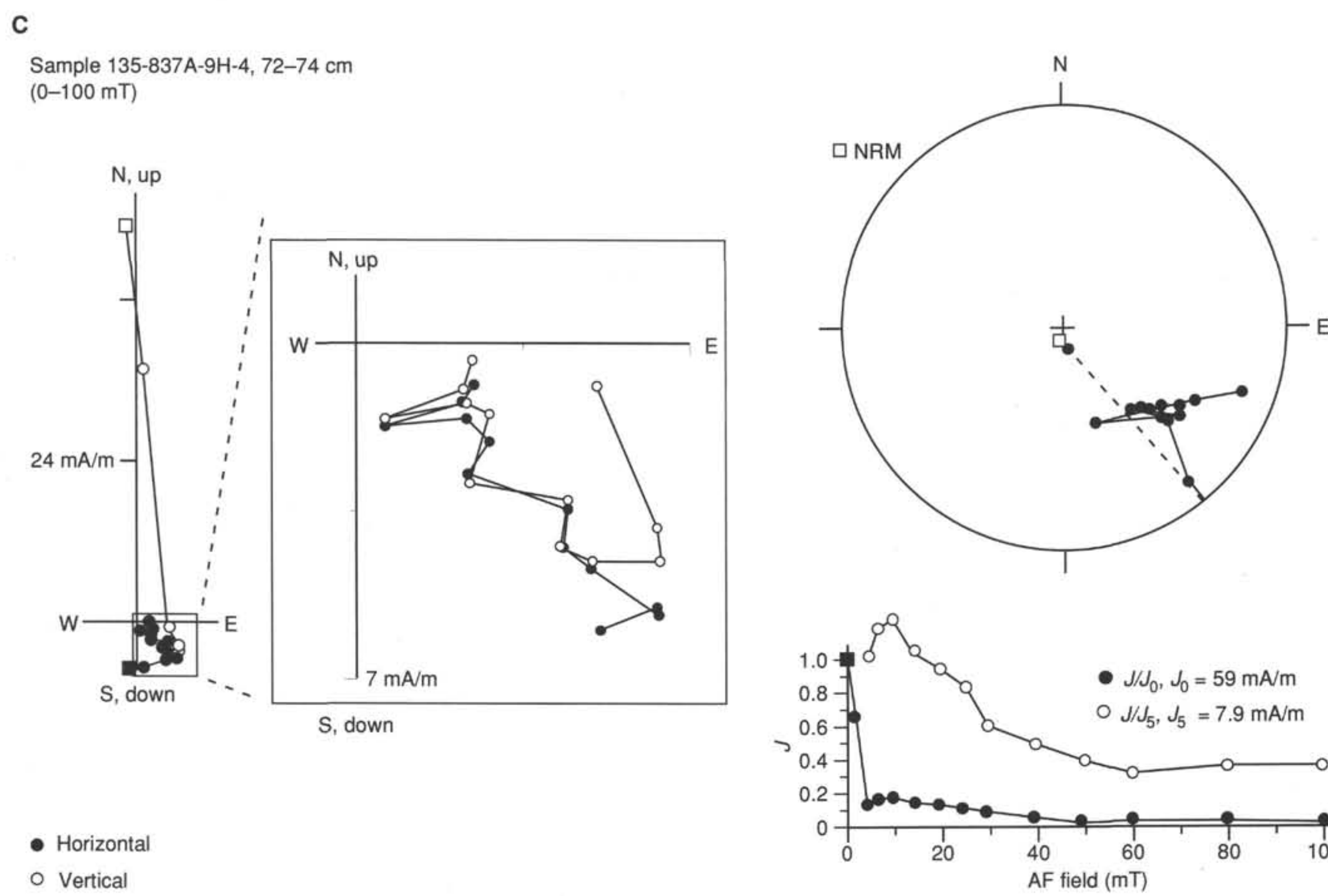

Figure 19 (continued).

Magnetic Susceptibility

Sediments

Volume magnetic susceptibility was measured on a routine basis on whole (i.e., unsplit) APC core segments of the sediments from Hole 837A, whenever the core sections appeared to be relatively full in cross sections. The measurements were done every 3 cm with a Bartington MS-2 susceptibility meter with a 100-mm sensor loop.

Volume magnetic susceptibility values in Hole 837A sediments (Fig. 22) range from about 10×10^{-6} to 1000×10^{-6} cgs, with typical values between 30×10^{-6} and 100×10^{-6} cgs (geometrical mean about 60×10^{-6} cgs). They display both long- and short-wavelength variations, although not in the same manner as was seen in the Hole 834A sediments.

Three major cycles in Unit I (0–13.5 mbsf) are seen, with high values at 2, 4–5, and 12–13 mbsf. The three spikes present in this unit correlate with the ash-rich layers. Unit II (13.5–82 mbsf) has been divided (see "Lithostratigraphy" section, this chapter) into five subunits (A through E). The lower half of Subunit IIB and the whole of Subunit IIC consists of two major ash layers, T1 and T2 (as illustrated in Fig. 22). These graded layers show a pronounced increase in susceptibility with grain size (see "Physical Properties" section, this chapter), decreasing by a factor of 15 from the coarsest to the finest grain size. Even the inverse grading at the base of T2 (see "Lithostratigraphy" section, this chapter) is also nicely matched by the gradual increase in susceptibility from 53 to 52 mbsf (Fig. 22). Other notable ash layers are matched by susceptibility peaks at 57, 59, 66, 67, 69, 70, 75.5, and 77 mbsf, respectively.

The modified Q-ratio (ratio between the 15-mT AF-cleaned intensity and the susceptibility) for the top 40 m of Hole 837A is shown in Figure 23. As was the case with the sediments of Holes 834A and 836A, a somewhat regular cyclicity in the Q-value is seen, with about 30 peaks in the top 24.5 m (this depth has a well-constrained age of 1.12 Ma, given by the Cobb Mountain Event; Fig. 21), equivalent to about 37 k.y./cycle, which is close to that expected from the Milankovitch obliquity (Berger, 1978; Ruddiman and McIntyre, 1981). Although this value is not as close to that expected as those in Holes 834A and 836A, it appears likely that Milankovitch cycles are also seen in Hole 837A.

Basalt

Few basalt susceptibility measurements were made because recovery in Hole 837A was poor. The susceptibilities show relatively constant values, typically between 700×10^{-6} and 1000×10^{-6} cgs, with the geometrical mean value about 800×10^{-6} cgs.

Core Orientation

Cores 135-837A-4H through -9H were oriented using the multishot camera (see "Explanatory Notes" chapter, this volume). Orientation data are given in Table 7.

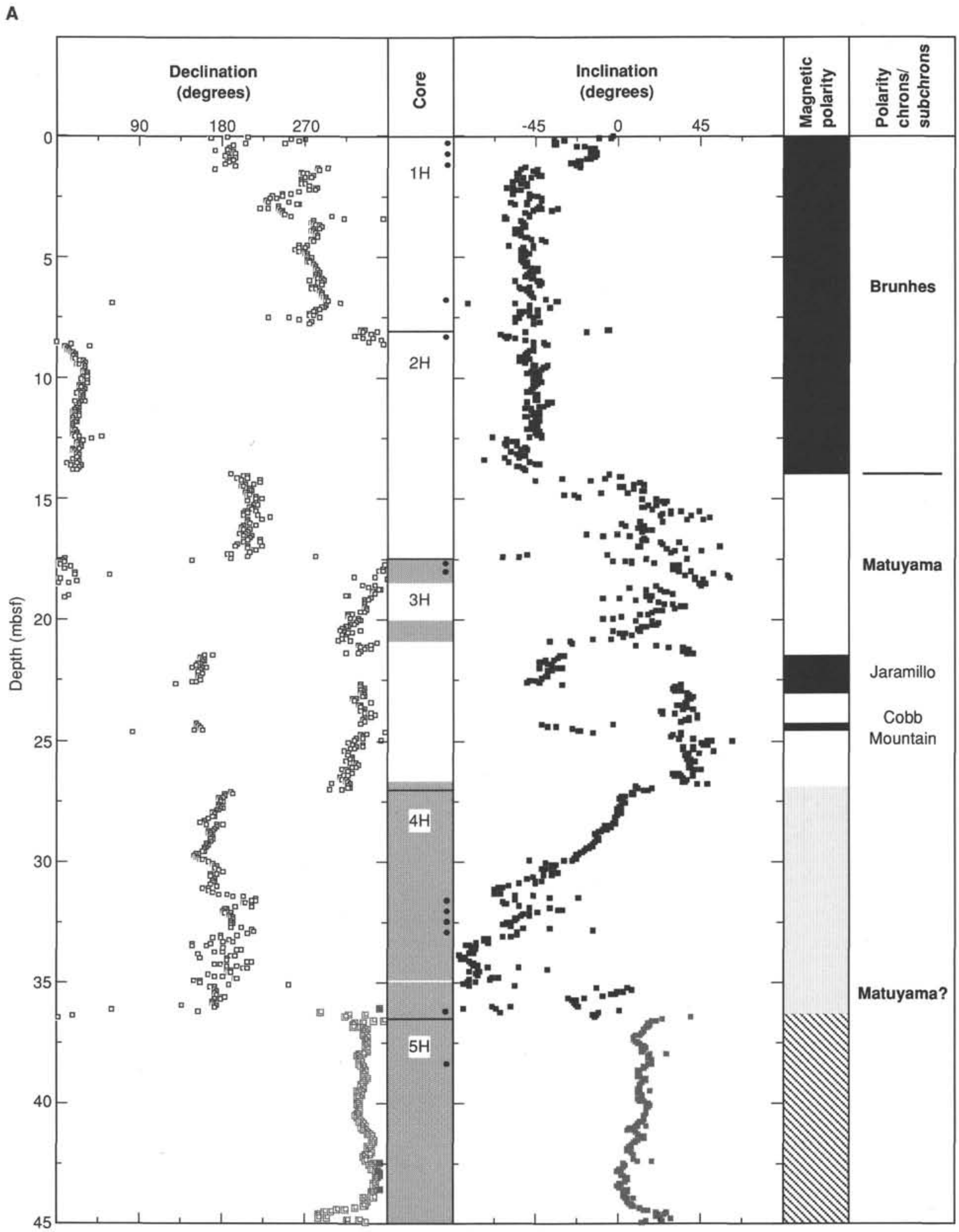

Figure 20. Magnetic polarity stratigraphy of Hole 837A. Wide columns at left and middle show the magnetization declination and inclination, respectively, after AF demagnetization to 15 mT by the pass-through cryogenic magnetometer. Column between declination and inclination plots indicates core boundaries, sections of core disturbed by drilling (dots), and ash layers > 50 cm thickness (gray). Columns at right show interpreted magnetic polarities; black = normal, dark gray = probably normal, hachured = indeterminate, light gray = probably reversed, and white = reversed (see Table 6). At far right, interpreted magnetic polarity chrons and subchrons are indicated. Bold type denotes polarity chron names and lines show polarity chron boundaries. Plain type indicates subchron names.

B

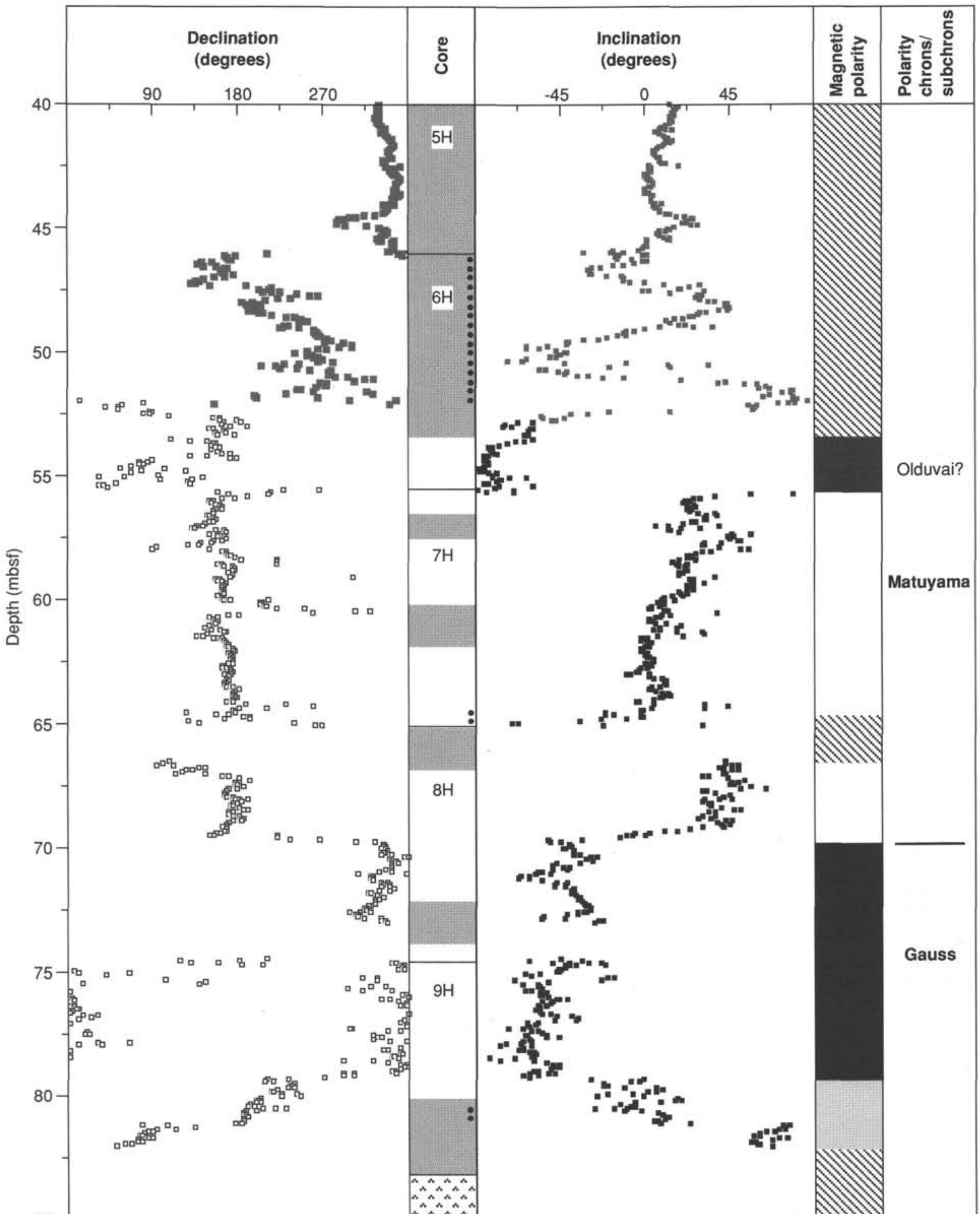

Figure 20 (continued).

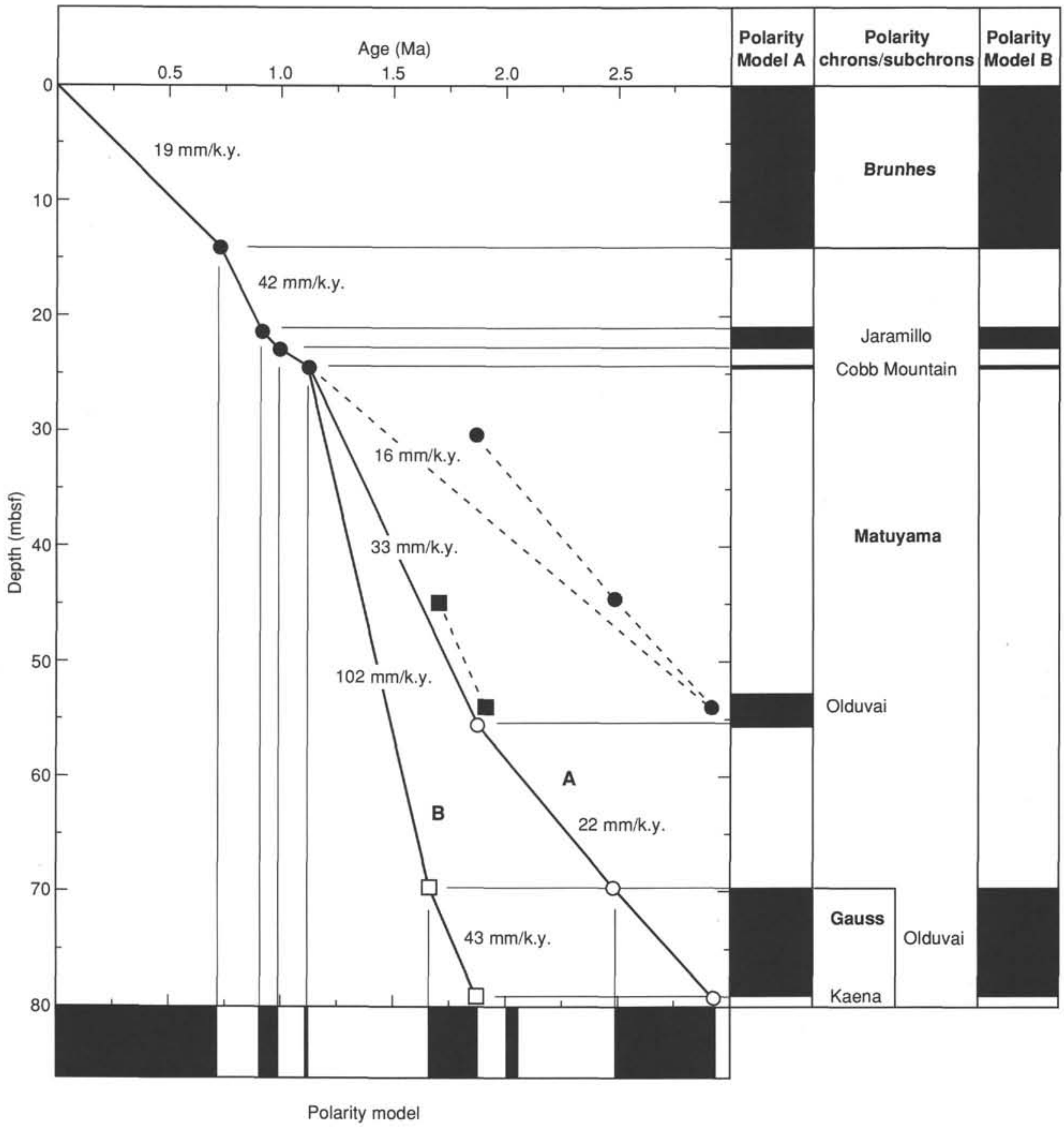

Figure 21. Age vs. depth in Hole 837A, constructed from magnetic polarity stratigraphy and geomagnetic polarity reversal time scale. Filled circles indicate points thought to be most reliable; hollow symbols show less reliable points. Observed polarity and two possible interpretations, Models A and B, are shown at right, with chron and subchron names indicated in bold and plain type, respectively. Numbers on line segments indicate calculated rates of deposition; dashed lines signify positions after subtraction of two major ash layers, as discussed in text. Polarity model is from Berggren et al. (1985a, 1985b), supplemented with selected subchron ages from Harland et al. (1982) and Clement and Robinson (1987).

INORGANIC GEOCHEMISTRY

Introduction

A total of six interstitial water samples were collected in Hole 837A. They were collected from every core in the uppermost 32 mbsf; below this depth, samples were taken every second core. The results are summarized in Table 8, and the depth chemical distribution is illustrated in Figure 24.

In Hole 837A, dissolved major constituents (chloride, sodium, calcium, magnesium, potassium, and sulfate) were determined. Magnesium concentrations were determined by two analytical methods (see "Explanatory Notes" chapter, this volume). Subsequent charge balance calculations yielded sodium concentrations. Ammonia, phosphate, silica, strontium, and manganese were also measured using colorimetric methods and flame AA spectrophotometry.

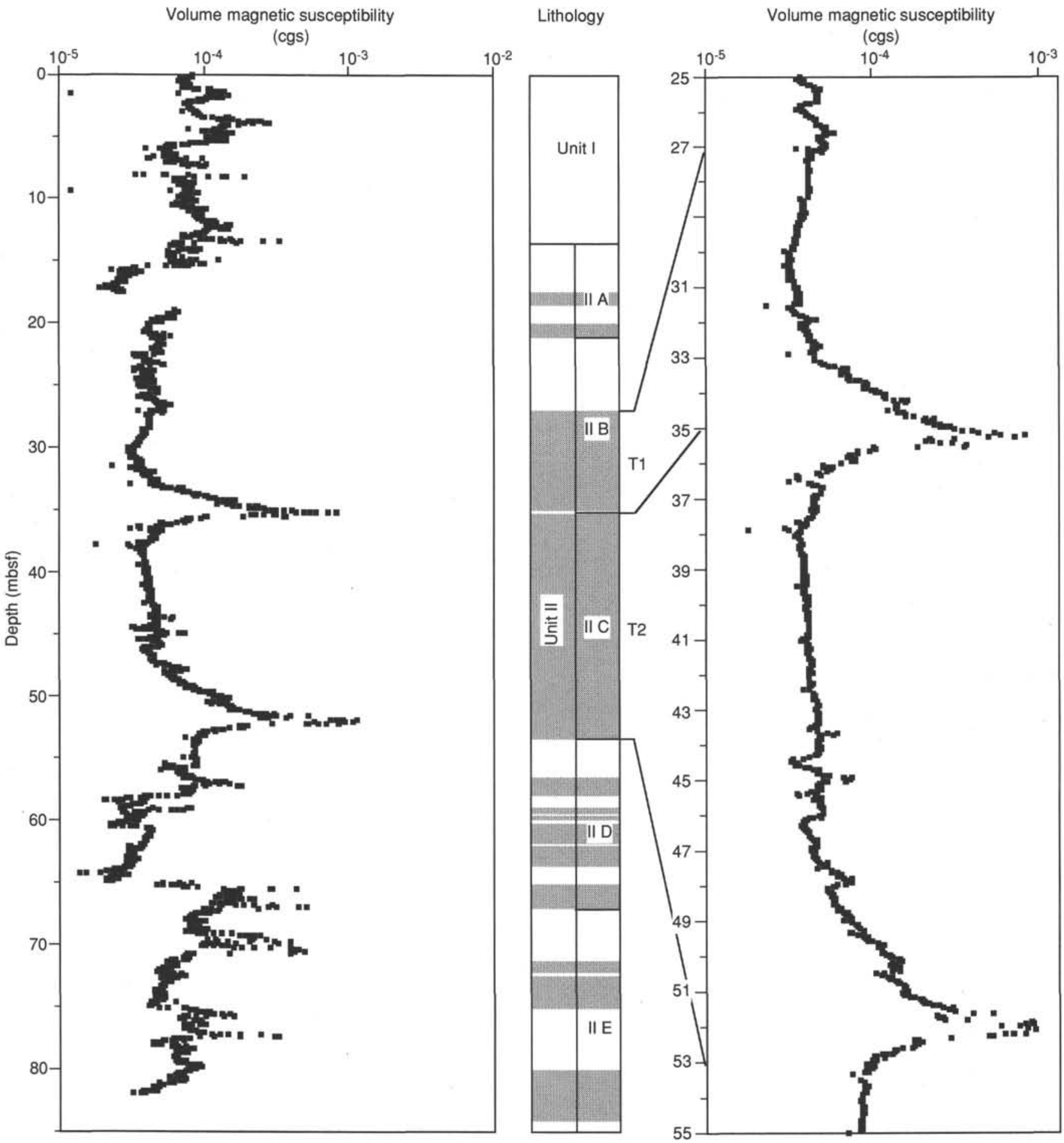

Figure 22. Volume magnetic susceptibility, Hole 837A. Columns at left and right show susceptibility values, plotted on a logarithmic scale. Middle column denotes lithostratigraphy of Hole 837A. Gray areas indicate sections of core containing ash layers. Column at right is an enlargement of the susceptibility plot for the interval from 25 to 55 mbsf that shows possible correlations between susceptibility spikes and the top and bottom of the large ash turbidite units.

Results

The chemical data in Hole 837A are similar to those obtained in Holes 834A, 835A, and 836A. The major constituent concentrations are similar to average values for seawater. The values of dissolved ammonia and phosphate concentrations are very low and consistent with the sulfate concentrations, which are fairly uniform with depth. The values of dissolved phosphate, silica, and strontium are comparable with those obtained in Holes 834A, 835A, and 836A.

The comparison between the low and uniform NH_4^+ concentrations and the scatter of PO_4^{3-} concentrations indicates that only a small amount of PO_4^{3-} is released from organic matter degradation. The manganese concentration-depth profile at Site 837

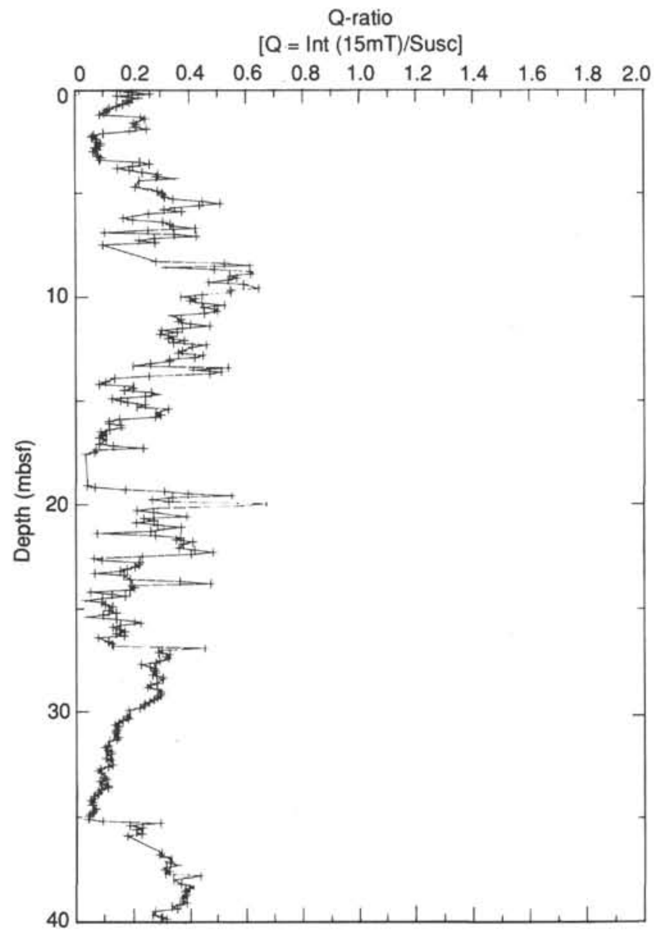

Figure 23. Modified Q values for the upper 40 m of Hole 837A. About 30 peaks are seen in the upper 24.5 m, which spans the last 1.2 m.y. according to the magnetic stratigraphy. The cycles in Q are probably Milankovitch cycles.

Table 7. APC core orientation data, Hole 837A.

Core no.	Camera no.	Compass	Inclination Direction	Inclination Drift	Declination
135-837A-					
4H	3209	A	N8°E	1°	185°
5H	3250	B	27°	1°	49°
6H	3250	B	25°	1°	194°
7H	3209	A	10°	1.3°	256°
8H	3209	A	0°	0.5°	87°
9H	3250	B	340°	1°	47°

Notes: Magnetic declination at site is 13°E. Compass B declinations must be corrected by adding 13° to observed core declination values.

shows a regular increase of Mn with depth. The Mn maximum reaches a value of about 87 μM at 71 mbsf and implies a release of Mn from solid phases.

Conclusion

The interstitial water chemistry data obtained in Hole 837A revealed the same chemical signatures that characterized the Hole 834A, 835A, and 836A and also suggest downwelling of bottom seawater to underlying basalt, with a low flow rate.

ORGANIC GEOCHEMISTRY

Shipboard organic geochemical analysis of samples from Hole 837A consisted of seven determinations of volatile hydrocarbons in sediments using the Carle gas chromatograph, 10 determinations of total nitrogen, carbon, and sulfur using the Carlo Erba NCS analyzer and 23 determinations of total inorganic carbon using the Coulometrics 5011 coulometer equipped with a System 140 carbonate/carbon analyzer. Details of the analytical procedures used are outlined in the "Organic Geochemistry" section ("Explanatory Notes" chapter, this volume) and are described in detail by Emeis and Kvenvolden (1986).

The volatile hydrocarbon gases were obtained from the bulk sediment using the head-space sampling technique and were routinely monitored for methane, ethane, and propane. Samples were taken from the first eight APC cores with the exception of Core 135-837A-4H, which contained predominately volcanic sands and silts. Methane concentrations in all the samples were between 2 and 3 ppm, which is very low and at the laboratory background level. Ethane and propane were not detected. The extremely low concentration of methane indicates that methanogenesis is not occurring in these sediments. An important factor at this site could be the very low levels of organic carbon (see below) present in these sediments, which might not be enough to sustain microbial activity.

Determinations of inorganic carbon (IC) contents were performed on the samples used for physical properties and on additional samples selected by the sedimentologists. Percent $CaCO_3$ is calculated according to the equation:

$$CaCO_3 = IC \cdot 8.334.$$

This equation assumes that all the carbonate is present as calcite. The data from these analyses are presented in Table 9. Carbonate values range from <1.9% to 66.1%. The very low carbonate values correspond to samples collected from volcanic sand/silt intervals. This is discussed in more detail and related to the lithologic units in the "Lithostratigraphy" section of this site chapter.

Also shown in Table 9 are the percentages of total carbon and sulfur for the ten samples measured. Sulfur content was also measured, but it was not detected in any of the samples analyzed. Total organic carbon (TOC) is defined here as the difference between the total carbon and the inorganic carbon values. The sediments from Site 837 have organic carbon contents between 0.00% and 0.27% and hence are considered too low for analysis by the Rock-Eval instrument. Only one sample of volcanic sand was analyzed for total carbon (13.31 mbsf) and, as expected, this contained 0.0% TOC. A considerable proportion of these sediments, corresponding to the volcanic sand/silt intervals, can be expected to have zero or an extremely low TOC content. Consequently, such lithologies were not sampled for these analyses. This is the reason, for example, that no data are is provided in Table 9 between depths of 32.18 and 57.71 mbsf. Some of the samples with high carbonate contents also contained extremely low TOC contents. TOC content, therefore, displays no correlation to depth or percentage of carbonate. Nitrogen was only detected in low concentrations in two of the samples analyzed.

IGNEOUS PETROLOGY

Introduction

Site 837 is situated 69 km west of the ELSC and was selected because it is in a location likely to give information about chemi-

Table 8. Interstitial water chemistry data, Hole 837A.

Core, section, interval (cm)	Depth (mbsf)	pH	Alkalinity (mM)	Salinity	Ca^{2+} (mM)	Mg^{2+} (1) (mM)	Mg^{2+} (2) (mM)	K^+ (mM)
135-837A-								
1H-3, 140–150	4.5	7.59	3.380	34.7	10.3	52.7	54.7	11.6
2H-4, 140–150	14.0	7.59	2.951	35.0	10.1	52.5	53.8	10.9
3H-4, 140–150	23.5	7.45	2.749	35.8	10.2	52.0	53.0	10.8
4H-4, 140–150	31.5	7.97	3.027	35.8	10.8	54.0	55.2	9.8
6H-4, 140–150	53.5	7.68	2.594	34.2	10.1	52.2	52.6	11.9
8H-4, 140–150	71.0	7.82	2.521	36.0	10.2	52.9	53.1	11.8

Core, section, interval (cm)	Cl^- (mM)	SO_4^{2-} (mM)	NH_4^+ (μM)	PO_4^{3-} (μM)	Si^{4+} (μM)	Sr^{2+} (μM)	Mn^{2+} (μM)	Na^+ (1) (mM)	Na^+ (2) (mM)
135-837A-									
1H-3, 140–150	545	28.9	8	4.8	278	101	27.4	465	462
2H-4, 140–150	549	29.3	9	2.1	289	97	28.4	471	469
3H-4, 140–150	552	29.0	5	2.3	305	98	55.8	475	473
4H-4, 140–150	553	29.8	8	1.2	295	110	52.0	473	471
6H-4, 140–150	554	28.9	6	2.6	320	107	70.9	475	474
8H-4, 140–150	555	29.6	9	2.4	311	101	87.0	476	474

Notes: Mg (1) derived from EDTA titration; Mg (2) is determined by flame AA spectrometry; Na (1) derived from charge balance calculations using Mg (1); Na (2) used those of Mg (2).

Table 9. Concentrations of inorganic and organic carbon and total nitrogen, Hole 837A.

Core, section, interval (cm)	Depth (mbsf)	Total carbon (%)	Inorganic carbon (%)	Organic carbon (%)	$CaCO_3$ (%)	N (%)	OrgC/N
135-837A-							
1H-2, 80–81	2.3	5.47	5.46	0.01	45.5		
1H-4, 78–79	5.28	5.24	4.97	0.27	41.4	0.27	1
1H-6, 7–8	7.57		6.55		54.6		
1H-CC, 9–10	7.86		6.10		50.8		
2H-2, 74–76	10.24		6.75		56.2		
2H-4, 81–82	13.31	6.34	6.34	0	52.8		
2H-6, 99–100	16.49		0.56		4.7		
3H-6, 69–70	25.69	7.97	7.94	0.03	66.1		
4H-2, 65–66	29.15	0.52	0.52	0	4.3		
4H-4, 68–69	32.18		0.23		1.9		
7H-2, 71–72	57.71	7.81	7.70	0.11	64.1		
7H-3, 70–71	59.20		3.54		29.5		
7H-4, 71–72	60.71		2.59		21.6		
7H-6, 101–102	64.01		0.89		7.4		
8H-2, 25–26	66.75		0.54		4.5		
8H-2, 86–87	67.36	6.37	6.25	0.12	52.1		
8H-4, 66–67	70.16		4.92		41.0		
8H-6, 81–82	73.31		0.70		5.8		
9H-1, 27–28	74.77		0.70		5.8		
9H-1, 76–77	75.26	7.39	7.22	0.17	60.1	0.21	0.81
9H-1, 130–131	75.80	6.89	6.85	0.04	57.1		
9H-2, 76–77	76.76		7.08		59.0		
9H-4, 63–64	79.63	5.63	5.43	0.20	45.2		

cal/petrologic transitions between arc-like and MORB-like magma series.

Approximately 4 m of vesicular, sparsely to moderately phyric, orthopyroxene-clinopyroxene-plagioclase basaltic andesite were recovered from Site 837. Recovery of the igneous rock was poor (only 13% in Hole 837B), but it yielded very fresh material. Hole 837A was drilled to 82.5 mbsf, with no recovery of igneous rocks. Hole 837B, 20 m away, recovered igneous rocks in Core 135-837B-2R from 70.64 to 99.6 mbsf (Fig. 25). The good core recovery in Hole 837A makes it unlikely that igneous rocks were cored but not recovered. The difference in depth to igneous rock in the two adjacent holes may result from deposition on a sloping surface, offset on a fault, or from an irregular depth of emplacement because of the mode of magma eruption or injection.

The volcanic rock recovered is a sparsely to moderately phyric orthopyroxene-clinopyroxene-plagioclase basaltic andesite. The nominal thickness of basaltic andesite is 24.4 m (or 28.96 m if the whole of Section 135-837B-6R-1 is included). Macroscopically, the unit has plagioclase, pyroxene, and rare olivine as phenocrysts. Plagioclase forms fresh, tabular to equant euhedral phenocrysts, up to 5.5 mm across, varying between <1% and 3% in abundance. Fresh pyroxene phenocrysts, up to 1.2 mm across, comprise 1%–2% of the rock. Trace amounts of phenocrystal olivine, up to 0.7 mm across, are also present. The phenocrysts are set in a dark gray, fine-grained, vesicular groundmass with 10%–20% vesicles. There is a glassy rim on Piece 4 in Section 135-837B-5R-1. Additional very fine-grained samples include Pieces 1, 8, 12, and 13 in Section 135-837B-2R-1; Pieces 1, 7,

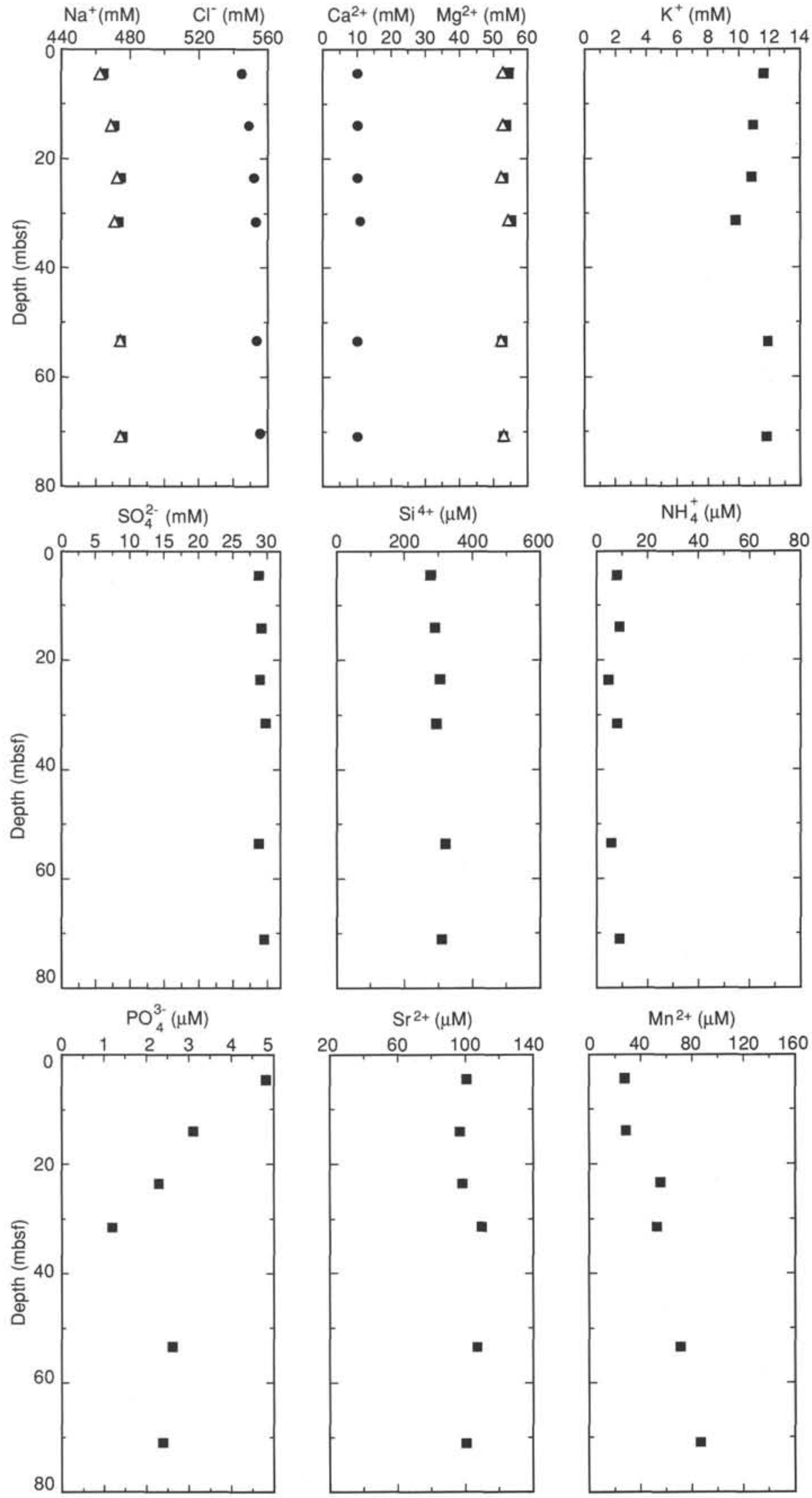

Figure 24. Concentration vs. depth profiles for chloride and sodium, calcium and magnesium, potassium, sulfate, ammonia, phosphate, silica, strontium, and manganese, Hole 837A.

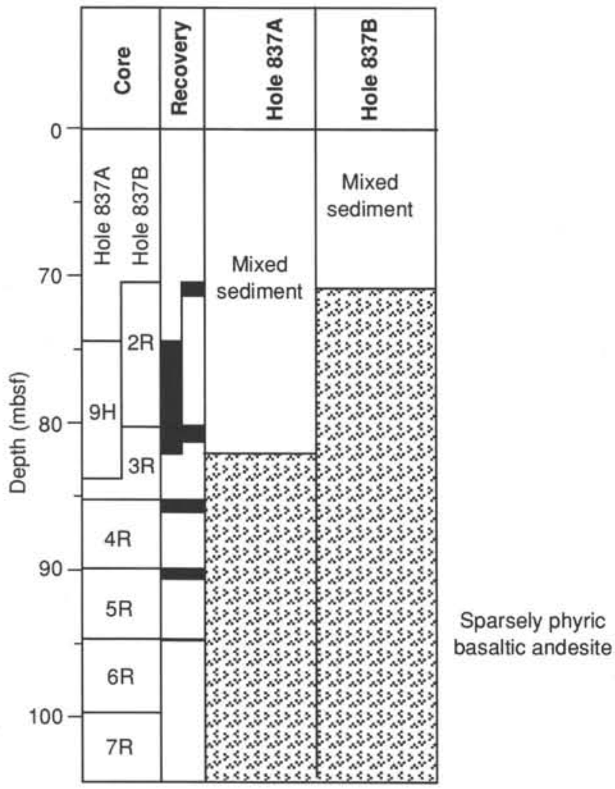

Figure 25. Schematic summary of igneous lithologic units recovered at Site 837. Note the discrepancy in the depth to igneous basement as inferred from core recovery at Holes 837A and 837B. Although no basalt was recovered in Hole 837A, the black shading is included in the "Recovery" column for Core 135-837A-9H to indicate that the discrepancy in depth to basement is not a function of poor recovery.

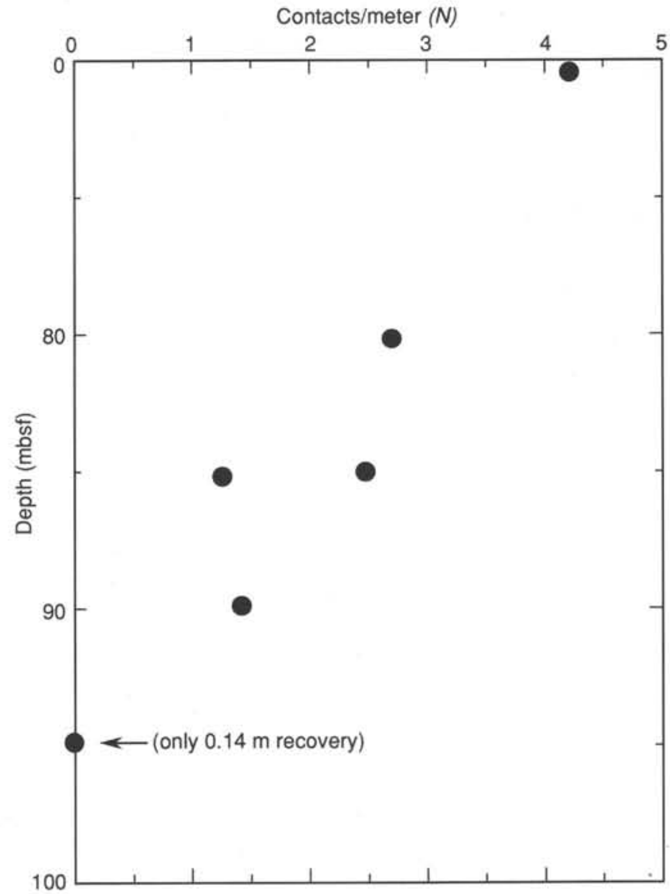

Figure 26. Data for cooling unit contacts per meter, plotted by section, for cores from Hole 837B. Recovery from Section 135-837B-6R-1 was too low to yield a reliable estimate. Methodology is discussed in the "Igneous Petrology" section, "Site 834" chapter (this volume).

and 17 in Section 135-837B-3R-1; Piece 1 in Section 135-837B-4R-1; and Piece 10 in Section 135-837B-5R-1. The abundance of these fine-grained fragments suggests the presence of multiple cooling units within the rock. The number of contacts (glassy margins, chilled margins) per meter of recovered core decreases downsection, suggesting an increase in the thickness of cooling units (Fig. 26).

Conspicuous features of the rocks are fine-scale planar laminae defined by vesicle concentrations, which have orientations predominantly subhorizontal or dipping at 10°–30° (Fig. 27). These occur as thin layers (1–2 mm wide) that are darker in color than the surrounding basalt and contain slightly larger vesicles than occur elsewhere in the rock. These structures are likely to have developed along internal flow laminae during emplacement of the lavas, suggesting that these rocks may represent a sheet flow or series of sheet flows. Vesicles are generally <0.5 mm. Some have been partially filled or lined with highly vesiculated quenched lava (Fig. 27).

The core is fresh to only very slightly altered. Some brownish discoloration is evident in Pieces 5–7 of Section 135-837B-5R-1 and is likely to be the result of low-temperature oxidative alteration. Vesicle linings are confined to rare brownish clay, red-brown iron-oxyhydroxides, and small encrustations of zeolite. These are most conspicuous in Section 135-837B-5R-1. Occasional encrustations of similar material are observed on fragment surfaces. These altered surfaces may represent the remnant margins of small filled fractures that were broken during drilling.

Petrography

Site 837 volcanic rocks are assigned to a single lithologic unit that is a sparsely phyric orthopyroxene-clinopyroxene-plagioclase basaltic andesite. Representative modal analyses are given in Table 10. Euhedral plagioclase phenocrysts (1%–2%) range in size from approximately 0.5 up to 1 mm, giving the rock a seriate porphyritic texture. Plagioclase phenocrysts are characterized by resorbed cores, scalloped edges, incipient alteration to fine-grained clays, and overgrown rims with abundant glass inclusions (Fig. 28). Normal zoning with distinct narrow rims of sodic compositions are evident on some phenocrysts. Rare (~1%), subhedral-euhedral equant to elongate clinopyroxene (<1 mm) forms phenocrysts, occurring both as isolated grains and in small glomeroporphyritic clusters with plagioclase phenocrysts. Twinning and sector zoning are relatively common among the largest clinopyroxene grains. Orthopyroxene most commonly occurs as euhedral crystals (0.2–0.3 mm) in some cases with clinopyroxene rims. The clinopyroxene to orthopyroxene ratio is approximately 3:1. Preliminary microscope studies suggest that olivine may be a rare constituent, forming irregular, subrounded xenocrysts(?) up to about 0.3 mm in length. No orthopyroxene reaction rims were observed on the olivine.

The groundmass dominantly comprises cryptocrystalline mesostasis but plagioclase (20%), pyroxene (7%–10%), and magnetite (5%–7%) can be identified. Euhedral plagioclase laths are up

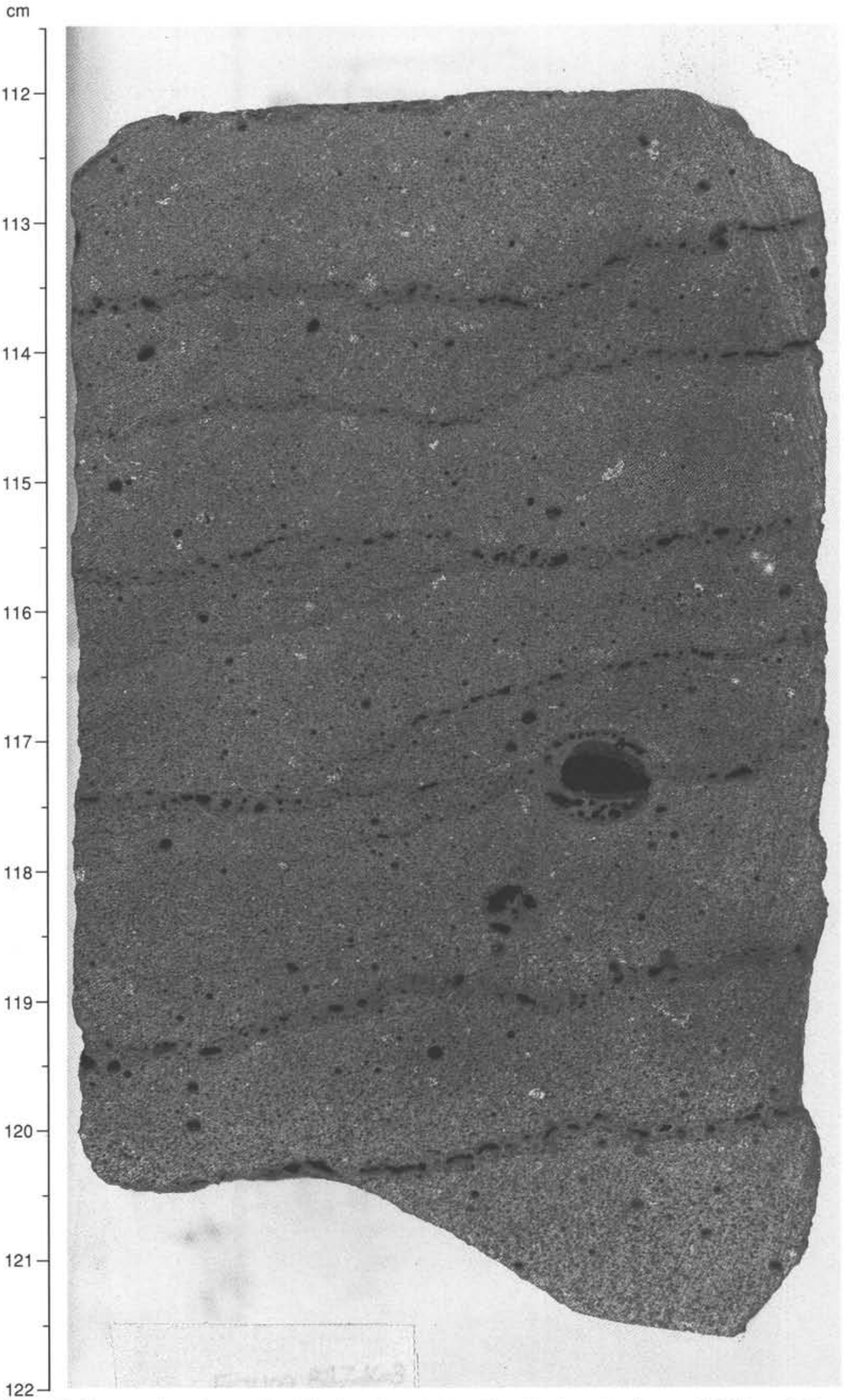

Figure 27. Closeup view of a sample of the basaltic andesite with subhorizontal stringers of highly vesicular, quenched material; Section 135-837B-2R-1, 111.5–122 cm, Piece 17.

Table 10. Modal analyses (>800 point counts) of representative samples from Hole 837B.

Hole	873B	837B
Core	2R-1	5R-1
Interval (cm)	24–26	60–69
Piece	2	8
Unit	1	1
Depth (mbsf)	70.7	90.4
Phenocrysts:		
Plagioclase	1.3	1.1
Clinopyroxene	0.4	0.7
Olivine	Trace	Trace
Orthopyroxene	Trace	Trace
Total phenocrysts	1.7	1.8
Vesicles:		
Open vesicles	15.2	13.6
Filled vesicles	—	2.1
Total vesicles	15.2	15.7
Groundmass:		
Plagioclase	18.9	19.9
Pyroxene	7.6	11.2
Olivine	—	—
Opaques	5.7	4.7
Mesostasis	50.4	46.2
Total groundmass	82.6	82.0
Plag/cpx (phenocrysts)	3.2	1.6

Notes: Phenocrysts were generally identified as larger, more blocky or tabular crystals. Several of the samples are seriate porphyritic and the phenocrysts grade in size into the groundmass laths.

to 0.5 mm in length and commonly show swallowtail terminations indicative of rapid growth. Clinopyroxene typically forms small (<0.2 mm) equant grains but it also occurs as acicular and plumose-quenched crystals commonly intergrown with quenched plagioclase. The amount of orthopyroxene in the groundmass is difficult to determine, but it is present as small, euhedral-subhedral laths. Magnetite is an abundant groundmass phase, occurring both as large, equant grains (0.1–0.2 mm) throughout the rock and as a major constituent of the mesostasis as skeletal grains (<0.1 mm). The large equant magnetite grains are commonly associated with glomeroporphyritic clusters of clinopyroxene and plagioclase and could be considered microphenocrysts. Ilmenite is absent as a primary phase, but it occurs rarely as lamellae in the large magnetite grains. Spherulitic- to variolitic-textured interstitial mesostasis makes up nearly 50% of the rocks. The mesostasis is extremely fresh and includes intersertal patches of tan-colored glass.

The vesicle content of the basaltic andesite ranges from 15% to 20%, and subrounded vesicles are as large as 3 mm across. Apart from those occurring along local alteration fronts, the vesicles are empty and commonly have thin linings of fresh glass. Along alteration fronts, vesicles are lined or filled with amorphous material ranging in color from yellow to orange to brown, which is tentatively identified as clays and iron-oxyhydroxides. Stringers of highly vesicular, dark, glassy material (0.5 mm wide) with quenched crystallites occur at about 1-cm intervals through some portions of this unit. These are very similar in appearance to the globular-shaped melt segregation vesicles described from previous sites, except that they appear to be oriented in planes throughout the rock. We interpret these stringers as having some relationship to magma flow.

Alteration

Macroscopically, alteration is restricted to the formation of iron-hydroxides and light brown clays along fractures. Globular encrustations of zeolites(?) can be discerned lining the walls of some vesicles. However, except for minor breakdown of some of the largest plagioclase grains, the rock is extremely fresh. Glassy patches are preserved in the mesostasis and, as noted above, glassy linings are present in many vesicles. Rarely, alteration minerals (dark red iron-hydroxide or yellow smectites) rim vesicles. Patchy replacement of mesostasis by yellowish and reddish clays is also rare and localized.

Geochemistry

All samples are termed low-K basaltic andesites using classification schemes based on their total alkali ($Na_2O + K_2O$) and SiO_2 abundances (e.g., Taylor et al., 1981; Table 11). The rocks are significantly fractionated relative to basalts at other sites nearby, with MgO contents of 3.4–3.5 wt%, Ni < 6 ppm, and Cr below the lower limit of detection. The high whole-rock Fe_2O_3* and V contents indicate that fractionation of magnetite from the magma was not extensive. The low Zr, Ti, and Y in these evolved rocks indicates that the parental magmas had even lower abundances of these elements. This implies derivation from a mantle source very depleted in incompatible elements. The compositional similarity of the two samples supports designation of the recovered core as a single unit.

Table 12 lists selected analyses for rocks from nearby areas that have similar high SiO_2 and low MgO. However, the closest match (from the Lau island arc series of Naitauba) has significantly lower TiO_2, Fe_2O_3*, and K_2O and higher Al_2O_3, K_2O, and P_2O_5 compared with the Site 837 rocks. Therefore, the rocks at Site 837 display a stronger Fe and Ti enrichment (tholeiitic trend) with fractionation than the arc samples. Sample 10-1-1 from the Central Lau Spreading Center (CLSC) shows much greater Fe and Ti enrichment than the Site 837 rocks, but it has significantly lower SiO_2. In contrast, Sample D1-5 from the Valu Fa Ridge (Jenner et al., 1987) is very similar in composition to the Site 837 basaltic andesites. The Site 837 samples are also similar to the andesitic hyaloclastite recovered at Site 836 (Fig. 29). In addition, a major element analysis of a glass sample (RNDB-15-29-6; Hawkins, 1989) dredged from near the propagating rift tip of the CLSC is comparable to the composition of the Site 837 rocks (Table 12).

In a more general way, Figure 29B illustrates how the trace element signature of the Site 837 basaltic andesites is transitional between modern Lau Basin basalts (from the active spreading centers) and the arc rocks from the Tonga-Kermadec group. The less incompatible elements shown (i.e., Nb-Y) more closely reflect the modern spreading center compositions, whereas the enrichment in Rb, Ba, and K, including the marked depletion in Nb relative to K, is more representative of island-arc magmas. The transitional nature of the Site 837 rocks is further illustrated in plots of Ba and Y vs. Zr for the various groups (Fig. 30). Note the position of the Site 837 samples between the fields for the arc and modern backarc rocks.

Despite their evolution to low MgO contents, the trace element signatures of the basaltic andesites from Site 837 show clear evidence for an influence of a mantle source similar to that proposed for arc magmagenesis. The strong decoupling between Rb, Ba, K, and Nb is distinct from element patterns for MORB.

Although the origin of the pumiceous material for Site 837 is unknown at this time, the trace element signature displayed in Figure 29C shows some strong similarities to that of the basaltic andesites from this site (e.g., the marked enrichment in large-ion-lithophile elements [LILE] over Nb). In contrast, Sr, P, and Ti are

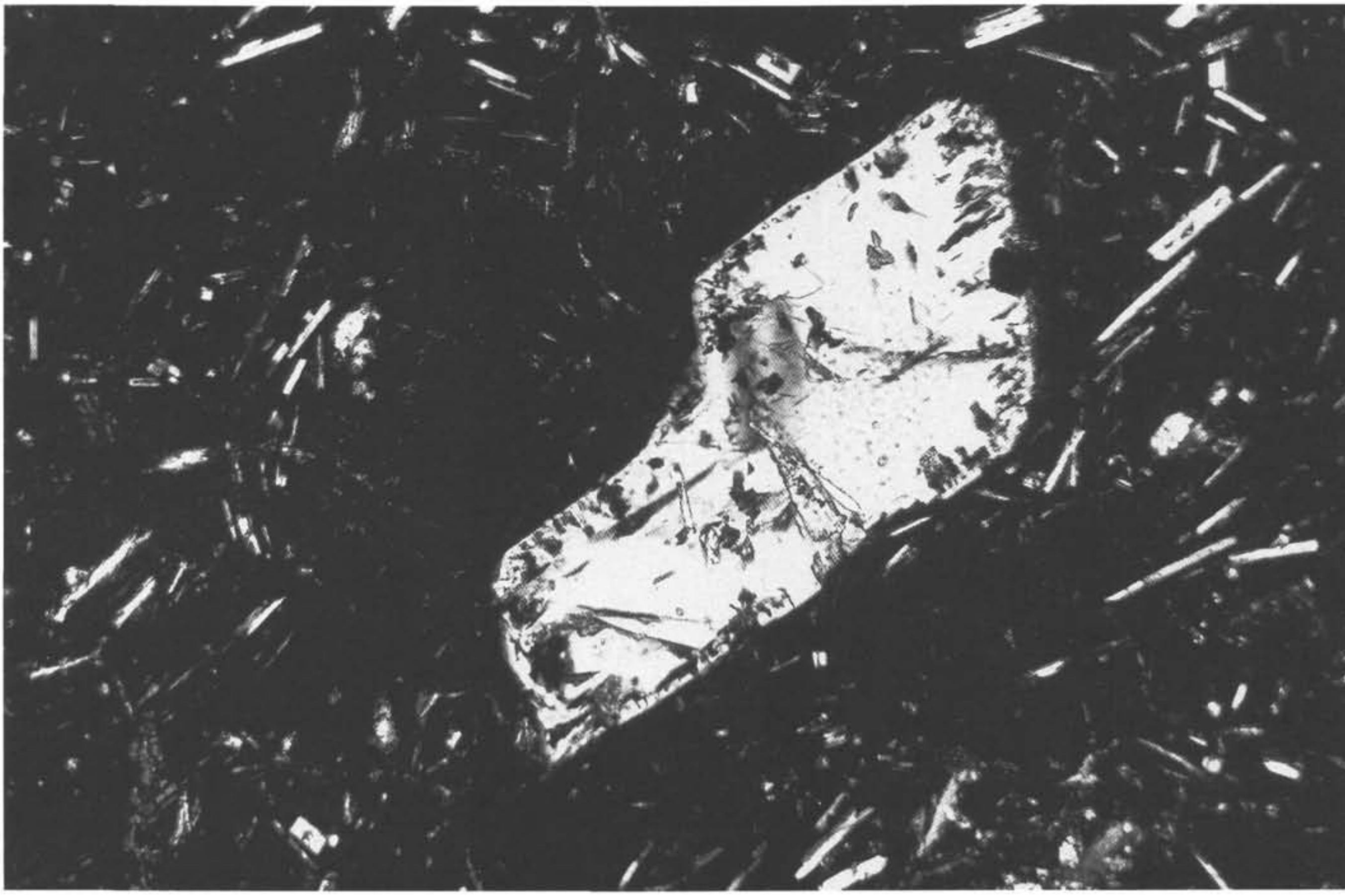

Figure 28. Photomicrograph of a partially resorbed plagioclase phenocryst illustrating a concentration of glass inclusions around the rim; Sample 135-837A-3R-1, 26–29 cm; field of view = 1.5 mm, crossed polars.

all relatively low in the pumice. This is consistent with extensive plagioclase fractionation and removal of apatite and oxides from this highly evolved material.

PHYSICAL PROPERTIES

Introduction

A full suite of standard ODP physical properties measurements was made at Site 837. Index properties on sediments and sedimentary rocks from Holes 837A and 837B were determined by using a pycnometer and balance and include bulk density, grain density, porosity, water content, and void ratio. Bulk density was also measured using the continuous gamma-ray attenuation and porosity evaluator (GRAPE) on full APC cores from Hole 837A. Two samples selected from the 34.6 m of basalt recovered from Hole 837B were run through the 2-min GRAPE process to determine bulk densities. These samples were also powdered, and the weight and volume of the dried powder were determined to yield grain density.

Compressional wave velocities were measured on whole cores using the continuous *P*-wave logger and on discrete samples using the Hamilton Frame apparatus. Velocities of unconsolidated sediments that could not be removed from the core liner were measured in only one direction. Velocities were measured in both horizontal and vertical directions when possible in unconsolidated sediments and on most of the consolidated sedimentary rocks and basalts.

Vane shear strength was measured on selected undisturbed intervals of the core samples from Hole 837A until the sediment became too stiff (when cracking of the sediment indicated that the assumption of uniform shear by the vane was no longer valid) or when degrees of rotation exceeded 90°.

Thermal conductivity was measured on undisturbed sediment cores from Hole 837A and on two basalt samples from Hole 837B.

The lithologic units referenced in this section are those described in the "Lithostratigraphy" section (this chapter). Results from laboratory measurements are listed on Table 13 and plotted on Figures 31–39.

Index Properties

Hole 837A

Wet-bulk density, grain density, water content, porosity, and void ratio for sediments and sedimentary rocks from Hole 837A are plotted vs. depth in Figure 31, and values for the gravimetrically determined index properties are listed in Tables 13 and 14.

The bulk density from Hole 837A sediments averages 1.45 g/cm^3, ranges between 1.29 and 1.64 g/cm^3, and increases only slightly downhole with little variation around the mean. The sediment grain density from Hole 837A averages 2.57 g/cm^3 and shows more variation downhole than the bulk density, although the gradient is essentially zero. Sediment water content averages 125% and ranges between 90% and 140%; porosity averages 78% and ranges between 71% and 85%; and void ratio averages 3.7 and ranges between 2 and 5. Trends in water content, porosity, and void ratio, all based on weight and pycnometer-measured volume, show significant variability and similar trends downhole. High values in the water content, porosity, and void ratio are

Table 11. Analyses of representative samples from Site 837.

Hole	837B	837B	837A
Core	2R-1	5R-1	8H-1
Interval (cm)	24–30	62–69	108–116
Depth (mbsf)	70.74	90.52	66.08
Major elements (wt%):			
SiO_2	54.40	55.93	77.16
TiO_2	1.34	1.36	0.44
Al_2O_3	14.56	14.86	12.50
Fe_2O_3	12.81	12.52	2.46
MnO	0.21	0.21	0.11
MgO	3.38	3.45	0.59
CaO	7.92	8.08	2.16
Na_2O	2.62	2.62	4.19
K_2O	0.66	0.72	1.68
P_2O_5	0.16	0.17	0.06
Total	98.06	99.92	101.32
LOI	0.96	1.45	5.55
Mg#	34.3	35.3	
Trace elements (ppm):			
Nb	3	2	3
Zr	75	76	164
Y	35	36	52
Sr	155	167	143
Rb	9	12	25
Zn	103	106	52
Cu	39	40	16
Ni	2	5	1
Cr	0	0	0
V	332	311	19
Ce	17	7	36
Ba	75	98	286

Notes: The sample from Section 135-837A-8H-1 was taken from a pumice horizon within the sedimentary sequence. The small (up to 1 mm across) fragments were leached overnight in a 0.5 vol% acetic acid solution to remove carbonate material. The residue was then cleaned in nanopure water for 30 min in an ultrasonic bath and dried in air overnight. Each piece was examined for signs of alteration under a binocular microscope, and fresh, clean material was handpicked for analysis. Mg# represents 100 · [Mg/(Mg + Fe^{2+})], where Fe^{3+}/Fe^{2+} is assumed to be 0.2. Mg# was not calculated for the sample with SiO_2 > 65%. LOI = loss on ignition.

Table 12. Comparison between the average of the two samples from Site 837, and similarly evolved rocks from the region.

	Site 837 (av.)	CLSC 10-1-1	CLSC RNDB 15-29-6	Lau Ridge NT165	Valu Fa D1-5
Major elements (wt%):					
SiO_2	55.73	52.21	55.37	55.32	56.04
TiO_2	1.36	2.61	1.48	0.77	1.37
Al_2O_3	14.86	12.04	15.49	18.32	14.39
$*Fe_2O_3$	12.79	18.16	12.25	8.67	12.63
MnO	0.21	0.30	0.21	0.21	0.22
MgO	3.44	3.23	3.65	3.41	3.69
CaO	8.08	7.59	8.24	8.52	7.66
Na_2O	2.65	3.23	2.70	3.08	3.33
K_2O	0.70	0.22	0.43	1.19	0.51
P_2O_5	0.17	0.41	0.18	0.53	0.16
Trace elements (ppm):					
Cr	BDL	10		8	
V	321	301		178	
Ni	3	16		7	
Rb	10	4.7		24	8.62
Sr	161	88		621	169
Y	36	109		31	
Zr	76	282		93	
Nb	2.5	6		4	
Ba	86	32.2			102

Notes: Sample 10-1-1 is from the Central Lau Spreading Center (CLSC; Ernewein et al., in press); RNDB-15-29-6 is at the south end of the CLSC propagating tip (Hawkins, 1989); NT165 is an arc rock from the Lau Island of Naitauba (Cole et al., 1985); and D1-5 is a sample from the Valu Fa Ridge (Jenner et al., 1987). Major element oxides are renormalized to 100% anhydrous. BDL = below detection level.

found in the sediments of the upper 10 mbsf, at about 20–25 mbsf, and between 57 and 60 mbsf, and correlate with regions of high clay content, as defined on the basis of smear slides (see "Lithostratigraphy" section, this chapter). The low values of water content, porosity, and void ratio at 18–19, 32–35, 62, and between 73 and 75 mbsf correlate with high sand content. The sediments in the region between 32 and 52 mbsf have a high silt content with relatively stable water contents, porosities, and void ratios.

The GRAPE bulk density values have been processed by initially averaging at 5–cm intervals to remove spurious data points caused by core-section ends and void spaces within the core (Fig. 32A), and then by applying a 15-point running average (Fig. 32B). The processed GRAPE bulk density data correlates well with sediment type and grain size at this site. The interval between the sediment/water interface and 27 mbsf is essentially a nannofossil ooze with an average bulk density of about 1.49 g/cm^3. Variations within this interval are caused by vitric volcanic sandy silt with a higher density than the nannofossil ooze. A downward-coarsening sequence of volcanic silt and sand between 27 and 35 mbsf is responsible for the increasing density from 1.49 to 1.6 g/cm^3 within this interval. A uniform density (1.49 g/cm^3) corresponds to a sequence of clay and silt with fine vitric ash between 35 and 55 mbsf. The anomalously low density at 50 mbsf is caused by incompletely filled core liners. In the lowest part of the sequence, the interbedding of nannofossil ooze and vitric sandy silts between 55 and 70 mbsf is reflected in the variability of measured density, and the increasing density (1.52 to 1.63 g/cm^3) is caused by increasing consolidation of the sediment.

Hole 837B

Two basalt samples were recovered from Hole 837B. Data are presented in Table 14. The bulk densities are 2.49 and 2.64 g/cm^3; the grain densities are 2.76 and 3.2 g/cm^3, respectively. These values are similar to those measured for basalts recovered at Sites 834–836.

Compressional Wave Velocity

Compressional velocity data measured with a Hamilton Frame device and the *P*-wave logger are shown in Figures 33 and 34 and listed in Tables 13 and 14. Compressional wave velocity values determed on discrete samples show little variability or gradient downhole. The average sediment velocity is 1504 m/s and ranges between 1461 and 1598 m/s. Discrete velocity measurements were made on representative samples (e.g., matrix material). Although an attempt was made to sample every lithology, clasts and inclusions were generally not measured, and velocity differences were small. Displaying the *P*-wave logger velocity on an expanded scale after applying a 15-point running average shows significant variability in the compressional wave velocity. The trends are similar to those found in the GRAPE-measured density. The nannofossil ooze within the upper 30 mbsf has average velocities just under 1500 m/s. Between 30 and 37 mbsf, the increasing velocity from 1500 to 1585 m/s reflects the increase in

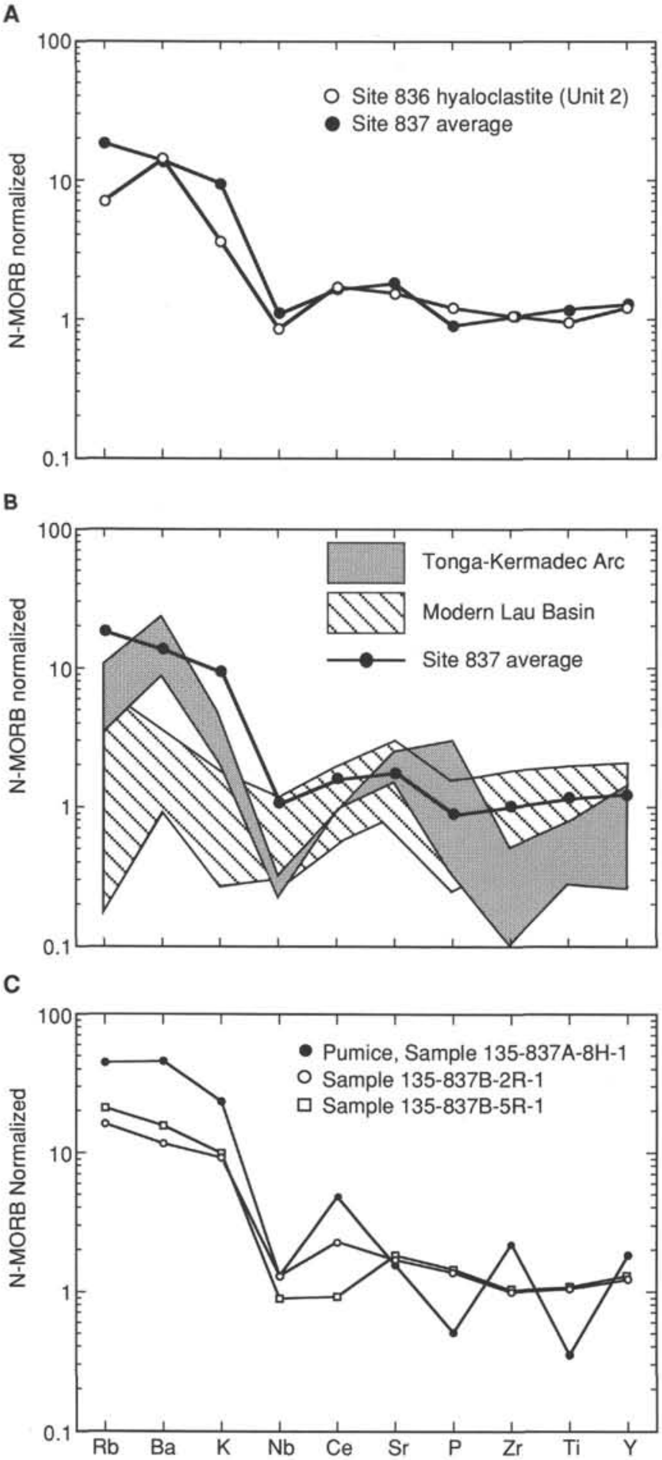

Figure 29. Representative analyses of Site 837 basaltic andesites normalized to values for N-MORB (Sun and McDonough, 1989). **A.** Average of basaltic andesites from Site 837 compared with analyses for andesitic hyaloclastites from Site 836, Unit 2. **B.** Site 837 basaltic andesites compared with representative analyses for modern volcanics from the Central and Eastern Lau spreading centers and Tonga and Kermadec arcs (data from Ernewein et al., in press; Hawkins and Melchior [1985] and Hawkins [1989] for Lau spreading centers; and Ewart and Hawkesworth [1987] for arc analyses). **C.** Two basaltic andesites from Site 837 compared with trace element signature of pumice sample recovered from Hole 837A.

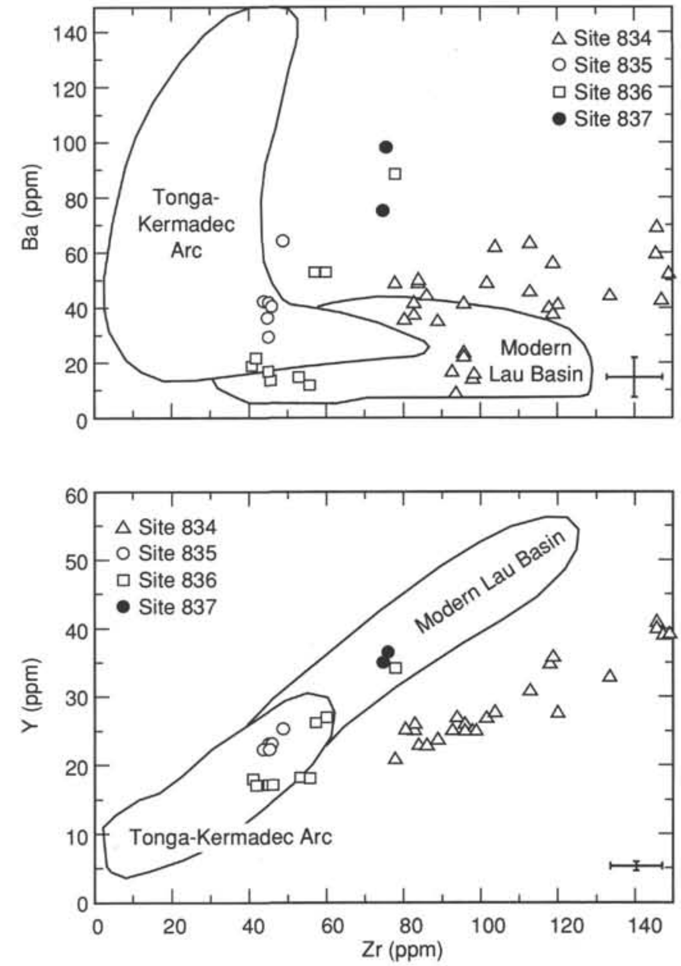

Figure 30. Analyses of Site 837 basaltic andesites compared with Site 834, 835, and 836 lavas, and volcanic rocks from the Tonga and Kermadec arcs and the active Central and Eastern Lau spreading centers (CLSC and ELSC, respectively). The highest Zr sample from Site 836 is from the andesitic hyaloclastite (Unit 2); note the similarity to the Site 837 basaltic andesites. Sources of data for the arc fields include Ewart and Bryan (1972), Ewart et al. (1973, 1977), Cunningham and Anscombe (1985), Hawkins and Falvey (1985), and Vallier et al. (1985). The fields for the modern Lau Basin are based on selected CLSC and ELSC data from Hawkins and Melchior (1985), Hawkins (1989), Ernewein et al. (in press), and Pearce (unpubl. data, 1991). Error bars are shown for ±1 standard deviation.

volcanic silt and sand. Between 37 and 53 mbsf, the velocity gradually increases from 1535 to 1585 m/s; this reflects the increase in grain size (from clay to silt and fine vitric ash), and thus bulk modulus, without a corresponding increase in bulk density (Fig. 32). The lowest interval between 53 and 80 mbsf is highly variable, reflecting the interbedding of nannofossil ooze and vitric sandy silts.

Undrained Vane Shear Strength

Values of undrained shear strength were obtained using the standard onboard miniature vane shear apparatus on unconsolidated sediments in Hole 837A; the results are plotted in Figure 35 and reported in Table 13.

In general, measurements are made on representative sections of core, which means that the matrix material, generally the finer

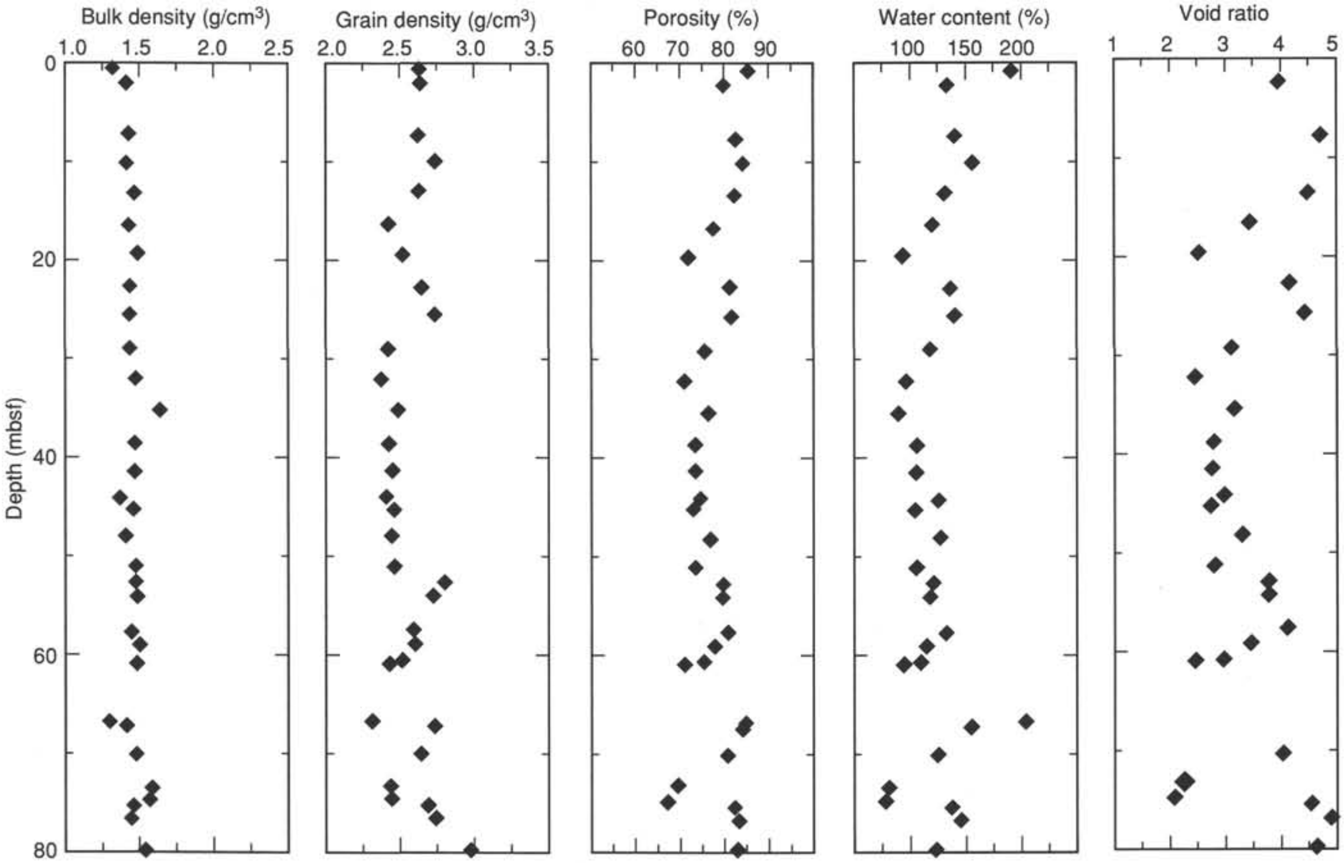

Figure 31. Index property data (grain density, bulk density, water content, porosity, and void ratio) vs. depth, Hole 837A.

grained sediment, is sampled preferentially. Initial shear strengths are low (about 5 kPa) and generally increase downhole to a high of 113 kPa at 79.8 mbsf. The upper 50 mbsf have low shear strength, averaging <20 kPa. Between 30 and 50 mbsf, however, shear strengths are unexpectedly low and do not show the intermediate values expected based on consolidation theory. This sequence has a high silt and sand content with a low clay content (see "Lithostratigraphy" section, this chapter). The consequent poor binding of the sediment reduces the shear strength of the material. Below 50 mbsf, significantly higher shear strengths were measured that increase steadily downhole.

Thermal Conductivity and Temperature Measurements

All thermal conductivity values in soft sediment cores were obtained using needle probes inserted through core liners into full core sections. For lithified sedimentary rocks and basalts, the thermal conductivity was measured on the split core face. The thermal conductivity results for both full and split cores from Holes 834A and 837B are shown in Figure 36 and listed in Tables 13 and 14. The thermal conductivity averages about 0.88 W/(m · °K) and shows no significant gradient with increasing depth.

The water sampler temperature probe (WSTP) was used to make temperature measurements at three points in Hole 837A. The results are shown in Figure 37. The temperature history in the sedimentary section should be such that after 5 min in the sediment, the decay curve is approximated by

$$T_{(}t) = \mathrm{A}/t + T_{eq},$$

where A is a constant determined experimentally, t is time, and T_{eq} is the equilibrium formation temperature (Hyndman et al., 1987). The temperature gradient defined by these measurements is about 2.11°C/100 m (Fig. 38) compared to 1.53°C/100 m at Site 835 and 5°C/100 m at Site 834. Thermal conductivity measurements (Fig. 36) were used to calculate thermal resistivity and integrated over depth. When the resulting thermal resistance is plotted with the temperature measurements from the WSTP temperature probe (Fig. 39), the slope of the regression line indicates that the heat flow in the region is 24.4 mW/m^2. For comparison, heat flow was 50 mW/m^2 at Site 834 and 14.5 mW/m^2 at Site 835; heat flow predicted by theoretical heat-flow curves approaches 200 mW/m^2 for young crust (Anderson et al., 1977).

Discussion

The physical properties data, particularly the GRAPE densities and *P*-wave logger compressional wave velocities, correlate well with the lithologic units identified within Site 837. For example, the density of the nannofossil ooze is relatively constant around 1.49 g/cm^3. An increase in volcanic sands and silts (30–35 mbsf) and an increase in consolidation state (70–80 mbsf) are reflected in increased density values. Compressional wave velocity particularly reflects the changes in grain size downhole. The velocity of the nannofossil ooze is about 1490 m/s and values higher than this reflect increases in grain size as in the 30–37 mbsf interval. In the interval between 37 and 53 mbsf, the grain size of the sediments increases from clay to silt with fine vitric ash. Because the density remains constant throughout this interval, the increased velocity is related to the increase in grain size. Interbedded nannofossil ooze and sandy silts results in variable density and velocity values.

The heat flow measured at Site 837 is 24.4 mW/m^2, low when compared with the theoretical heat-flow values of 175 to 200 mW/m^2 predicted for young crust (Anderson et al., 1977). Sites 834 and 835, more than 120 nmi to the northwest of Site 837, also

Table 13. Physical properties data, Hole 837A.

Core, section, interval (cm)	Depth (mbsf)	Su (kPa)	TC (W/[m · °K])	Bulk density (g/cm^3)	Grain density (g/cm^3)	Water content (%)	Porosity (%)	Void ratio	V_p (m/s)	V_p dir.
135-837A-										
1H-1, 77–78	0.77			1.33	2.63	191	85	5.8		
1H-2, 60	2.10		0.776081							
1H-2, 77–78	2.27	2.0		1.42	2.66	135	80	4.0		
1H-2, 84–86	2.34								1480	C
1H-3, 60	3.60		0.919121							
1H-4, 60	5.10		0.878276							
1H-4, 70–71	5.20	5.7								
1H-4, 77–79	5.27								1518	A
1H-5, 60	6.60		0.877766							
1H-5, 110–111	7.10	5.3								
1H-6, 2–4	7.52			1.44	2.63	141	83	4.7		
1H-6, 4–6	7.54								1516	A
1H-6, 15–16	7.65	5.9								
2H-2, 60	10.10		0.845228							
2H-2, 70–71	10.20			1.41	2.75	158	84	5.3	1492	A
2H-2, 75–76	10.25	12.2								
2H-3, 60	11.60		0.930631							
2H-4, 60	13.10		0.903959							
2H-4, 75–77	13.25	28.4		1.46	2.64	134	82	4.5		
2H-4, 77–79	13.27								1524	C
2H-6, 60	16.10		0.836762							
2H-6, 75–76	16.25	2.4								
2H-6, 97–99	16.47			1.44	2.42	123	77	3.4		
2H-6, 97–99	16.47								1478	C
3H-2, 57–60	19.57			1.5	2.52	96	72	2.5	1520	C
3H-2, 60	19.60		0.845414							
3H-2, 75–76	19.75	6.9								
3H-2, 103–106	20.03								1504	C
3H-3, 60	21.10		0.926806							
3H-4, 60	22.60		0.896256							
3H-4, 70–73	22.70			1.43	2.65	138	81	4.2	1473	C
3H-4, 75–76	22.75	21.5								
3H-6, 60	25.60		0.919118							
3H-6, 70–73	25.70			1.43	2.74	141	82	4.4		
3H-6, 75–76	25.75	26.6								
4H-2, 60	29.10		0.782129							
4H-2, 67–70	29.17			1.43	2.43	119	76	3.1	1530	C
4H-2, 75–76	29.25	11.8								
4H-2, 100–100	29.50		0.865636							
4H-4, 67–70	32.17			1.47	2.38	97	71	2.4		
4H-4, 75–76	32.25	4.8								
4H-4, 100–100	32.50		0.866117							
4H-4, 102–106	32.52	5.7								
4H-6, 85–86	35.35	15.3								
4H-6, 87–90	35.37			1.64	2.49	90	76	3.1	1521	C
4H-6, 100–100	35.50		0.833399							
5H-2, 60	38.60		0.764547							
5H-2, 67–70	38.67			1.46	2.43	106	73	2.8		
5H-2, 75–76	38.75	14.4								
5H-3, 60	40.10		0.883653							
5H-4, 40–43	41.40			1.46	2.44	106	73	2.8	1537	C
5H-4, 45–46	41.45	7.4								
5H-4, 60	41.60		0.839954							
5H-6, 20–23	44.20			1.36	2.41	127	75	2.9	1528	C
5H-6, 60	44.60		0.782726							
5H-6, 125–127	45.25			1.45	2.45	107	73	2.7		
5H-6, 125–126	45.25	8.7								
5H-6, 125–128	45.25								1518	C
6H-2, 70–73	48.20			1.4	2.44	129	77	3.3	1534	C
6H-2, 75–76	48.25	1.3								
6H-4, 70–73	51.20			1.46	2.45	107	73	2.8	1573	C
6H-4, 75–76	51.25	4.4								
6H-5, 50–50	52.50		0.892894							
6H-5, 69–71	52.69			1.47	2.8	122	79	3.8	1529	C
6H-5, 75–76	52.75	59.3								
6H-5, 100–100	53.00		0.975528							
6H-6, 50–50	54.00		0.945632							
6H-6, 70–73	54.20			1.48	2.71	120	79	3.8	1487	C
6H-6, 75–76	54.25	24.7								
6H-7, 30–30	55.30		0.957471							
7H-2, 60	57.60		0.890862							
7H-2, 70–73	57.70			1.44	2.58	134	80	4.1	1488	C
7H-2, 75–76	57.75	47.3								
7H-3, 60	59.10		0.930601							

Table 13 (continued).

Core, section, interval (cm)	Depth (mbsf)	Su (kPa)	TC (W/[m · °K])	Bulk density (g/cm^3)	Grain density (g/cm^3)	Water content (%)	Porosity (%)	Void ratio	V_p (m/s)	V_p dir.
135-837A- (cont.)										
7H-3, 65–68	59.15			1.49	2.58	114	77	3.4	1484	C
7H-3, 70–71	59.20	34.6								
7H-4, 60	60.60		0.778304							
7H-4, 70–73	60.70			1.46	2.5	110	75	3.0	1481	C
7H-4, 100–103	61.00			1.48	2.42	96	71	2.4		
7H-6, 60	63.60		0.83085							
7H-6, 100–103	64.00								1512	C
7H-6, 105–106	64.05	6.4								
8H-2, 25–26	66.75			1.29	2.3	203	85	5.5		
8H-2, 27–29	66.77								1598	C
8H-2, 50–52	67.00								1472	C
8H-2, 60	67.10		0.832764							
8H-2, 85–86	67.35	49.5		1.4	2.74	156	83	5.0		
8H-2, 87–89	67.37								1454	C
8H-3, 60	68.60		0.953695							
8H-4, 60	70.10		0.933935							
8H-4, 65–66	70.15	14.1								
8H-4, 66–68	70.16								1453	C
8H-4, 68–69	70.18			1.47	2.64	126	80	4.0		
8H-4, 123–125	70.73								1473	C
8H-4, 125–126	70.75	71.4								
8H-6, 60	73.10		0.869259							
8H-6, 80–81	73.30	25.4		1.57	2.43	82	69	2.2		
8H-6, 82–84	73.32								1530	C
9H-1, 25–26	74.75	21.0		1.56	2.44	79	67	2.0		
9H-1, 27–29	74.77								1523	C
9H-1, 74–75	75.24	44.1		1.45	2.69	139	82	4.5		
9H-1, 104–106	75.54								1473	C
9H-2, 60	76.60		0.866869							
9H-2, 75–76	76.75	38.6		1.44	2.74	144	83	4.9		
9H-3, 60	78.10		0.906934							
9H-4, 60	79.60		0.889605							
9H-4, 74–76	79.74	113.7		1.52	2.97	124	82	4.6		
9H-4, 77–79	79.77								1465	C
9H-5, 60	81.10		0.753739							

Notes: Su = undrained vane shear strength, TC = thermal conductivity, Vp = compressional (P-wave) velocity, Vp dir. = velocity direction, where A is the vertical velocity along the core, B is the horizontal velocity parallel to the cut core face, and C is the horizontal velocity perpendicular to the core face.

Table 14. Physical properties data, Site 837B.

Core, section, interval (cm)	Depth (mbsf)	TC (W/[m · °K])	Bulk density (g/cm^3)	Grain density (g/cm^3)	V_p (m/s)	V_p dir.
135-837B-						
1R-2, 60	2.10	0.754655				
1R-3, 60	3.60	0.968965				
1R-4, 30	5.10	0.849047				
3R-1, 87–95	81.05	1.445583				
3R-1, 88–90	81.08		2.49	2.76	3753	A
3R-1, 88–90	81.08				3585	B
3R-1, 88–90	81.08				3748	C
5R-1, 14–28	90.04	1.248074				
5R-1, 19–21	90.09		2.64	3.20	4116	A
5R-1, 19–21	90.09				4121	B
5R-1, 19–21	90.09				4042	C

Notes: TC = thermal conductivity, Vp = compressional (P-wave) velocity, Vp dir. = velocity direction, where A is the vertical velocity along the core, B is the horizontal velocity parallel to the cut core face, and C is the horizontal velocity perpendicular to the core face.

have low heat-flow values (50 and 14.5 mW/m^2, respectively). Although Site 837 is undoubtedly not located within the same heat and fluid circulation cell, similar conclusions to those from Sites 834 and 835 can be drawn: (1) that the sediments are not thick or diagenetically altered enough to function as an impermeable cap impeding fluid exchange between the sediments and seawater, and (2) that fluid circulation is sufficient to dissipate large amounts of heat.

DISCUSSION

The principal objectives for Site 837 were similar to those for Site 836. At Site 837, we were again unable to core a thick (>200 m) basement section. We were successful, however, in dating the basement by the microfossil assemblage of the overlying sediment, which provided information crucial for understanding the timing of backarc-spreading models. The integration of these data with those from Sites 836, 838, and 839 provides a closely spaced data set with which to test models for ridge jumps, ridge migration, and the initiation of the ELSC.

Deep penetration into basement was not possible at Site 837 because of unstable hole conditions. The basement rock cored consisted of basaltic andesites, approximately straddling the compositional fields for N-MORB and analyses of Tonga-Kermadec Arc volcanics. The upper sedimentary unit of nannofossil oozes overlies a sequence of thick, locally derived vitric turbidites. Rhyodacitic shards from an unknown source are abundant in the sediments. The age of the lowermost sediments is upper Pliocene, and these immediately overlie the basaltic andesite. The combination of paleomagnetic data and biostratigraphy provides an age estimate between 2 and 1.8 Ma for the basement. Sites 836 and 837 are separated across strike by a distance of about 20–25 km

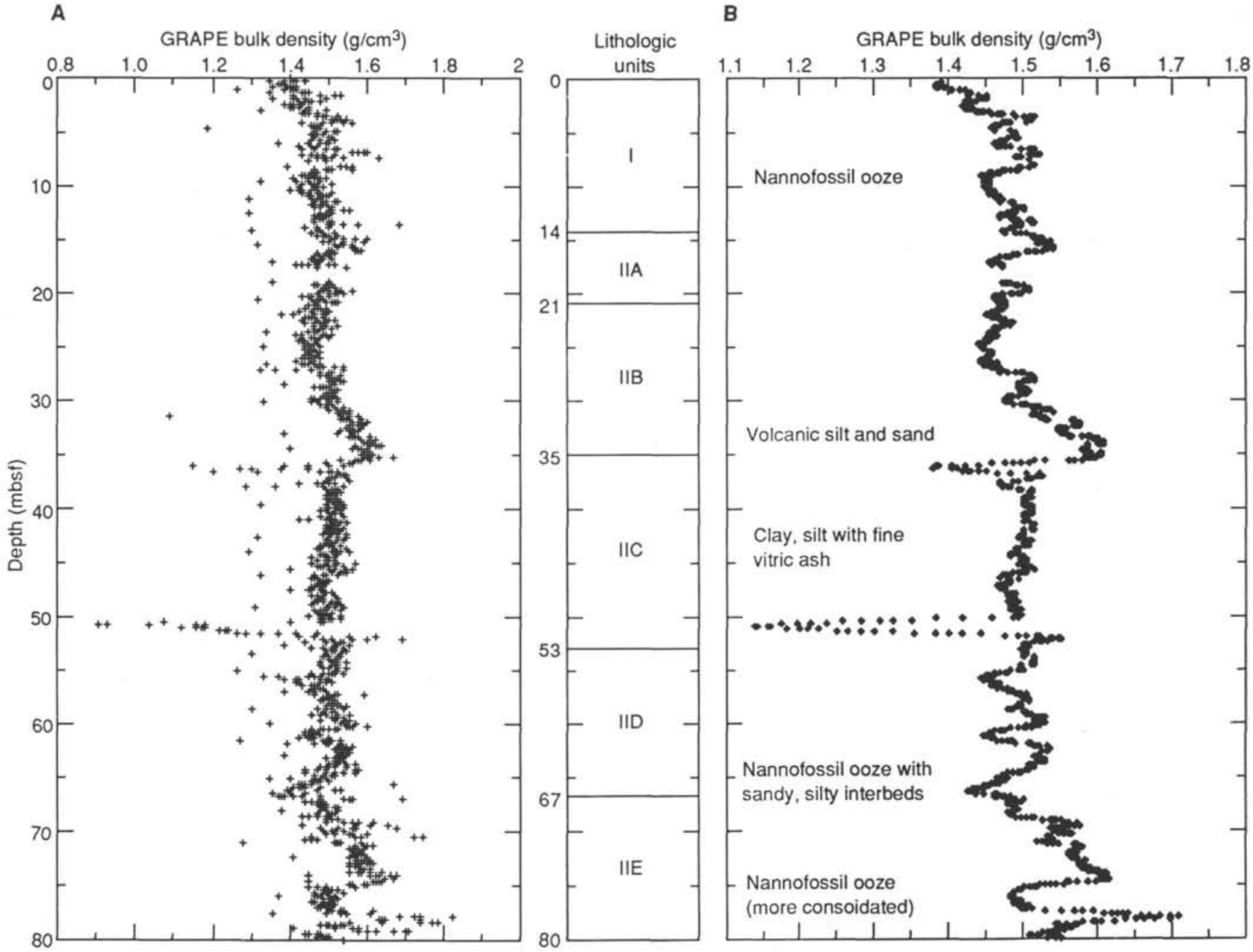

Figure 32. GRAPE bulk density vs. depth for Holes 837A. **A.** GRAPE bulk density at 5-cm intervals. **B.** GRAPE data after 15-point running average has been applied; the figure also identifies sediments that correlate with GRAPE density.

and have the youngest basement ages (0.7 and 2.1 Ma, respectively). If the basin floor formed by "normal" seafloor crustal accretion from the ELSC, an average half spreading rate of 14 mm/yr has prevailed. This is similar to the rate recognized at the ELSC. We lack data to prove that the crust at this site is genetically related to the ELSC and it may have formed by a mechanism different from seafloor spreading.

REFERENCES

Anderson, R. N., Langseth, M. G., and Sclater, J. G., 1977. The mechanisms of heat transfer through the floor of the Indian Ocean. *J. Geophys. Res.*, 82:3391–3409.

Bagnold, R. A., 1956. The flow of cohesionless grains in fluids. *Philos. Trans. R. Soc. London A*, 249:235–297.

Berger, A. L., 1978. Long-term variations of caloric solar insolation resulting from earth's orbital variations. *Quat. Res.*, 9:139–167.

Berggren, W. A., Kent, D. V., Flynn, J. J., and Van Couvering, J. A., 1985a. Cenozoic geochronology. *Geol. Soc. Am. Bull.*, 96:1407–1418.

Berggren, W. A., Kent, D. V., and Van Couvering, J. A., 1985b. The Neogene: Part 2. Neogene geochronology and chronostratigraphy. *In* Snelling, N. J. (Ed.), *The Chronology of the Geological Record.* Geol. Soc. London Mem., 10:211–260.

Chaproniere, G.C.H., in press. Pleistocene to Holocene planktic foraminiferal biostratigraphy of the Coral Sea, offshore Queensland, Australia. *BMR J. Aust. Geol. Geophys.*

Church, B. N., and Johnson, W. M., 1980. Calculation of the refractive index of silicate glasses from chemical composition. *Geol. Soc. Am. Bull.*, 91:619–625.

Clement, B. M., and Robinson, F., 1987. The magnetostratigraphy of Leg 94 sediments. *In* Ruddiman, W. F., Kidd, R. B., Thomas, E., et al., *Init Repts. DSDP*, 94 (Pt 2): Washington (U.S. Govt. Printing Office), 635–650.

Cole, J. W., Gill, J. B., and Woodhall, D., 1985. Petrologic history of the Lau Ridge, Fiji. *In* Scholl, D., and Vallier, T. (Eds.), *Geology and Offshore Resources of Pacific Island Arcs—Tonga Region.* Circum-Pac. Counc. Energy Miner. Resour., Earth Sci. Ser., 2:379–414.

Cronan, D. S., Hodkinson, R. A., Harkness, D. D., Moorby, S. A., and Glasby, G. P., 1986. Accumulation rates of hydrothermal metalliferous sediments in the Lau Basin, S.W. Pacific. *Geo.-Mar. Lett.*, 6:51–56.

Cunningham, J. K., and Anscombe, K. J., 1985. Geology of 'Eua and other islands, Kingdom of Tonga. *In* Scholl, D., and Vallier, T. (Eds.), *Geology and Offshore Resources of Pacific Island Arcs—Tonga Region.* Circum-Pac. Counc. Energy Miner. Resour., Earth Sci. Ser., 2:221–258.

Emeis, K.-C., and Kvenvolden, K. A., 1986. Shipboard organic geochemistry on *JOIDES Resolution. ODP Tech. Note*, No. 7.

Ernewein, M., Pearce, J. A., Bloomer, S. H., Parson, L. M., Murton, B. J., and Johnson, L. E., in press. Geochemistry of Lau Basin volcanic rocks: influence of ridge segmentation and arc proximity. *Contrib. Mineral. Petrol.*

Ewart, A., Brothers, R. N., and Mateen, A., 1977. An outline of the geology and geochemistry, and the possible petrogenetic evolution of the volcanic rocks of the Tonga-Kermadec-New Zealand island arc. *J. Volcanol. Geotherm. Res.*, 2:205–250.

Ewart, A., and Bryan, W., 1972. Petrography and geochemistry of the igneous rocks from 'Eua, Tonga Islands. *Geol. Soc. Am. Bull.*, 83:3281–3298.

Ewart, A., Bryan, W. B., and Gill, J., 1973. Mineralogy and geochemistry of the younger volcanic islands of Tonga, southwest Pacific. *J. Petrol.*, 14:429–465.

Ewart, A., and Hawkesworth, C. J., 1987. The Pleistocene-Recent Tonga-Kermadec arc lavas: interpretation of new isotope and rare earth data in terms of a depleted mantle source model. *J. Petrol.*, 28:495–530.

Fisher, R. V., and Schmincke, H.-U., 1984. *Pyroclastic Rocks:* New York (Springer-Verlag).

Harland, W. A., Cox, A. V., Llewellyn, P. G., Pickton, C.A.G., Smith, A. G., and Walters, R., 1982. *A Geologic Time Scale:* Cambridge (Cambridge Univ. Press).

Hawkins, J. W., 1976. Petrology and geochemistry of basaltic rocks of the Lau Basin. *Earth Planet. Sci. Lett.*, 28:283–298.

———, 1989. Cruise Report—ROUNDABOUT Expedition, Legs 14, 15, R/V *Thomas Washington.* SIO Ref. Ser., No. 89-13.

Hawkins, J. W., and Falvey, D. A., 1985. Petrology of andesitic dikes and flows from 'Eua, Tonga. *In* Scholl, D., and Vallier, T. (Eds.), *Geology and Offshore Resources of Pacific Island Arcs—Tonga Region.* Circum-Pac. Counc. Energy Miner. Resour., 2:269–280.

Hawkins, J. W., and Melchior, J. T., 1985. Petrology of Mariana Trough and Lau Basin basalts. *J. Geophys. Res.*, 90:11,431–11,468.

Hiscott, R. N., and Middleton, G. V., 1979. Depositional mechanics of thick-bedded sandstones at the base of a submarine slope, Tourelle Formation (Lower Ordovician), Quebec, Canada. *In* Doyle, L. J., and Pilkey, O. H. (Eds.), *Geology of Continental Slopes:* Soc. Econ. Paleontol. Mineral. Spec. Publ., 27:307–326.

Hodkinson, R. A., Cronan, D. S., Glasby, G. P., and Moorby, S. A., 1986. Geochemistry of marine sediments from the Lau Basin, Havre Trough and Tonga-Kermadec Ridge. *N. Z. J. Geol. Geophys.*, 29:335–344.

Hyndman, R. D., Langseth, M. G., and Von Herzen, R. P., 1987. Deep Sea Drilling Project geothermal measurements: a review. *Rev. Geophys.*, 25:1563–1582.

Jenner, G. A., Cawood, P. A., Rautenschlein, M., and White, W. M., 1987. Composition of back-arc basin volcanics, Valu Fa Ridge, Lau Basin: evidence for a slab-derived component in their mantle source. *J. Volcanol. Geotherm. Res.*, 32:209–222.

Lowe, D. R., 1982. Sediment gravity flows: II. Depositional models with special reference to the deposits of high-density turbidity currents. *J. Sediment. Petrol.*, 52:279–297.

Mankinen, E. A., Donnelly, J. M., and Grommé, C. S., 1978. Geomagnetic polarity event recorded at 1.1. m.y.r. B.P. on Cobb mountain, Clear Lake volcanic field, California. *Geology*, 6:653–656.

Nilsson, K., Florendo, F. F., and Hawkins, J. W., et al., 1989. Petrology of a nascent triple junction, northeastern Lau Basin. *Eos*, 70:1389.

Parson, L. M., et al., 1989. RRS *Charles Darwin* Cruise 33/88, 5 May–1 June 1988. Geophysical and geological investigations of the Lau back-arc basin, SW Pacific. *Inst. Oceanogr. Sci. Deacon Lab. Cruise Report*, No. 206.

Parson, L. M., Pearce, J. A., Murton, B. J., and RRS *Charles Darwin* Scientific Party, 1990. Role of ridge jumps and ridge propagation in the tectonic evolution of the Lau back-arc basin, southwest Pacific. *Geology*, 18:470–473.

Pickering, K. T., Hiscott, R. N., and Hein, F. J., 1989. *Deep Marine Environments: Clastic Sedimentation and Tectonics:* London (Unwin Hyman).

Reich, V., Marchig, V., Sunkel, G., and Weiss, W., 1990. Hydrothermal and volcanic input in sediments of the Lau Back-Arc Basin, S.W. Pacific. *Mar. Mining*, 9:183–203.

Ruddiman, W. F., and McIntyre, A., 1981. Oceanic mechanisms for amplification of the 23,000-year ice volume cycle. *Science*, 212:617–627.

Schmincke, H.-U., 1981. Ash from vitric muds in deep sea cores from the Mariana Trough and fore-arc regions (south Philippine Sea) (Sites 453, 454, 455, 458, 459). *In* Hussong, D. M., Uyeda, S., et al., *Init. Repts. DSDP*, 60: Washington (U.S. Govt. Printing Office), 473–481.

Sun, S.-S., and McDonough, W. F., 1989. Chemical and isotopic systematics of oceanic basalts: implications for mantle composition and processes. *In* Saunders, A. D., and Norry, M. J. (Eds.), *Magmatism in the Ocean Basins.* Geol. Soc. Spec. Publ. London, 42:313–345.

Taylor, S. R., Arculus, R. J., Perfit, M. R., and Johnson, R. W., 1981. Island arc basalts. *Basaltic Volcanism on the Terrestrial Planets* (Basaltic Volcanism Study Project): New York (Pergamon Press), 193–213.

Vallier, T. L., Stevenson, A. J., and Scholl, D. W., 1985. Petrology of igneous rocks from Ata Island, Kingdom of Tonga. *In* Scholl, D., and Vallier, T. (Eds.), *Geology and Offshore Resources of Pacific Island Arcs—Tonga Region.* Circum.-Pac. Counc. Energy Miner. Resour., Earth Sci. Ser., 2:301–316.

von Stackelberg, U., 1990. R.V. *Sonne* Cruise SO 48: summary of results testing a model of mineralisation. *Mar. Mining*, 9:135–144.

Walker, R. G., 1975. Generalized facies models for resedimented conglomerates of turbidite association. *Bull. Geol. Soc. Am.*, 86:737–748.

Ms 135A-107

NOTE: All core description forms ("barrel sheets") and core photographs have been printed on coated paper and bound separately as Part 2 of this volume, beginning on page 681.

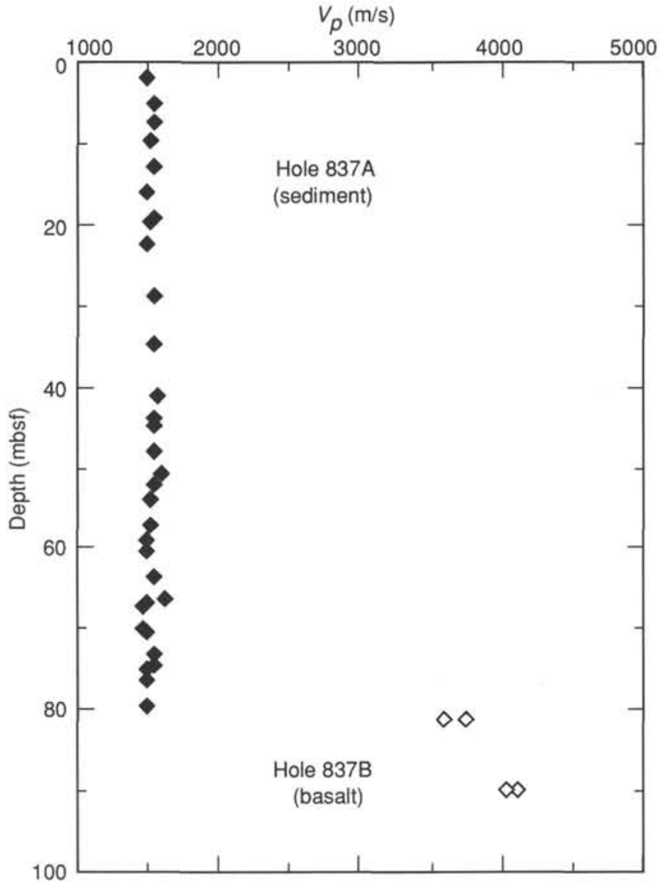

Figure 33. Compressional wave velocity vs. depth, Holes 837A and 837B.

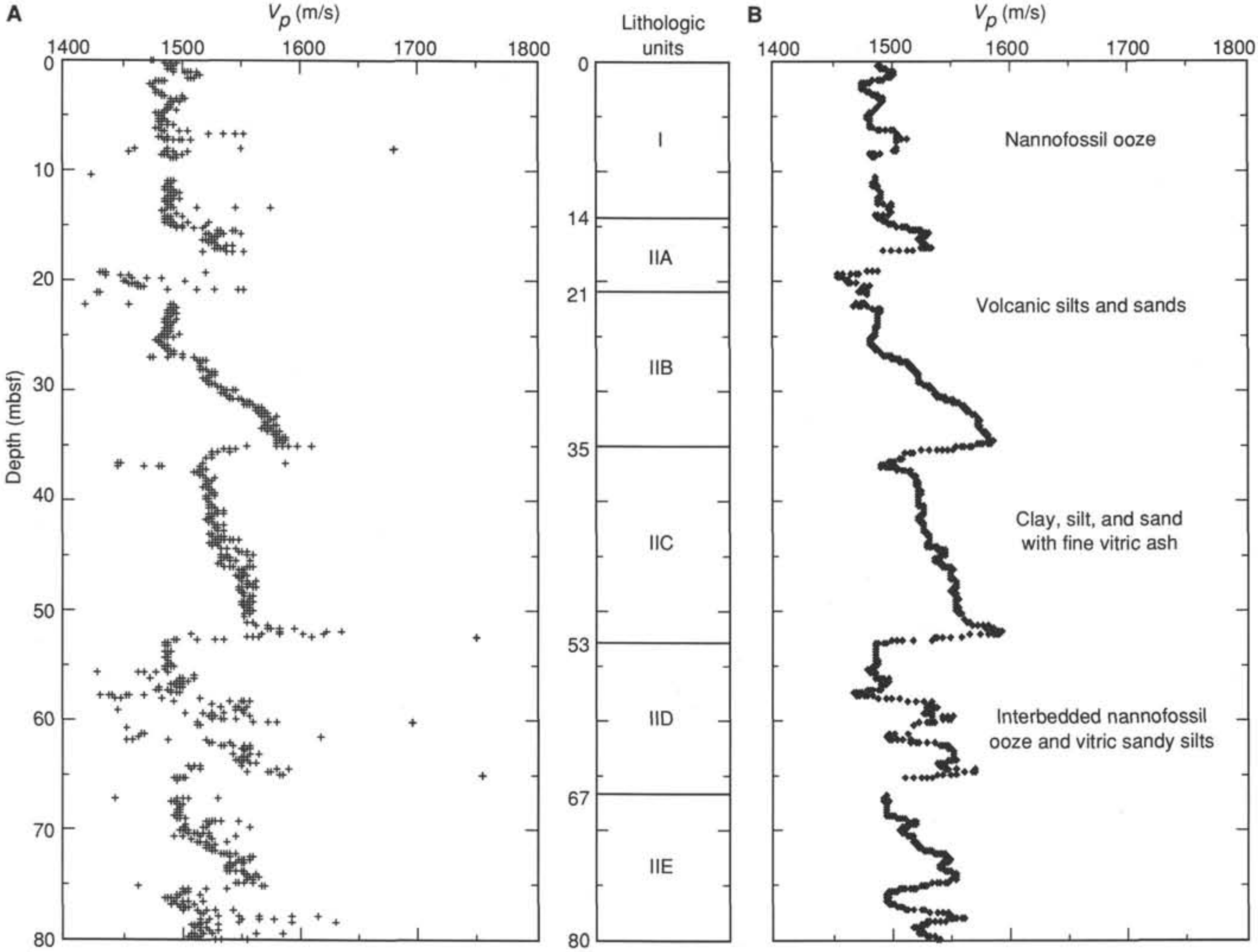

Figure 34. *P*-wave logger data vs. depth, Hole 837A. **A.** After initial 5-cm averaging. **B.** After application of 15-point running average. The figure also identifies sediments that correlate with *P*-wave logger velocity.

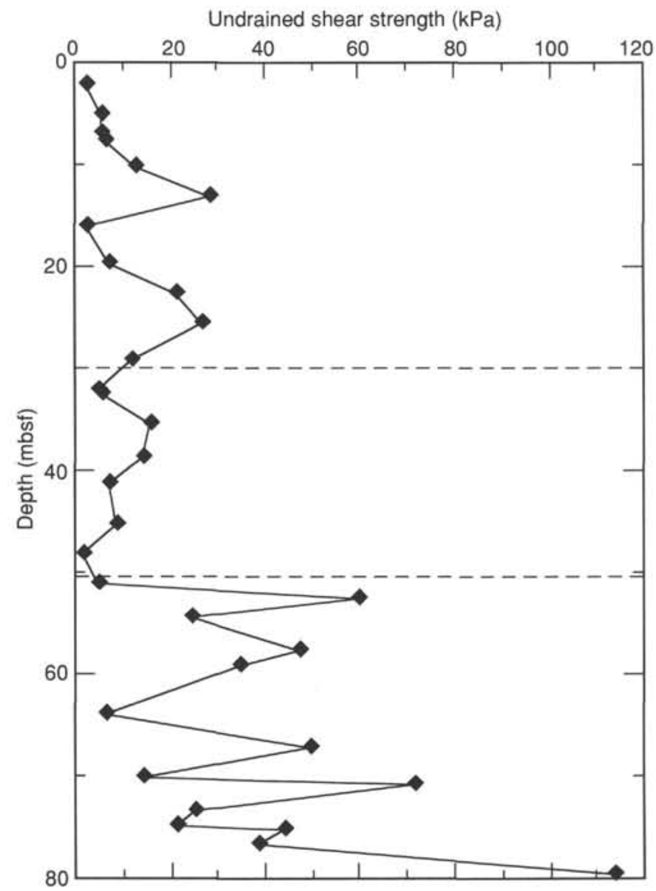

Figure 35. Undrained vane shear strength vs. depth, Hole 837A. Dashed lines separate the upper, middle, and lower intervals of shear strength discussed in the text.

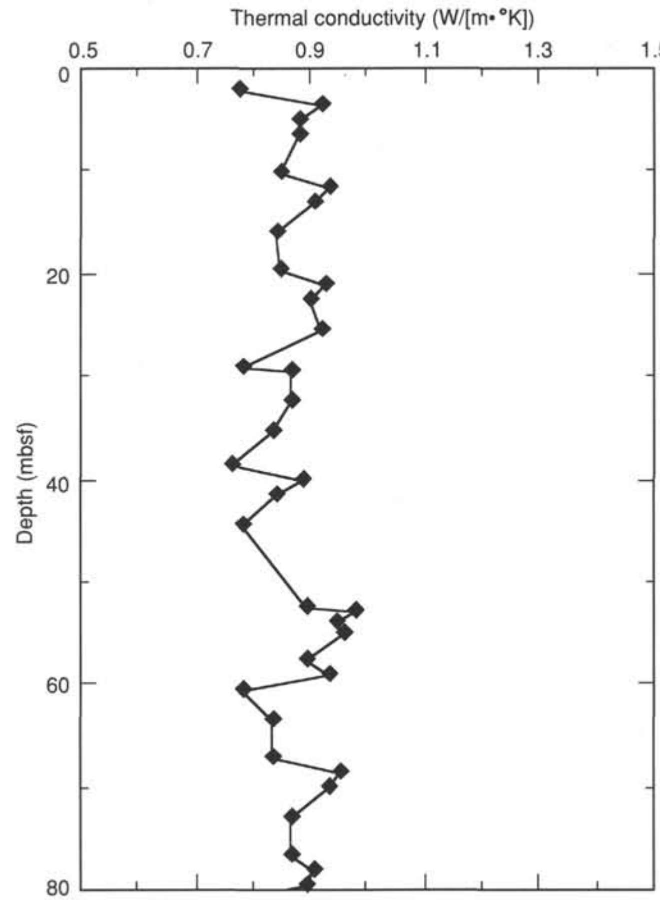

Figure 36. Thermal conductivity vs. depth, Hole 837A.

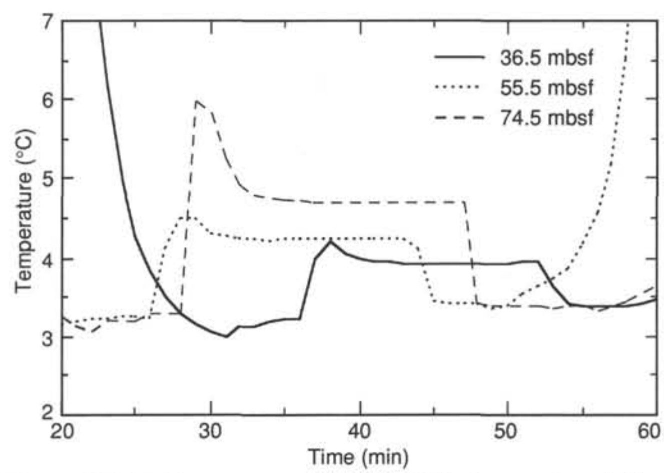

Figure 37. Heat flow measurements, Hole 837A, from various depths, based on WSTP probe temperature runs.

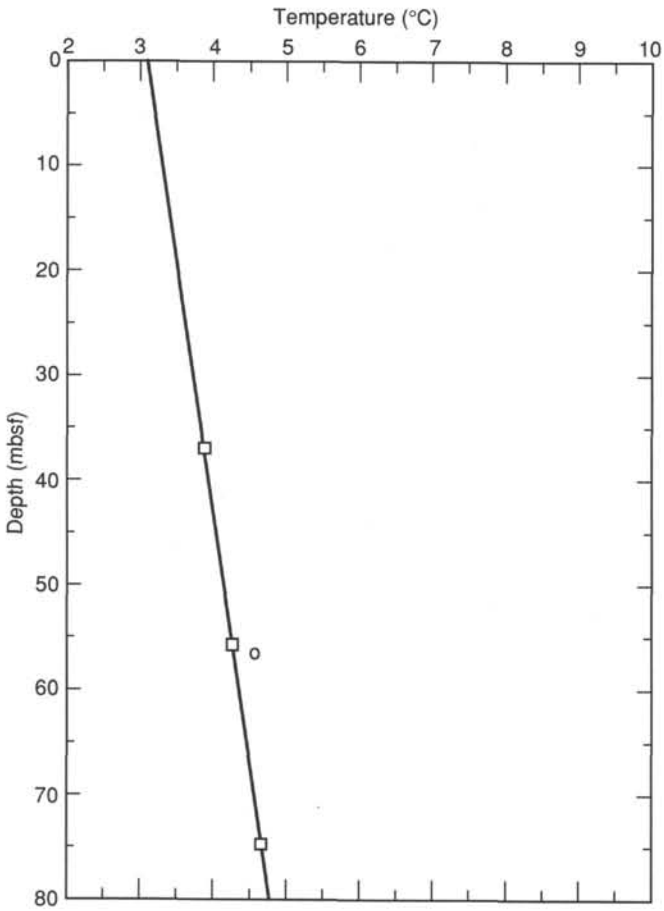

Figure 38. Temperature gradients vs. depth, Hole 837A. The line through the values indicates a geothermal gradient of 2.11°C/100 m.

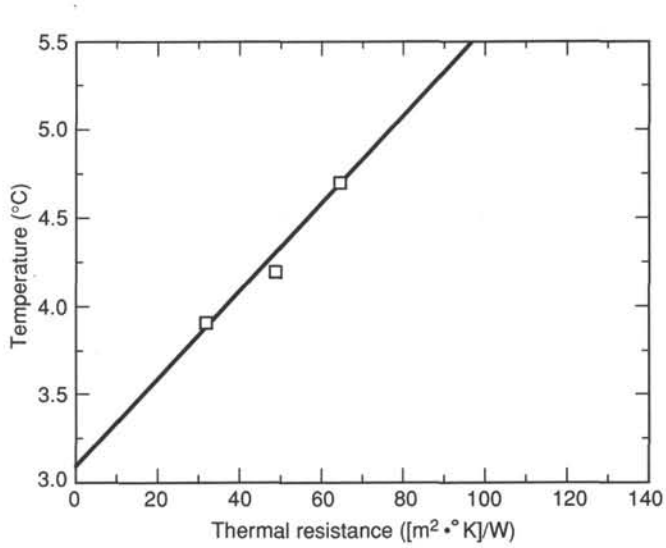

Figure 39. Thermal resistance vs. temperature, Site 837. The slope of the line indicates the magnitude of the heat flow for this site, which is 2.44 mW/m^2.